

**Doctoral thesis**

**Numerical simulation of evaporation behavior  
and solute deposit of a sessile droplet on  
substrates**

**1138008 Li Rongjuan**

**Advisor Dr. Yoshio Morozumi**

**Course of Engineering**

**Graduate School of Engineering, Kochi University of Technology**

**August 2012**



## **Abstract**

Thin film or particle layer is formed after evaporation or drying of droplets with solid particles or solute on substrates, which is frequently observed in nature and in industrial processes. The difference in the shape of thin film or particle layer is affected by the evaporation behavior such as contact line motion, internal fluid flows and thin film formation after drying a sessile droplet on substrates. The objective of this study is to investigate the contact line motion, internal fluid flows and solid particles transport during drying a sessile droplet on homogeneous or patterned substrates by using numerical simulation based a two-phase lattice Boltzmann model.

In this study, a mathematical model is developed which is composed of a two-phase lattice Boltzmann method incorporating with an evaporating model, a wetting model and a solid particles transport model. The present evaporation model and wetting model are tested by comparing with theoretical or experiment results. The results of the evaporation model agree well with a theoretical law of the square of the droplet radius with time. The wetting model can give the correct contact angle of droplet on substrates at steady states. In addition, the solid particle transport model is proposed, based on a Newton equation of each solid particle motion during droplet evaporation on substrates.

In two-phase lattice Boltzmann simulation, spurious velocities appeared in

the interface region between liquid and vapor phase. Therefore, the effect of computational parameters on the reduction of spurious velocities is investigated. The dimensionless surface tension can significantly reduce the spurious velocities with preserving the real properties of surface tension by adjusting scale parameters. The spurious velocities slightly decrease as the density ratio of the liquid and vapor phase decreases. In addition, the effect of the order parameter on the spurious velocities and the time steps needed to reach steady state are examined.

Evaporation behavior of a droplet on a homogenous substrate is numerically investigated. The calculation results of droplet evaporation on hydrophilic substrates shows the transition from pinning to de-pinning of the contact line motion, while those on the hydrophobic substrate shows only de-pinning of the contact line throughout the evaporation. In addition, internal fluid flows towards the contact line of the droplet in the pinning stage of the evaporation are discussed.

The contact line motion of an evaporating droplet on a patterned substrate with line-shaped hydrophilic region is numerically investigated. The effects of the width of hydrophilic region and the evaporation rate on the contact line motion are discussed. The calculated result shows the transition of the contact line motion from de-pinning to pinning when the contact line reaches to the edge of the hydrophilic region of patterned substrates. In addition, the difference in the pinning time and the evaporation termination time is obtained

for variation of hydrophilic region on patterned substrates.

Finally, solid particles transport and deposit after droplet evaporation on homogenous substrate are numerically investigated. In present simulation, the solid particles toward to downward and centre of the evaporating droplet on hydrophilic substrate. And the shape of solid particles deposit shows thick in the center and thin in edge of the deposit.

**Key words:** Lattice Boltzmann Model, Evaporation Model, Wetting Model, Solid Particles Transport Model, Contact Line Motion, Internal Fluid Flows, Solid Particles Deposit.



# Contents

## CHAPTER 1 INTRODUCTION .....1

1.1	Background.....	1
1.2	Outline .....	3
1.3	Literature review .....	5

## CHAPTER 2 NUMERICAL SIMULATION MODEL .....17

2.1	Introduction .....	17
2.2	Two-phase lattice Boltzmann model.....	17
2.3	Boundary conditions.....	24
2.4	Wetting model.....	27
2.5	Evaporation Model.....	33
2.6	Solid particles transport model.....	37
2.7	Conclusions .....	39

## CHAPTER 3 THE EFFECT OF THE COMPUTATIONAL PARAMETERS ON THE REDUCTION OF SPURIOUS VELOCITIES IN LB SIMULATION OF TWO-PHASE FLOWS .....41

3.1	Introduction .....	41
3.2	Numerical simulation.....	42
3.3	Results and discussion .....	43
3.3	Conclusions .....	51

## **CHAPTER 4 A LATTICE BOLTZMANN SIMULATION OF CONTACT LINE MOTION AND INTERNAL FLUID FLOWS IN AN EVAPORATING DROPLET ON HOMOGENOUS SUBSTRATES.....53**

4.1	<i>Introduction</i> .....	53
4.2	<i>Numerical Simulation</i> .....	53
4.3	<i>Results and Discussion</i> .....	55
4.4	<i>Conclusions</i> .....	67

## **CHAPTER 5 A LATTICE BOLTZMANN SIMULATION FOR CONTACT LINE MOTION OF EVAPORATING DROPLET ON PATTERNED SUBSTRATES.....69**

5.1	<i>Introduction</i> .....	69
5.2	<i>Numerical simulation</i> .....	69
5.3	<i>Results and Discussion</i> .....	71
5.4	<i>Conclusions</i> .....	78

## **CHAPTER 6 A LATTICE BOLTZMANN SIMULATION FOR SOLID PARTICLE TRANSPORT AFTER A DROPLET EVAPORATION ON HOMOGENOUS SUBSTRATE.....80**

6.1	<i>Introduction</i> .....	80
6.2	<i>Numerical simulation</i> .....	80
6.3	<i>Results and Discussion</i> .....	83
6.4	<i>Conclusions</i> .....	85



<b>CHAPTER 7 CONCLUSIONS.....</b>	<b>87</b>
<b>REFERENCES .....</b>	<b>90</b>
<b>PUBLICATIONS.....</b>	<b>99</b>
<b>ACKNOWLEDGMENTS</b>	



# Chapter 1 Introduction

## 1.1 Background

Inkjet printing technology can produce monodisperse microdroplets of a few microns to millimeter in diameter and deposit on specific regions of substrates. This technology has been developed and implemented in droplet-on-demand devices based on piezoelectric or thermal ink-jet technology. Fig. 1-1 shows a piezoelectrically driven droplet-on demand device. Two designs producing the fluid ejection and retraction pressure pulse by piezoelectric are the most common printing applications. A tubular design is easier to fabricate by hand, however, it is inferior to a flat plate design in the ability to be used as elements in miniaturized packed arrays.

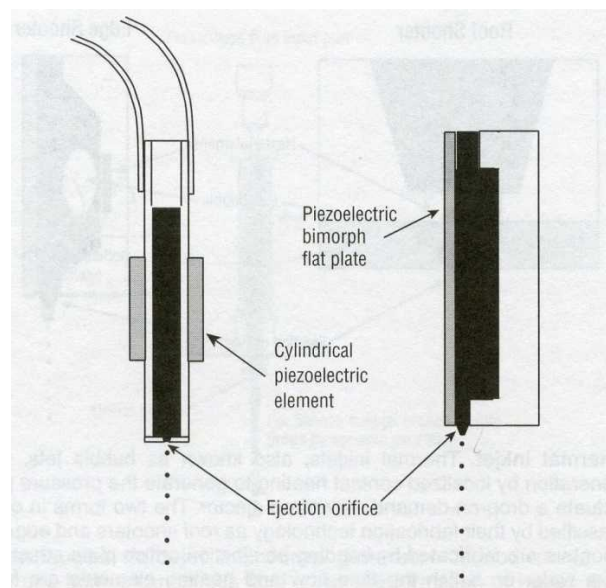


Fig. 1-1 Piezoelectrically driven droplet-on-demand microdroplet ejectors [1].

Recently, inkjet printing has become an attractive technology in the application to manufacturing and engineering such as the electrical, optical, and biotechnology industries [2-4]. In these industrial processes, thin films or particle layers are formed by evaporation and drying of droplets with solid constituents or solutes. The shape of the thin films or particle

layers is affected by fluid properties of droplets or wettability of substrates. For example, dot-like deposit is formed on hydrophobic substrates due to the de-pinning of the contact line of the droplets throughout the evaporation process. In contrast, ring-like deposit is formed on hydrophilic substrates due to the pinning of the contact line. When the contact line is pinned during evaporation process, internal fluid flows inside the droplet will occur to supply the mass loss around the contact line caused by evaporation, and then the solute or particles are transported toward the contact line, leading to the ring-like deposit [5]. The difference in the deposit shape is mainly caused by the internal fluid flows of evaporating droplet. Therefore, it is of great practical interest to investigate the evaporation behavior as well as internal fluid flows and thin film formation after drying of a sessile droplet on substrates. In addition, thin film formation will be applied to the production of organic thin film transistors by the deposit of inkjet droplets on patterned substrates with different wettability, forming thin film of line-shape or dot-shape patterns on hydrophilic region of the substrates [6-8]. However, contact line motion and internal fluid flows during the evaporation of a droplet affects greatly on solute deposit or the shape of the thin film, which have not been understood clearly.

The objective of this study is to investigate the contact line motion, internal fluid flows and thin film formation after drying a sessile droplet on homogeneous or patterned heterogeneous substrates. To this end, first, a mathematical model for simulating the evaporation of a droplet on substrates is presented. The validity of the mathematical model is confirmed by comparing with theoretical or experimental results. Second, a lattice Boltzmann (LB) simulation is performed to investigate the evaporation behavior and internal fluid flows of a single droplet on substrates with homogeneous wettability. The effect of evaporation rate and the wettability of substrates on the contact line motion and internal flows are discussed. Third, a two-phase LB simulation is performed to investigate the evaporation of an evaporating droplet on patterned substrates with heterogeneous wettability. The contact line motion is discussed for various patterned substrates with different width of hydrophilic regions. Finally, solid particles transport and deposit after drying a droplet on hydrophilic substrates is numerically studied by incorporating a solid particles transport model into the two-phase lattice Boltzmann model.

## 1.2 Outline

The outline of the present dissertation is introduced as follows.

In Chapter 1, background and objectives of this study are presented. Then literature review on the inkjet film formation, evaporation behavior of a single droplet on substrates and numerical studies of two-phase flows are summarized in order to clarify the significance of this study.

In Chapter 2, a mathematical model for the simulation of an evaporating droplet on substrates is introduced. The mathematical model is composed of a two-phase lattice Boltzmann model, wetting model and evaporation model. A lattice Boltzmann model is a class of computational fluid dynamics methods and is based on microscopic and mesoscopic kinetic equation by considering the behavior of a collection of fluid particles as a unit. A wetting model is used to describe the wettability of substrates, which is applicable to the present lattice Boltzmann model. In the present study, two kinds of wetting models are utilized; an adhesive force wetting model and a partial wetting boundary condition model. An evaporation model is proposed to describe evaporation of liquid phase on the droplet surface by adding an evaporation term into the particle distribution function for the order parameter. The evaporation term indicates the rate of mass loss in the interface region between the liquid and vapor phases. The evaporation of a droplet in ambient vapor is calculated to examine the validity of the present evaporation model. In addition, a solid particle transport model is proposed, which is capable to describe colloid particles motion in a droplet and deposit onto substrates.

In Chapter 3, a two-phase lattice Boltzmann simulation is performed to investigate the effect of simulation parameters such as dimensionless surface tension, density ratio and order parameter on the spurious velocities that appear in a droplet in ambient vapor. A dimensionless surface tension parameter is given with preserving actual values of the physical properties of surface tension by adjusting the scale parameter. The dimensionless surface tension can significantly reduce the spurious velocities. The magnitude of the spurious velocities is sufficiently small to neglect the internal fluid flow caused by the spurious velocities in an evaporating droplet. Nevertheless, the decrease in the order

parameter does not affect the reduction of spurious velocities, the smaller the order parameter is the shorter the time to reach steady state becomes. The spurious velocities slightly decrease as the density ratio of the liquid and vapor phase decreases.

In Chapter 4, a two-phase lattice Boltzmann simulation is performed to investigate the evaporation behavior of a single droplet on substrates with homogeneous wettability. An evaporation model is used in the simulation to describe the mass loss from the surface of the evaporating droplet. In addition, a partial wetting boundary condition is imposed on the lattice sites on the substrate surface to determine the wettability of the substrate. During the evaporation of a droplet on a hydrophobic substrate, the wetting diameter decreases while the contact angle remains almost constant. The evaporation termination time increases when the evaporation rate coefficient decreases. In order to take into account the dynamical changes in the contact angle in the pinning stage of evaporation, the partial wetting boundary condition is modified by using the relationship between the change in the droplet volume and the contact angle when the contact line is pinned. In addition, internal fluid flows towards the contact line of the droplet in the pinning stage of the evaporation are discussed.

In Chapter 5, a two-phase lattice Boltzmann simulation is performed to investigate the evaporation behavior of a droplet on the patterned substrate with different wettability. The patterned substrates have hydrophilic region with the width of  $L_{\text{phi}}$  in the middle of hydrophobic region. The wettability of substrate is evaluated by the adhesive force between liquid and wall to give static contact angles of liquid film on the substrate. In addition, the difference in the pinning time and the evaporation termination time is obtained for different width of hydrophilic region on patterned substrates.

In Chapter 6, deposit of solid particles after drying droplet on substrates is numerically investigated. A solid particles transport model is proposed which is capable to incorporate into the two-phase lattice Boltzmann model for simulating the solute deposit of an evaporating droplet on substrates. Solid particles transport inside the droplet is evaluated by solving a Newton equation for each solid particle inside the droplet. This equation accounts for the particles transport due to the surrounding fluid flows, the force of the capillary interaction between the particle and the liquid-vapor interface, gravity, buoyancy force and the force due to the potential energy of the interaction of each solid particle with any other

solid particle. The solid particles transport inside droplet and the shape of solid particle deposit after droplet evaporation are investigated.

In Chapter 7, conclusions of this study and future works are presented.

## **1.3 Literature review**

Literature review on the inkjet film formation, evaporation behavior of a single droplet on substrates and numerical simulations of two-phase lattice Boltzmann model are summarized.

### **1.3.1 Application of Inkjet printing to film formation**

Inkjet printing can form monodispersed droplets in picoliter size, which is widely used in the field of printers in office and household. Recently, inkjet printing is a key technology for producing micro-droplets on specific region of substrates used in various industrial manufacturing. For example, the inkjet technology has been applied to electrical [3, 9-11], optical [12] and biotechnology industries [13]. Fig. 1-2 shows a schematic diagram of high-resolution inkjet printing onto a pre-patterned substrate to form organic thin-film transistor (TFT) [3].

Inkjet technology can be used to ‘write’ refractive microlenses for optical interconnects. Fig. 1-3 illustrates an assembled smart-pixel switch containing a lens array printed using the inkjet technology [14, 15].

Inkjet droplets deposition of active elements such as DNA has been interested because bioactive fluids are usually not suitable for use in photolithographic or other subtractive processes. Fig. 1-4 shows the result of hybridizing a wild type *M. tb.* target to an array of 100  $\mu\text{m}$  oligonucleotide probes spots printed on 200  $\mu\text{m}$  centers [15]. While a probe complementary to a drug resistant mutant strain was printed to form the letters ‘TB’, a probe complimentary to the wild type was printed around the letters to fill in the square array.

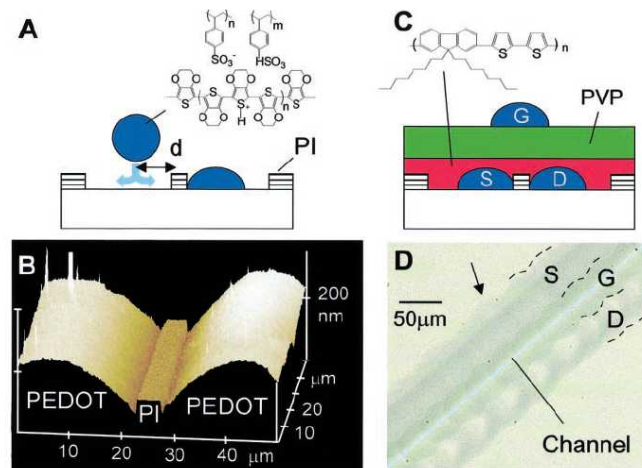


Fig. 1-2 (A) A schematic diagram of high-resolution inkjet printing onto a prepatterned substrate. (B) Atomic force microscopy (AFM) showing accurate alignment of inkjet-printed PEDOT/PSS source and drain electrodes separated by a repelling polyimide (pi) line with  $L = 5 \mu\text{m}$ . (C) Schematic diagram of the top-gate inkjet printing TFT configuration with an F8T2 semiconducting layer (S, source; D, drain; and G, gate). (D) Optical micrograph of an inkjet printing TFT ( $L = 5 \mu\text{m}$ ) [3].

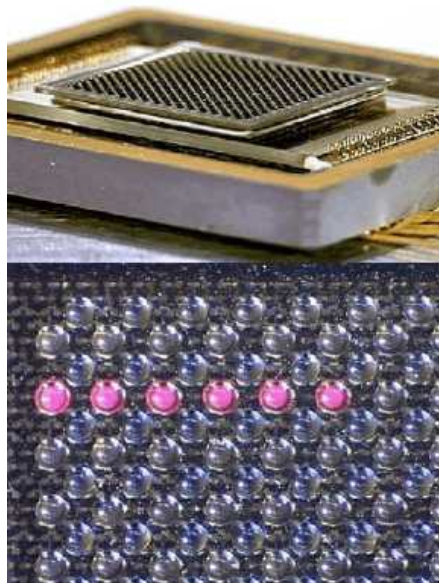


Fig. 1-3 Smart-pixel array module (top) and printed 250 μm diameter microlens array in module with VCSELs under 6 lenslets turned on (bottom) [14, 15].





Fig. 1-4 100  $\mu\text{m}$  spots of DNA on 200  $\mu\text{m}$  centers: wild type *M.tb.* probe hybridized with wild type target [15].

For above all, the inkjet printing method is main technologies applied to various industrial processes due to the simplicity, low cost, flexibility and maturity. In these processes, microdroplets with solid constituents or solutes deposit onto substrates to form thin films or particle layers after evaporation and drying of the droplets. The thickness profile or uniformity of the thin film is key factors for the industrial processes. Therefore, the evaporation or drying of droplet on substrates has been investigated experimentally, theoretically or numerically.

### 1.3.2 Evaporation or drying of droplet on substrates

The evaporation behavior of a sessile droplet on substrates has been investigated in a large number of experimental, theoretical or numerical studies.

Shanahan and Bourg s [16] measured the variation of the contact angle and wetting diameter of an evaporating droplet on polymer surfaces. They found three stages of evaporation behavior characterized by two types of contact line motion: the wetting diameter remains constant whereas the contact angle decreases (pinning), the wetting diameter decreases and the contact angle remains constant (de-pinning), and the wetting diameter decreases with decreasing contact angle (pinning and de-pinning mixture). The evolution of a sessile droplet on a polymer surface for three stages are shown in Fig. 1-5. Bourg s and

Shanahan [17] investigated the evaporation of sessile drops of water and *n*-decane on various substrates. In the results, two or three different stages appeared, depending on the surface roughness. Hu and Larson [18] performed a numerical analysis of the evaporation of a droplet with a pinned contact line and predicted the evaporation flux along the droplet surface. They analyzed the microfluid flow in an evaporating sessile droplet with pinned contact line using an analytical lubrication theory in numerical studies [19].

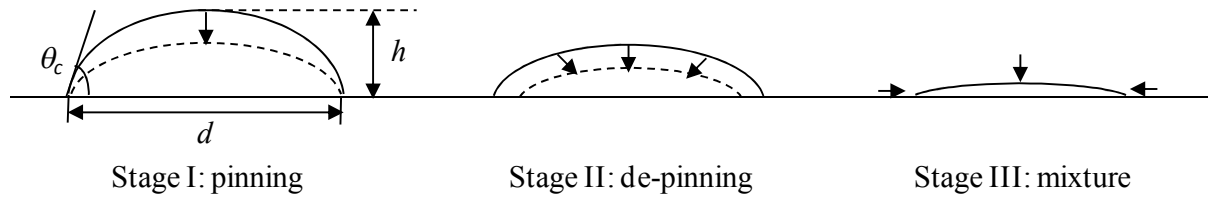


Fig. 1-5 Schematic representation of a sessile droplet during evaporation.

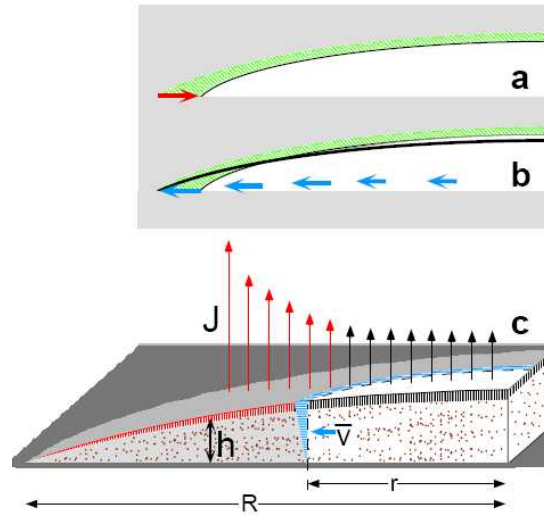


Fig. 1-6 Mechanism of outward flow during evaporation. **a** and **b** show an increment of evaporation viewed in cross-section [5]. In **a**, the result of evaporation without flow: the droplet shrinks. In **b**, the compensating flow needed to keep the contact line fixed. In **c**, the quantities responsible for flows leave at a rate per unit area  $J(r)$ . The removed liquid contracts the height  $h(r)$  vertically, vacating the vertically striped region in a short time  $\Delta t$ . Depth-averaged speed of fluid flows is  $\bar{v}(r)$ .

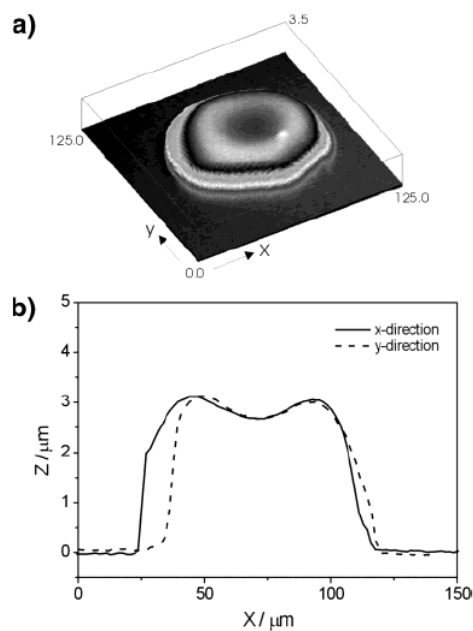


Fig. 1-7 (a) Volcano-shaped polymer dot, formed by an inkjet printed droplet of a 1 wt% solution of polystyrene in acetophenone on perfluorinated glass; (b) cross-sections in the  $x$ - and  $y$ -directions [21].

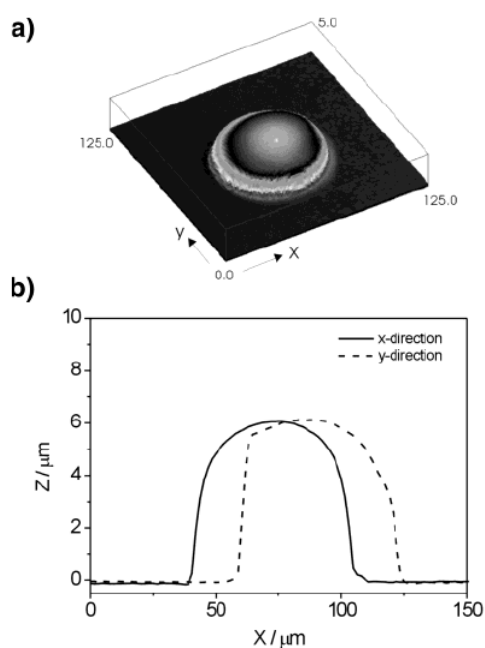


Fig. 1-8 (a) Polymer dot, fomed by a droplet of a 1 wt% solution of polystyrene in an 80/20 wt% ethyl acetate/acetophenon mixture on perfluorinated glass; (b) cross-sections in the  $x$ - and  $y$ -directions [21].

As for the formation of thin films or particle layers, Deegan *et al.* [5, 20] investigated the ring-like deposit of solutes formed after the drying of droplets and reported that the ring-like deposit is a result of outward flows towards the contact line when the contact line is pinned. Fig. 1-6 illustrates the factors leading to outward flow in a small, thin, dilute, circular droplet of fixed radius  $R$  slowly drying on a solid surface.

De Gans and Schubert [21] studied the film formation from a polymer solution droplet and the film shape after the drying of the droplet by changing the ratio of the mixture solvent. Fig. 1-7 and 1-8 shows a polymer dot shape after drying of polystyrene solution droplet for different ratio of the mixture solvent.

Morozumi *et al.* [22] investigated the effect of the substrate temperature on the shape of the ring-like deposit both experimentally and numerically. Park and Moon [23] investigated the particle deposit patterns by controlling the particle concentration of the colloidal ink. Fig. 1-9 shows the morphologies of  $\text{SiO}_2$  particle deposit produced from the single inkjet droplets by varying ink concentration from 0.5 to 4 vol% after drying on the hydrophilic Si substrate. In their results, they demonstrated the particle concentrations play a critical role for determining the morphologies of particle deposit from evaporating colloidal droplets.

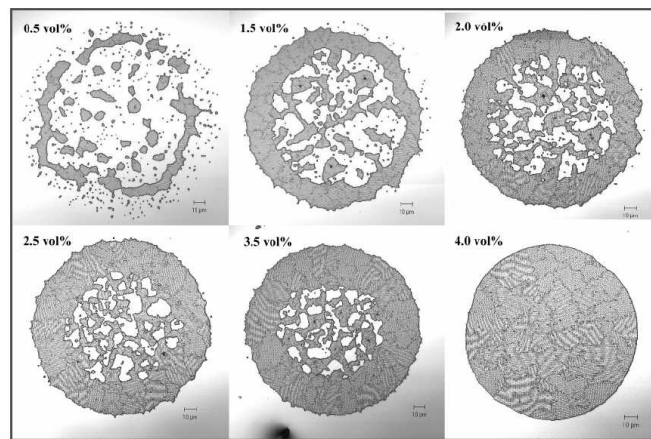


Fig. 1-9 Images of deposit patterns composed of the silica microspheres produced by inkjet printing of a single inkjet droplet of water/ formamide (FA)-based ink [23].

Fukai *et al.* [24] investigated the effects of the droplet size and initial solute concentration on the drying process and film shape of polymer solution droplets and the film

shape. Both pinning and de-pinning of the contact line were observed on hydrophilic substrates, whereas the pinning of the contact line was not observed on hydrophobic substrates. The shape of the film formed by the evaporation of a sessile droplet was affected not only by the contact line motion but also by internal flows during the evaporation. Kim *et al.* [25] performed an experimental study of the direction and the magnitudes of internal fluid flows inside an evaporating water droplet using a theoretical equation of the vertically averaged velocity. They explained the ring-like deposit in the final stage of evaporation from the observation of the vertically averaged internal velocities of an evaporating droplet. Soltman and Subramanian [26] reported that the enhancement or elimination of the coffee ring is achieved by adjusting temperature in their drying features. Kaneda *et al.* [27] investigated the effect of the initial solute concentration and the evaporation rate of a droplet on a hydrophobic substrate on the flow pattern, both experimentally and numerically. Yoshitake *et al.* [28] carried out a numerical simulation of internal flows induced by the Marangoni effect and discussed the effect of the contact angle on the solute transport. Yunker *et al.* [29] reported that the shape of the suspended particles is important factor and can be used to eliminate the ring-like deposit: ellipsoidal particles are deposited uniformly during evaporation.

Evaporating behavior and thin film formation on heterogeneous substrate have also been investigated. Wang *et al.* [30] proposed a method that was improvement of droplet positioning accuracy on substrates and controlled thin film patterning (Fig. 1-10). Jung *et al.* [31] studied the drying of a thin film of oligomeric polymer solution placed on a substrate enclosed by bank to avoid a ring-like deposit of polymer solute. Morita *et al.* [7] proposed sub-micrometer and micrometer scale site-selective coating of polymer solution on flat patterned substrates with different wettability, and obtained complete line-patterned polymer thin film with a line of hydrophilic region. The difference in wettability between the front and backsides of the film would be a key factor for the formation of patterned thin film. Fig. 1-11 shows the micrographs of polymer thin films coated by inkjet method.

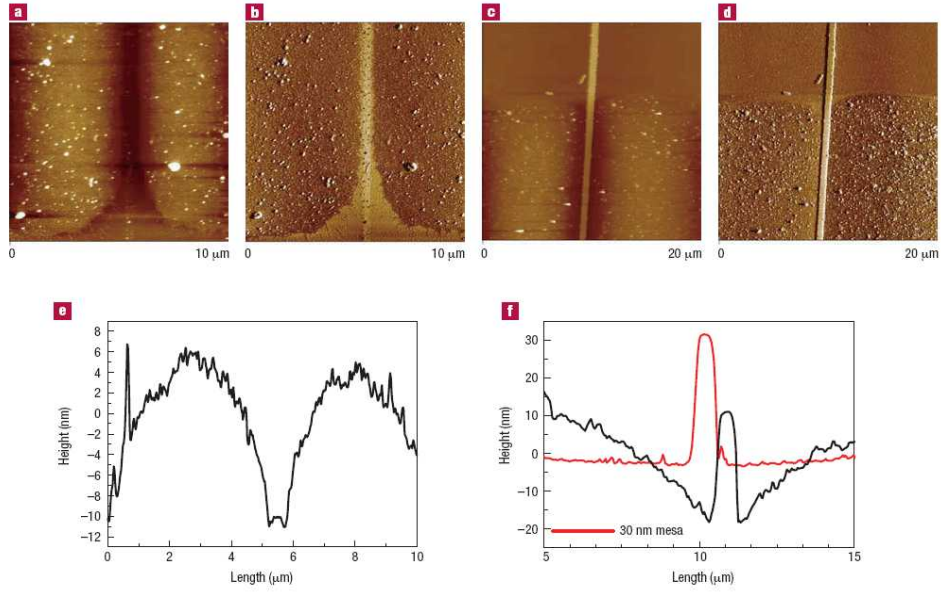


Fig. 1-10 AFM pictures of dewetted PEDOT/PSS (polymer poly/poly) [30]. a, b, e show AFM topography (a), phase (b) and cross-sectional image (e) of dewetted 1:3 PEDOT/PSS droplets split on top of a 250-nm FDTD SAM without mesa. C, d, f give the corresponding dewetting results of 1:1 PEDOT/PSS droplets on a 500-nm-wide FDTD SAM with 30-nm mesa.

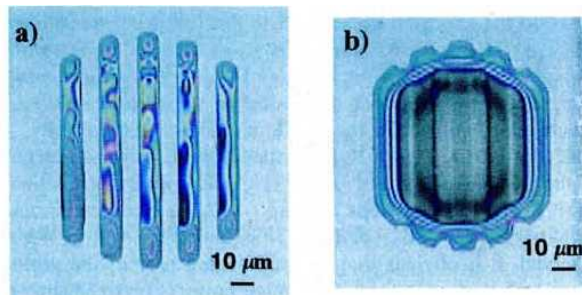


Fig. 1-11 Optical micrographs of polymer thin films coated by ink-jet method. PS/xylene solution was applied on (a)  $R_f$ /Si-OH and (b)  $R_h(C10)$ /Si-OH patterned surfaces with 10  $\mu$ m line width [7].

### 1.3.3 Two-phase lattice Boltzmann model

Lattice Boltzmann model (LB) model is a numerical model based on a microscopic and mesoscopic kinetic equation, which is derived from lattice gas automata (LGA) method [32, 33]. The LB model has been used to simulate multiphase flows [34-37]. Shan and Chen [38, 39] described the LB model in detail by incorporating an interparticle potential term in order

to model the phase segregation and surface tension of nonideal gases and liquid-gas phase. A LB model based on the free-energy approach was proposed by Swift *et al.* [40, 41] to simulate the hydrodynamics of phase separation and two-phase flows. In the model by Swift *et al.*, standard boundary conditions are provided in order to investigate the effect of wetting on the phase separation and the fluid flow in confined geometries.

#### **(a) Two-phase lattice Boltzmann model with large density ratio**

A larger number of researchers started to solve two-phase flows with large density ratio same as that of actual liquid and gas fluids. Lee and Lin [42], and Inamuro *et al.* [43] made it possible to track the interface movement of two-phase flows with a large density ratio up to 1000. Tanaka *et al.* [44] employed the two-phase lattice Boltzmann model proposed by Inamuro *et al.* [43] to simulate a droplet impinging on a solid surface. Yan and Zu [45] performed a numerical simulation of the droplet spreading on partial wetting substrates by using the two phase lattice Boltzmann model of Inamuro *et al.* [43] with the partial wetting boundary conditions of Briant *et al.* [46-48]. Zheng *et al.* [49] proposed a LB model without solving the Poisson equation and complex treatments for derivative terms. This method was further verified by applying to capillary wave and the bubble rising. Begum *et al.* [50] further demonstrated the validity of an incompressible LB method by using Casson's Rheology model [51] and Shan and Chen model [38] for different flows and phase transition process.

#### **(b) Spurious velocities**

To simulate the interfacial dynamics between gas and liquid phase, an intermolecular force term is required in the lattice Boltzmann equations. However, the intermolecular force term between gas and liquid phase will cause unphysical flows in order to satisfy the balance of interaction surface stresses in the interfacial region. The unphysical velocity is also called as spurious velocities or currents [52]. The reduction of spurious velocities is required in interfacial dynamics of multiphase flows. For example, in a drying droplet on substrates, internal fluid flows caused by droplet evaporation will transport solid constituents or solutes toward the contact line [20]. In this case, reducing or eliminating of spurious velocities are required for an accurate computation of solute deposit of a drying droplet [53]. Therefore, much attention has been paid to the reduction or elimination of the spurious velocities in past researches. He *et al.* [54] proposed a LB formulation derived by He and Luo [55]. In their

study, they suggested that an improved LB scheme could remove unphysical approximations. Further, He *et al.* [56] proposed a new LB scheme. In their LB scheme, a pressure distribution function was introduced to replace the single particle density distribution function. As a result, the numerical stability could be improved by reducing the effect of numerical errors in the calculation of molecular interactions. Wagner [57] reported that the origin of spurious velocities is caused by the different discretization of driving forces for order-parameter and momentum equations in LB model. To eliminate the spurious velocities, the pressure form of the driving force term was replaced by the potential form of the driving force term. However, artificial viscosity was used for stable computation. Lee and Fischer [58] pointed out the spurious velocities are caused by discretization errors in the computation of the intermolecular force. Thus, they proposed a mixture scheme of discretization for potential form of the intermolecular force. However, non-mass conservation exists in their model [59]. Lou *et al.* [60] proposed a necessary condition for linear combinations of the interaction force and fluid density in interface regions for vanishing spurious velocities. In addition, this necessary condition can not be fulfilled at a discrete level due to discretization errors. Pooley and Furtado [61] showed the magnitude of spurious velocities which can be significantly reduced with a careful choosing of equilibrium distribution functions with the stencils of numerical calculation derivatives in a free-energy lattice Boltzmann algorithm. In addition, they presented a second numerical scheme which moves the gradient terms of intermolecular force in the equilibrium distribution function into a body force term leading to a further reduction of spurious velocities while preserving momentum conservation.

Physical properties or equation of state of two-phase fluids have also a great influence on the reduction of spurious velocities. Leclaire [62] investigated the effect of surface tension coefficient on the spurious velocities. Yu and Fan [63] showed the spurious velocities decreases with increasing viscosity of the two-phase fluid. In lattice Boltzmann simulation, physical properties of density, viscosity and surface tension are non-dimensionalized by giving the characteristic scales of time, length and mass. However, these dimensionless physical properties cannot be given uniquely. This is because these dimensionless properties can recover the actual physical properties by appropriately adjusting the characteristic scales, even if the dimensionless physical properties are arbitrarily chosen. Equation of state is utilized



to describe the relationship between temperature, pressure and volume (or density) for a given fluid. In two-phase flows, thermodynamic pressure evaluated by equation of state is incorporated into the intermolecular force term in order to distinguish the two-phase of fluid. Order parameter or density is used to define the shape of equation of state. Yuan [64] investigate the maximum magnitude of spurious velocities can be greatly reduced by changing the equation of state.

### **(c) Wetting model**

To simulate a droplet or liquid-gas interface on solid substrates, a wetting model is incorporated into two-phase LB model to describe wettability of the solid substrate. Sukop and Or [65] introduced a force between fluid particles and solid surface [66] which was incorporated into LB model by Newton's law. Briant *et al.* [46] developed a wetting model by adding partial boundary condition into equilibrium distribution function at wall sites. It is possible to control the wetting angle at any flat substrate. Iwahara *et al.* [67] proposed a boundary condition between fluid-side and solid-side nodes. This boundary condition was incorporated into the two-dimensional two-phase LB method of Inamuro *et al.* [68, 69] and used to model smooth substrates of chemically heterogeneous surfaces. Davies *et al.* [70] proposed a dynamic wetting boundary condition for the 'finite-density' multiphase model to give wettability of substrates. In this model, a surface affinity  $a_s$  was defined at first. The wetting boundary condition of  $-1 \leq a_s \leq 1$  is corresponding to from a non-wetting boundary to perfectly wetting boundary.

### **(d) Contact line motion**

Due to boundary condition developed for giving the wetting of droplets, the hydrodynamics behaviour, such as the spread of droplet or contact line motion of droplet on a homogenous or heterogeneous substrate had been investigated. LB simulations of contact line behavior on solid surface have been reported [46-48]. Dupuis and Yeomans [71-74] presented a LB model to describe the spreading of droplets on topologically patterned substrates. The dynamics of liquid droplets on chemically patterned substrates was presented by Kusumaatmaja *et al.* [75] using a free energy LB model. Chang and Alexander [76] applied the nearest-neighbor molecular interaction force [66] to the adhesive force and investigated the spreading of a single droplet on striped surfaces of hydrophilic and

hydrophobic domain. Yeomans and Kusumaatmaja [77] modeled the droplet dynamics and captured the physics of droplets moving across patterned surfaces. Yan [78] focused on surface tension dominated behaviour of water droplets spreading on hydrophilic surface with hydrophobic strips of different sizes and contact angles under different physical and interfacial conditions. Kim *et al.* [79] provided a relationship between local roughness and contact angle to analyze different possible roughness distributions and to calculate the effect of the cross-sectional area of pillars by using a LB model of Inamuro *et al.* [43].

**(e) Evaporation or condensation**

Yamamoto and Suzuki [80] simulated evaporation phenomenon of metals by using a LB method. Zhang and Chen [81] presented a LB method to simulate liquid-vapor boiling process. Joshi and Sun [53, 82, 83] further developed the LB model which can simulate particle deposition on patterned substrates. Márkus and Házi [84] simulated evaporation through a plane interface by applying an extension of the Shan-Chen lattice Boltzmann method [38]. Kamali *et al.* [85] argued the evaporation and condensation at the nose and the tail of the moving bubble that facilitates the motion of the three-phase contact line in the Shan-Chen LB approach [38].

## Chapter 2 Numerical Simulation Model

### 2.1 Introduction

A lattice Boltzmann method (LBM) is a powerful tool to simulate phase segregation [86] or interfacial dynamics of multiphase fluid flows [37], e.g. multiphase or multicomponent flows [49, 87]. The key success of the LBM is based on microscopic and mesoscopic kinetic equations, and it is more efficient to simulate the interfacial dynamics of multiphase fluid flows compared with traditional computational fluid dynamics (CFD) methods based on Navier-Stokes equation. In particular, the model makes it possible to track the interface movement of two-phase flows with a large density ratio up to 1000 [42, 43]. In this chapter, two-phase LB models are introduced, incorporating a wetting model, an evaporation model and a solid particles transport model. In addition, boundary conditions are also discussed in this section.

### 2.2 Two-phase lattice Boltzmann model

#### 2.2.1 Lee and Lin model

Lattice Boltzmann models are based on microscopic and mesoscopic kinetic equations, and the behaviour of a collection of fluid particles is considered to recover the conservation law of continuum fluid dynamics. The property of a collection of fluid particles at a given node point is represented by a discrete-velocity distribution function of particle number density. The fluid particles are confined to the node of a regular lattice, and the movement of the fluid particles are restricted toward the neighboring nodes with discrete-velocities. Fig. 2-1 shows a two-dimensional nine velocity (D2Q9) model. In the D2Q9 model, identical particles velocities are given by

$$[e_0, e_1, e_2, e_3, e_4, e_5, e_6, e_7, e_8] = \begin{bmatrix} 0 & 1 & 0 & -1 & 0 & 1 & -1 & -1 & 1 \\ 0 & 0 & 1 & 0 & -1 & 1 & 1 & -1 & -1 \end{bmatrix} \quad (2-1)$$

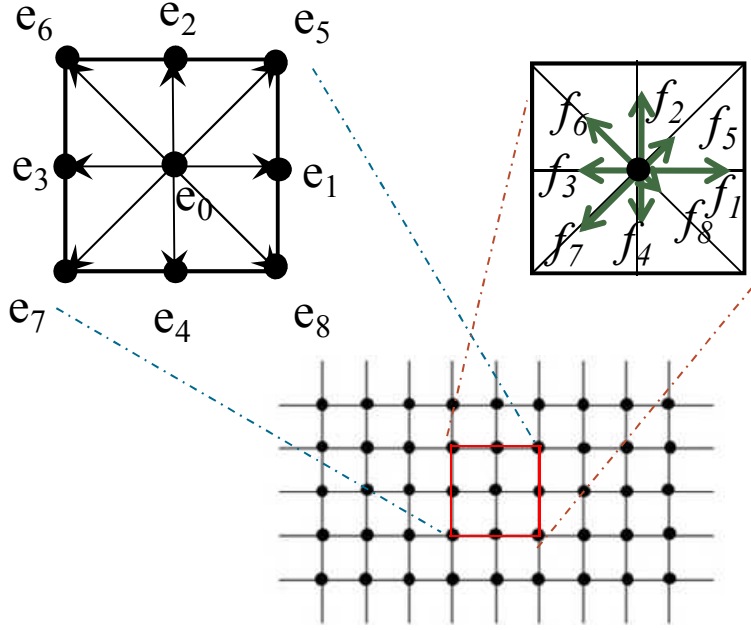


Fig. 2-1 D2Q9 lattice, velocities  $e_i$  and particle distribution function  $f_i$ .

In a two-phase lattice Boltzmann model proposed by Lee and Lin [42], two particle distribution functions are utilized. In their model, the time evolution equations of particles distribution functions are expressed as

$$\frac{\partial f_i}{\partial t} + e_{\alpha i} \frac{\partial f_i}{\partial x_\alpha} = -\frac{1}{\lambda} (f_i - f_i^{eq}) + \frac{(e_{\alpha i} - u_\alpha)(\partial_\alpha \rho c_s^2 - \rho \partial_\alpha (\varphi - k \partial_\beta^2 \rho))}{c_s^2} \Gamma_i(\mathbf{u}) \quad (2-2)$$

$$\frac{\partial g_i}{\partial t} + e_{\alpha i} \frac{\partial g_i}{\partial x_\alpha} = -\frac{1}{\lambda} (g_i - g_i^{eq}) + \frac{(e_{\alpha i} - u_\alpha) \partial_\alpha (\rho c_s^2 - P)}{c_s^2} (\Gamma_i(\mathbf{u}) - \Gamma_i(0)) \quad (2-3)$$

where  $f_i$  is a particle distribution function in  $i$  direction on the lattice and is related to the order parameter,  $g_i$  is a particle distribution function for hydrodynamic pressure and momentum,  $P$  is modified pressure,  $\rho$  and  $u_\alpha$  are the density and velocity of two-phase fluids, respectively.  $e_{\alpha i}$  is the  $\alpha$ -component of the  $i$  direction microscopic velocity. In Eq. (2-2),  $k$  is a constant parameter determining the interface width  $D$  and the dimensionless surface tension  $\sigma_{LG}$  related to the magnitude of the surface tension force. The reference speed of sound  $c_s^2 = 1/3$ ,  $\lambda$  is the relaxation time due to collision. The equilibrium distribution functions  $f_i^{eq}$  and  $g_i^{eq}$  are corresponding equilibrium states of  $f_i$  and  $g_i$  and are given as

$$f_i^{eq} = t_i \rho \left[ 1 + \frac{e_{\alpha i} u_{\alpha}}{c_s^2} + \frac{(e_{\alpha i} e_{\beta i} - c_s^2 \delta_{\alpha \beta}) u_{\alpha} u_{\beta}}{2c_s^4} \right] \quad (2-4)$$

$$g_i^{eq} = t_i \left[ \frac{P}{c_s^2} + \rho \left( \frac{e_{\alpha i} u_{\alpha}}{c_s^2} \right) + \frac{(e_{\alpha i} e_{\beta i} - c_s^2 \delta_{\alpha \beta}) u_{\alpha} u_{\beta}}{2c_s^4} \right] \quad (2-5)$$

where  $t_i$  is the weighting factor,  $\delta_{\alpha \beta}$  is the Kronecker delta.  $\Gamma_i$  in Eq. (2-2) is expressed as

$$\Gamma_i = t_i \left[ 1 + \frac{e_{\alpha i} u_{\alpha}}{c_s^2} + \frac{(e_{\alpha i} e_{\beta i} - c_s^2 \delta_{\alpha \beta}) u_{\alpha} u_{\beta}}{2c_s^4} \right] \quad (2-6)$$

$\phi(\rho)$  is the chemical potential and takes the form of

$$\phi(\rho) = 4\beta(\rho - \rho_G)(\rho - \rho_L)(\rho - \rho_M) \quad (2-7)$$

where  $\rho_L$  and  $\rho_G$  are the density of liquid and gas phases at saturation, respectively.  $\beta$  is a constant relating to the interfacial thickness and  $\rho_M = (\rho_L + \rho_G)/2$ .

In a plane interface at an equilibrium condition, the density profile across the interface at equilibrium can be represented as

$$\rho(z) = \frac{\rho_L + \rho_G}{2} + \frac{\rho_L - \rho_G}{2} \tanh\left(\frac{2z}{D}\right) \quad (2-8)$$

where  $z$  is the direction normal to the interface. The interface thickness  $D$  is give by

$$D = \frac{4}{\rho_L - \rho_G} \sqrt{\frac{k}{2\beta}} \quad (2-9)$$

The dimensionless surface tension force  $\sigma_{LG}$  is given by

$$\sigma_{LG} = \frac{(\rho_L - \rho_G)^3}{6} \sqrt{2k\beta} \quad (2-10)$$

The above LBEs are solved in two steps: collision (pre-streaming collision and post-streaming collision steps) and streaming steps.

Pre-streaming collision step:

$$\bar{f}_i(\mathbf{x}, t) = f_i(\mathbf{x}, t) - \frac{1}{2\tau} (f_i - f_i^{eq}) \Big|_{(\mathbf{x}, t)} + \frac{\delta t}{2} \frac{(e_{\alpha i} - u_{\alpha}) [\partial_{\alpha} \rho c_s^2 - \rho \partial_{\alpha} (\phi - k \partial_{\gamma}^2 \rho)]}{c_s^2} \Big|_{\Gamma_i(\mathbf{u})} \Big|_{(\mathbf{x}, t)} \quad (2-11)$$

$$\begin{aligned}\bar{g}_i(\mathbf{x}, t) = & g_i(\mathbf{x}, t) - \frac{1}{2\tau} \left( g_i - g_i^{eq} \right) \Big|_{(\mathbf{x}, t)} + \frac{\delta t}{2} \frac{(e_{ai} - u_\alpha) \partial_\alpha \rho c_s^2}{c_s^2} \left[ \Gamma_i(\mathbf{u}) - \Gamma_i(0) \right] \Big|_{(\mathbf{x}, t)} \\ & + \frac{\delta t}{2} \frac{(e_{ai} - u_\alpha) \left[ k \partial_\alpha (\partial_\gamma \rho \partial_\gamma \rho) - k \partial_\beta (\partial_\alpha \rho \partial_\beta \rho) \right]}{c_s^2} \Gamma_i(\mathbf{u}) \Big|_{(\mathbf{x}, t)}\end{aligned}\quad (2-12)$$

Streaming step:

$$\bar{f}_i(\mathbf{x} + e_{ai} \Delta t, t + \Delta t) = \bar{f}_i(\mathbf{x}, t) \quad (2-13)$$

$$\bar{g}_i(\mathbf{x} + e_{ai} \Delta t, t + \Delta t) = \bar{g}_i(\mathbf{x}, t) \quad (2-14)$$

Post-streaming collision step:

$$\begin{aligned}f_i(\mathbf{x} + e_{ai} \Delta t, t + \Delta t) = & \bar{f}_i(\mathbf{x} + e_{ai} \Delta t, t + \Delta t) - \frac{1}{2\tau + 1} \left( \bar{f}_i - f_i^{eq} \right) \Big|_{(\mathbf{x} + e_{ai} \Delta t, t + \Delta t)} \\ & + \frac{2\tau}{2\tau + 1} \frac{\Delta t}{2} \frac{(e_{ai} - u_\alpha) \left[ \partial_\alpha \rho c_s^2 - \rho \partial_\alpha (\varphi - k \partial_\gamma^2 \rho) \right]}{c_s^2} \Gamma_i(\mathbf{u}) \Big|_{(\mathbf{x} + e_{ai} \Delta t, t + \Delta t)}\end{aligned}\quad (2-15)$$

$$\begin{aligned}g_i(\mathbf{x} + e_{ai} \Delta t, t + \Delta t) = & \bar{g}_i(\mathbf{x} + e_{ai} \Delta t, t + \Delta t) g_i(\mathbf{x}, t) - \frac{1}{2\tau + 1} \left( \bar{g}_i - g_i^{eq} \right) \Big|_{(\mathbf{x} + e_{ai} \Delta t, t + \Delta t)} \\ & + \frac{2\tau}{2\tau + 1} \frac{\Delta t}{2} \frac{(e_{ai} - u_\alpha) \partial_\alpha \rho c_s^2}{c_s^2} \left[ \Gamma_i(\mathbf{u}) - \Gamma_i(0) \right] \Big|_{(\mathbf{x} + e_{ai} \Delta t, t + \Delta t)} \\ & + \frac{2\tau}{2\tau + 1} \frac{\Delta t}{2} \frac{(e_{ai} - u_\alpha) \left[ k \partial_\alpha (\partial_\gamma \rho \partial_\gamma \rho) - k \partial_\beta (\partial_\alpha \rho \partial_\beta \rho) \right]}{c_s^2} \Gamma_i(\mathbf{u}) \Big|_{(\mathbf{x} + e_{ai} \Delta t, t + \Delta t)}\end{aligned}\quad (2-16)$$

where  $\Delta t$  is the time step during which the particles travel through the lattice spacing.  $\tau$  is a relaxation time which can be expressed as  $\tau = \lambda / \Delta t$ . The relaxation time  $\tau$  is assumed to linearly depend on the density in the interface region as follows:

$$\tau = c \tau_L - (1 - c) \tau_G \quad (2-17)$$

where  $\tau_L$  and  $\tau_G$  are the relaxation time for liquid and gas phase, respectively.  $c$  is expressed as  $c = (\rho - \rho_G) / (\rho_L - \rho_G)$ . The viscosity is given by  $\mu = \rho \tau c_s^2 \Delta t$ .

Density, velocity and hydrodynamic pressure are calculated using the particle distribution functions after the streaming step as follows:

$$\rho = \sum_i \bar{f}_i \quad (2-18)$$

$$\rho u_\alpha = \sum_i e_{\alpha i} \bar{g}_i + \frac{\delta t}{2} k \left[ \frac{\partial}{\partial x_\alpha} \left( \frac{\partial \rho}{\partial x_\gamma} \frac{\partial \rho}{\partial x_\gamma} \right) - \frac{\partial}{\partial x_\beta} \left( \frac{\partial \rho}{\partial x_\alpha} \frac{\partial \rho}{\partial x_\beta} \right) \right] + \frac{\delta t}{2} (F_g + F_{ad}) \quad (2-19)$$

$$P = c_s^2 \sum_i \bar{g}_i + \frac{\delta t}{2} u_\alpha \frac{\partial \rho c_s^2}{\partial x_\alpha} \quad (2-20)$$

The first and second derivatives of density are calculated at node  $(i, j)$ , respectively [42]:

$$\left. \frac{\partial \rho}{\partial x} \right|_{(i,j)} = [\rho(i+1, j) - \rho(i-1, j)]/3 + [\rho(i+1, j+1) - \rho(i-1, j+1)]/12 + [\rho(i+1, j-1) - \rho(i-1, j-1)]/12 \quad (2-21)$$

$$\left. \frac{\partial \rho}{\partial y} \right|_{(i,j)} = [\rho(i, j+1) - \rho(i, j-1)]/3 + [\rho(i+1, j+1) - \rho(i-1, j+1)]/12 + [\rho(i-1, j+1) - \rho(i+1, j-1)]/12 \quad (2-22)$$

and

$$\begin{aligned} \left. \frac{\partial^2 \rho}{\partial x^2} \right|_{(i,j)} &= [\rho(i+1, j+1) + \rho(i-1, j+1) + \rho(i+1, j-1) + \rho(i-1, j-1) \\ &\quad + 4\rho(i+1, j) + 4\rho(i-1, j) + 4\rho(i, j+1) + 4\rho(i, j-1) - 20\rho(i, j)]/6 \end{aligned} \quad (2-23)$$

### 2.2.2 Inamuro model

In the two-phase LBM model proposed by Inamuro *et al.* [43], two particle distribution functions,  $f_i$  and  $g_i$  are employed. The function  $f_i$  is used to calculate the order parameter  $\phi$  which distinguishes the two phases, while the function  $g_i$  is used to calculate the predicted velocity of the two-phase flows without a pressure gradient. The time evolution of the particle distribution functions  $f_i(x, t)$  and  $g_i(x, t)$  at position  $x$  and time  $t$  are given as follows:

$$f_i(\mathbf{x}_\alpha + \mathbf{e}_{i\alpha} \Delta x, t + \Delta t) = f_i(\mathbf{x}_\alpha, t) - \frac{1}{\tau_f} [f_i(\mathbf{x}_\alpha, t) - f_i^{eq}(\mathbf{x}_\alpha, t)] \quad (2-24)$$

$$g_i(\mathbf{x}_\alpha + \mathbf{e}_{i\alpha} \Delta x, t + \Delta t) = g_i(\mathbf{x}_\alpha, t) - \frac{1}{\tau_g} [g_i(\mathbf{x}_\alpha, t) - g_i^{eq}(\mathbf{x}_\alpha, t)] + 3W_i e_{i\alpha} \frac{\Delta x}{\rho} \frac{\partial}{\partial x_\beta} \left\{ \mu \left( \frac{\partial u_\beta}{\partial x_\alpha} + \frac{\partial u_\alpha}{\partial x_\beta} \right) \right\} \quad (2-25)$$

where  $\tau_f=1$  and  $\tau_g=1$  are single relaxation times,  $\Delta x$  is a spacing of the square lattice and  $\mu$  is viscosity.  $f_i^{eq}$  and  $g_i^{eq}$  are expressed as follows [44, 45]:

$$f_i^{eq}(\mathbf{x}_\alpha, t) = H_i \phi + F_i \left[ p_0 - k \phi \frac{\partial^2 \phi}{\partial x_\alpha^2} \right] + 3W_i \phi e_{i\alpha} u_\alpha + W_i k G_{\alpha\beta}(\phi) e_{i\alpha} e_{i\beta} \quad (2-26)$$

$$g_i^{eq}(\mathbf{x}_\alpha, t) = W_i \left[ 1 + 3e_{i\alpha} u_\alpha - \frac{3}{2} u_\alpha u_\alpha + \frac{9}{2} e_{i\alpha} e_{i\beta} u_\alpha u_\beta + \frac{3}{4} \Delta x \left( \frac{\partial u_\beta}{\partial x_\alpha} + \frac{\partial u_\alpha}{\partial x_\beta} \right) e_{i\alpha} e_{i\beta} \right] + W_i \frac{k}{\rho} G_{\alpha\beta}(\phi) e_{i\alpha} e_{i\beta} - \frac{1}{2} F_i \frac{k}{\rho} \left( \frac{\partial \phi}{\partial x_\alpha} \right)^2 \quad (2-27)$$

where  $G_{\alpha\beta}(\phi)$  is given as

$$G_{\alpha\beta}(\phi) = \frac{9}{2} \frac{\partial \phi}{\partial x_\alpha} \frac{\partial \phi}{\partial x_\beta} - \frac{9}{4} \frac{\partial \phi}{\partial x_\gamma} \frac{\partial \phi}{\partial x_\gamma} \delta_{\alpha\beta} \quad (2-28)$$

and the weighting factors of  $H_i$ ,  $W_i$  and  $F_i$  are presented as

$$\begin{aligned} H_0 &= 1, H_1 = H_2 = \dots = H_8 = 0, \\ W_0 &= 4/9, W_1 = W_2 = W_3 = W_4 = 1/9, W_5 = W_6 = W_7 = W_8 = 1/36, \\ F_0 &= -5/3, F_i = 3W_i \ (i = 1, 2, \dots, 8) \end{aligned} \quad (2-29)$$

The first and second derivatives are calculated by using the following second-order finite difference approximations:

$$\frac{\partial \varpi}{\partial x_\alpha} = \frac{1}{6\Delta x} \sum_{i=1}^8 e_{i\alpha} \varpi(\mathbf{x}_\alpha + \mathbf{e}_{i\alpha} \Delta x) \quad (2-30)$$

$$\frac{\partial^2 \varpi}{\partial x_\alpha^2} = \frac{1}{3(\Delta x)^2} \left[ \sum_{i=1}^8 \varpi(\mathbf{x}_\alpha + \mathbf{e}_{i\alpha} \Delta x) - 8\varpi(\mathbf{x}_\alpha) \right] \quad (2-31)$$

where  $\varpi$  is an arbitrary variable  $\mathbf{u}_\alpha$  or  $\phi$ . The parameter  $p_0$  is given by as follows [45]:

$$p_0 = \phi \frac{\partial \psi}{\partial \phi} - \psi = \beta(\phi - \phi_L)(\phi - \phi_G)(3\phi^2 - \phi\phi_L - \phi\phi_G - \phi_L\phi_G) + p_b \quad (2-32)$$

where  $\psi$  is the bulk free-energy density and takes the following simple form in an isothermal system:

$$\psi(\phi) = \beta(\phi - \phi_G)^2(\phi - \phi_L)^2 + \phi_b\phi - p_b \quad (2-33)$$

where  $\phi_L$  and  $\phi_G$  are the order parameters for liquid and gas phase,  $\phi_b$  and  $p_b$  ( $p_b = \beta\phi_L^2\phi_G^2$ ) are the bulk chemical potential and bulk pressure, respectively [46-48].

In a plane interface at an equilibrium condition, the density profile across the interface can be represented as

$$\psi(z) = \frac{\phi_L + \phi_G}{2} + \frac{\phi_L - \phi_G}{2} \tanh\left(\frac{2z}{D}\right) \quad (2-34)$$

where  $z$  is the direction normal to the interface. The interface thickness  $D$  is give by

$$D = \frac{4}{\phi_L - \phi_G} \sqrt{\frac{k}{2\beta}} \quad (2-35)$$



The dimensionless surface tension parameter between liquid and gas phase,  $\sigma_{LG}$ , is expressed as [88]

$$\sigma_{LG} = \frac{(\phi_L - \phi_G)^3}{6} \sqrt{2k\beta} \quad (2-36)$$

The macroscopic variables,  $\phi$ ,  $\mathbf{u}_\alpha^*$ ,  $\rho$  and  $\mu$  can be evaluated as

$$\phi = \sum_{i=0}^8 f_i, \quad \mathbf{u}_\alpha^* = \sum_{i=0}^8 \mathbf{e}_{i\alpha} g_i \quad (2-37)$$

$$\rho = \begin{cases} \rho_G, & \phi < \phi_G \\ \frac{\phi - \phi_G}{\phi_L - \phi_G} (\rho_L - \rho_G) + \rho_G, & \phi_G \leq \phi \leq \phi_L \\ \rho_L, & \phi > \phi_L \end{cases} \quad (2-38)$$

$$\mu = \frac{\rho - \rho_G}{\rho_L - \rho_G} (\mu_L - \mu_G) + \mu_G \quad (2-39)$$

The predicted velocity  $\mathbf{u}_\alpha^*$  does not satisfy a divergence free condition, so  $\mathbf{u}_\alpha^*$  should be corrected to satisfy the continuity equation. The corrected velocity  $\mathbf{u}_\alpha$  can be obtained by solving the following equation:

$$\mathbf{u}_\alpha - \mathbf{u}_\alpha^* = -\frac{\nabla p}{\rho} \quad (2-40)$$

The pressure  $p$  is calculated by using the evolution equation of velocity distribution function  $h_i$ :

$$h_i^{n+1}(x + e_i \Delta x) = h_i^n(x) - \frac{1}{\tau_h} [h_i^n(x) - W_i p^n(x)] - \frac{1}{3} W_i \frac{\partial \mathbf{u}_\alpha^*}{\partial x_\alpha} \quad (2-41)$$

where  $n$  is the number of iterations,  $\tau_h$  is the relaxation time given by  $\tau_h = 1/\rho + 1/2$ .  $p$  is obtained by

$$p^{n+1} = \sum_{i=0}^8 h_i^{n+1} \quad (2-42)$$

The convergent pressure  $p$  of Eq. (2-41) is iterated until  $|p^{n+1} - p^n|/\rho < \varepsilon$  is satisfied in the whole computational domain. The tolerance  $\varepsilon$  is set to  $1.0 \times 10^{-6}$  in the present study. By substituting the newly obtained pressure  $p$  into Eq. (2-40), the corrected velocity  $\mathbf{u}_\alpha$  is obtained.

## 2.3 Boundary conditions

To develop an accurate computation scheme, efficient boundary conditions is important. This is because boundary conditions will influence the accuracy and stability of the computation. In this section, three kinds of boundary conditions, cyclic boundary condition, bounce back condition and mass conserving solid wall boundary condition, are introduced.

### 2.3.1 Cyclic boundary condition

The cyclic boundary condition would be applied to the ‘open’ ends of the slit. Fig. 2-2 illustrates the cyclic boundary conditions when the flow transfer out of the region of lattice boundary  $x = 0$  and  $L_x$ . For example, the flow point is on the left of line  $x = 0$  and on the right of line  $x = L_x$ . Now, the flow point on the left of line  $x = 0$  is discussed. The node is expressed as  $(i, j)$ . When the distributions functions are unknown on the line  $x = i-1$ , the cyclic boundary condition is given as:

$$f(i-1, j) = f(L_x, j) \quad (2-43)$$

For the flow on the right end line  $x = L_x$  have the similar condition. The distribution functions are unknown on the line  $x = L_x + 1$ , thus, the cyclic boundary condition is given as:

$$f(i+1, j) = f(0, j) \quad (2-44)$$

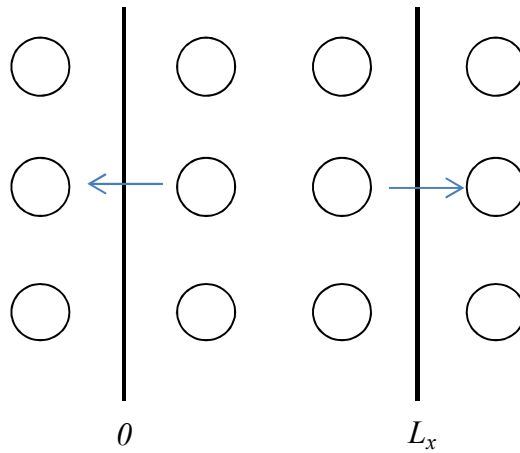


Fig. 2-2 Cyclic boundary condition.

### 2.3.2 Bounce back condition

Bounce back boundary condition is widely applied to traditional CFD methods to simulate the flow colliding with a solid wall. The fullway bounce back method of stationary

boundary will be introduced at here, which is shown in Fig. 2-3. Now, let consider  $x = 0$  and  $x = L_x$  as solid wall. For  $x = 0$ , the magnitude of particle distribution functions  $f_5, f_1$  and  $f_8$  is unknown which are given by  $f_7, f_3$  and  $f_6$  from streaming process, respectively. The boundary condition can be expressed by

$$\begin{aligned} f_5 &= f_7, \\ f_1 &= f_3 \\ f_8 &= f_6 \end{aligned} \quad (2-45)$$

For  $x = L_x$ , the  $f_7 = f_5, f_3 = f_1$  and  $f_6 = f_8$ , where  $f_5, f_1$  and  $f_8$  are known from streaming process.

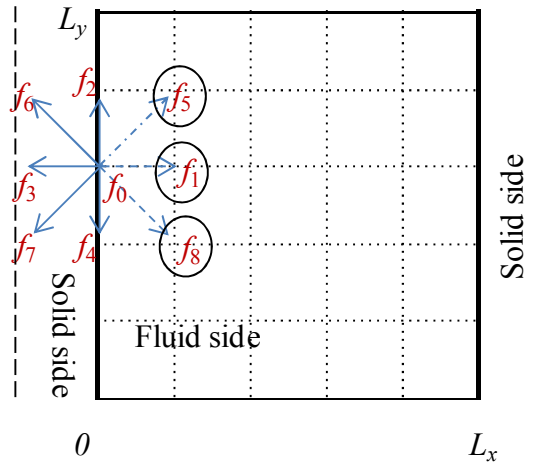


Fig. 2-3 Bounce boundary conditions.

### 2.3.3 Mass conserving solid wall boundary condition

A boundary condition that can prevent the leakage of mass in a given system is greatly important for LB simulations. Bao *et al.* [89] proposed a mass conserving solid wall boundary condition which is based on a curved wall boundary condition proposed by Filippova and Hänel (FH boundary condition) [90] and Mei *et al.* (MLS boundary condition) [91, 92].

FH boundary condition is briefly introduced in here. As shown in Fig. 2-4,  $\mathbf{e}_{\bar{a}}$  and  $\mathbf{e}_a$  denote the directions opposite to each other,  $\mathbf{x}_b$  is a boundary node,  $\mathbf{x}_f$  is a fluid node. The curved wall is located between boundary and fluid nodes. In order to terminate the streaming step,  $\tilde{f}_\alpha(\mathbf{x}_b, t)$  at the boundary node  $\mathbf{x}_b$  should be known, where  $\tilde{f}_\alpha$  denotes the post-collision

state of the distribution function. Thus, the total mass is conserved. In FH model, the following treatment for  $\tilde{f}_\alpha(\mathbf{x}_b, t)$  is forced on curved boundaries.

$$\tilde{f}_\alpha^-(\mathbf{x}_b, t) = (1 - \chi) \tilde{f}_\alpha^-(\mathbf{x}_f, t) + \chi f_\alpha^*(\mathbf{x}_b, t) + 2w_\alpha \rho \frac{\mathbf{e}_\alpha^- \cdot \mathbf{u}_w}{c_s^2} \quad (2-46)$$

where  $\mathbf{u}_w = \mathbf{u}(\mathbf{x}_w, t)$  is the velocity at the wall,  $\chi$  is the weighting factor that controls the linear interpolation between  $\tilde{f}_\alpha(\mathbf{x}_f, t)$  and  $f_\alpha^*(\mathbf{x}_b, t)$  (Filipova and Hänel, 1998) [90]. In this study,  $\mathbf{u}_{bf}$  is chosen to equal with  $\mathbf{u}_f$ , where  $\mathbf{u}_f$  is fluid velocity near the wall.  $\rho(\mathbf{x}_w, t)$  is wall density. When  $\mathbf{u}_w = 0$ , and  $\chi = 0$  are chosen, therefore, Eq. (2-46) becomes  $\tilde{f}_\alpha(\mathbf{x}_b, t) = \tilde{f}_\alpha(\mathbf{x}_f, t)$ .

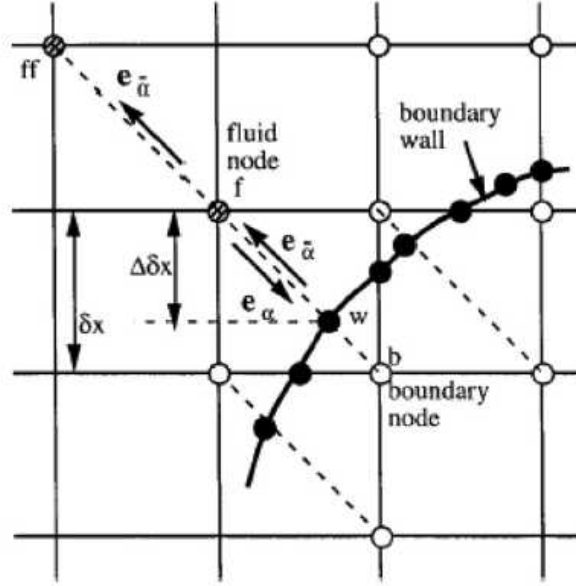


Fig. 2-4 Layout of the lattice and curved wall boundary [91].

The fictitious equilibrium distribution  $f_\alpha^*(\mathbf{x}_b, t)$  term is responsible to guarantee mass conservation [89]

$$f_\alpha^*(\mathbf{x}_b, t) = w_\alpha \rho(\mathbf{x}_w, t) \left[ 1 + \frac{\mathbf{e}_\alpha \mathbf{u}_{bf}}{c_s^2} + \frac{(\mathbf{e}_\alpha \mathbf{u}_f)^2}{2c_s^4} - \frac{\mathbf{u}_f \mathbf{u}_f}{2c_s^2} \right] \quad (2-47)$$

and

$$\rho(\mathbf{x}_w, t) = 6 \frac{f_4 + f_7 + f_8}{1 - 3\mathbf{u}_{bf}^y + 3(\mathbf{u}_f^y)^2} \quad (2-48)$$

where  $\mathbf{u}_{bf}^y$  is the y-component of  $\mathbf{u}_{bf}$  and  $\mathbf{u}_f^y$  is the y-component of  $\mathbf{u}_f$ .  $f_4, f_7$  and  $f_8$  are outgoing particle distribution functions which are known. Fig. 2-5 shows the known ( $f_4, f_7$  and  $f_8$ ) and

unknown ( $f_2$ ,  $f_5$  and  $f_6$ ) particles distribution functions of a flat boundary at the lower wall boundary after the streaming step. Then, by substituting the expression of  $\rho(\mathbf{x}_w, t)$  into Eq. (2-47), the unknown particle  $f_2$ ,  $f_5$  and  $f_6$  can be obtained. It is straightforward to show that this boundary treatment satisfies the condition:  $\sum_{outgoing} f = \sum_{incoming} f$ .

When  $\mathbf{u}_{bf}$  is chosen to equal with  $\mathbf{u}_f$ , thus,  $f_\alpha^*(\mathbf{x}_b, t) \approx f_\alpha^{(eq)}(\mathbf{x}_f, t) = f_\alpha(\mathbf{x}_f, t)$  [89]. Then, mass conserving solid wall boundary conditions at lower wall are expressed by particle distribution function as

$$\begin{aligned} \tilde{f}_2(\mathbf{x}_b, t) &= f_4^*(\mathbf{x}_b, t) \\ \tilde{f}_5(\mathbf{x}_b, t) &= f_7^*(\mathbf{x}_b, t) \\ \tilde{f}_6(\mathbf{x}_b, t) &= f_8^*(\mathbf{x}_b, t) \end{aligned} \quad (2-49)$$

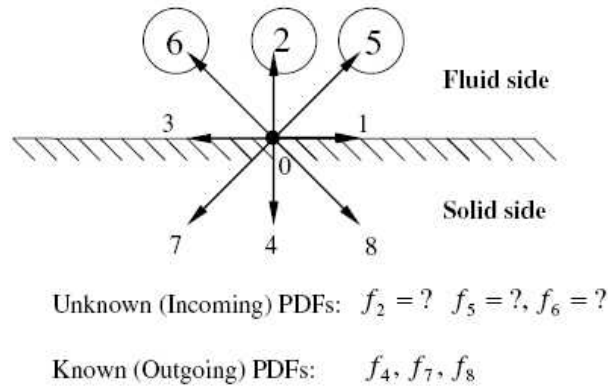


Fig. 2-5 Particles distribution functions of a flat boundary site at the lower wall boundary after the streaming step [89].

## 2.4 Wetting model

In this section, two kinds of wetting model, adhesive force model and a partial wetting boundary condition, are introduced at first. These wetting models can be incorporated into different LB models to give the wettability of substrates. The magnitude of static contact angle of a droplet on homogenous substrate will be a standard of the substrate wettability. In case of the static contact angle of  $\theta_c < 90^\circ$ , the droplet is on hydrophilic substrate. In contrast, in case of  $\theta_c > 90^\circ$ , the droplet is on hydrophobic substrate.

### 2.4.1 Adhesive force model

To take into account the wettability of the substrate, the fluid-solid surface force is described by Eq. (2-50) [66]

$$F_{ad}(\mathbf{x}, t) = -E(\mathbf{x}, t) \sum_{\alpha} G_{\alpha} s(\mathbf{x} + \mathbf{e}_{\alpha} \Delta t) \mathbf{e}_{\alpha} \quad (2-50)$$

where  $s = 1$  or  $0$  for a solid or fluid site at  $\mathbf{x} + \mathbf{e}_{\alpha} \Delta t$ .  $E$  is the interaction potential which can be chosen the form with flexibility. In the present study,  $E$  has the following equation form.

$$E(\mathbf{x}, t) = 0.5(\tau - \tau_l) / \tau \quad (2-51)$$

The  $G_{\alpha}$  is the direction-dependent weighting factor and defined as

$$G_{\alpha} = \begin{cases} 4G_{ad} & |\mathbf{e}_{\alpha}| = 1 \\ G_{ad} & |\mathbf{e}_{\alpha}| = \sqrt{2} \\ 0, & |\mathbf{e}_{\alpha}| = 0 \end{cases} \quad (2-52)$$

By adjusting the interaction strength parameter  $G_{ad}$  for the fluid, the wettability of substrates is given.

### 2.4.2 Partial wetting boundary condition [45, 46]

A partial wetting boundary condition based on the free energy of the fluid-solid interaction is imposed on the lattice sites of the wall surface by using the derivatives of the order parameter normal to the wall.

A one-dimensional problem where one phase of the nonideal fluid occupies the region  $y > 0$  with a solid wall  $y = 0$  is considered, and the derivative of the order parameter on the wall is expressed by

$$k \left( \frac{d\phi}{dy} \right) = \frac{d\Phi(\phi_s)}{d\phi_s} = -\lambda \quad (2-53)$$

where  $\phi_s$  is the order parameter on the wall,  $\Phi(\phi_s)$  is the contribution of the fluid-solid interaction to the surface energy, and  $\lambda$  is a constant that is obtained from a wetting potential  $\Omega$ ,

$$\Omega = \frac{4\lambda}{(\phi_L - \phi_G)^2 \sqrt{2k\beta}} \quad (2-54)$$

In addition,  $\Omega$  can be obtained for a given contact angle as

$$\Omega = 2 \operatorname{sgn}\left(\frac{\pi}{2} - \theta_c\right) \left\{ \cos\left(\frac{\gamma}{3}\right) \left[ 1 - \cos\left(\frac{\gamma}{3}\right) \right] \right\}^{1/2} \quad (2-55)$$

where  $\gamma = \arccos(\sin^2 \theta_c)$ . In order to introduce a partial wetting boundary condition in the lattice Boltzmann simulation, the following boundary conditions are imposed on the lattice sites through the equilibrium distribution functions  $f_i^{\text{eq}}$  and  $g_i^{\text{eq}}$  as follows:

$$\left. \frac{\partial \phi}{\partial y} \right|_{y=0} = -\frac{\lambda}{k} \quad (2-56)$$

$$\left. \frac{\partial^2 \phi}{\partial y^2} \right|_{y=0} \approx \frac{1}{2} \left( -3 \left. \frac{\partial \phi}{\partial y} \right|_{y=0} + 4 \left. \frac{\partial \phi}{\partial y} \right|_{y=1} - \left. \frac{\partial \phi}{\partial y} \right|_{y=2} \right) \quad (2-57)$$

### 2.4.3 Spread of droplet on substrate

Numerical simulations are carried out for a droplet on a homogenous substrate. Initial volume of the droplet is set to  $\pi d_w^3/12$ . When the shape of the droplet reaches to a corresponding equilibrium state, the contact angle of the droplet is calculated using the wetting diameter  $d_w$  and the height  $h$  as follows:

$$\theta_c = \arcsin\left(\frac{d_w h}{(d_w/2)^2 + h^2}\right) \quad (2-58)$$

The spread of droplet on homogenous substrate is checked for each wetting model to demonstrate that the wetting models can reproduce the wettability correctly in the present simulation.

The physical problem and computational domain of a droplet on a homogeneous substrate are shown in Fig. 2-6. The computational domain is a two-dimensional Cartesian coordinate system and is divided into  $L_x \times L_y$  lattices. The lattices size are given as  $400 \times 150$  for the adhesive force model incorporated into the LB model proposed by Lee and Lin [42], whereas the lattices size are given as  $80 \times 30$  for the partial wetting boundary condition incorporated into the LB model proposed by Inamuro *et al.* [43].

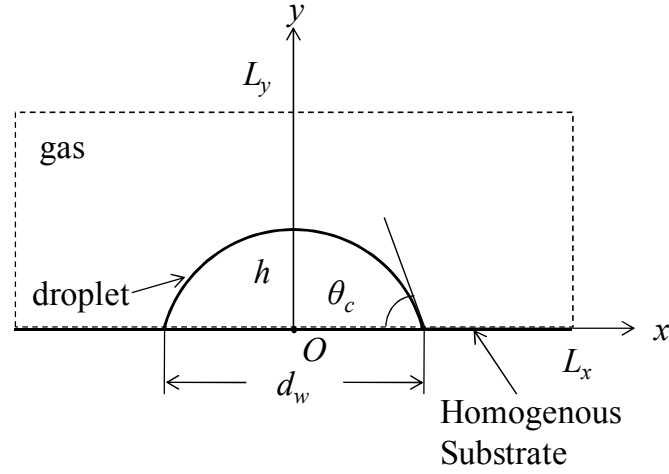


Fig. 2-6 Physical problem and computational domain of droplet on homogenous substrates.

Adhesive force model is incorporated into the LB model proposed by Lee and Lin [42]. The computational conditions are shown in the simulation parameters (a) of Table 2-1. The partial wetting boundary condition is incorporated into the LB model proposed by Inamuro *et al.* [43]. The computational conditions are shown in the simulation parameters (b) of Table 2-1.

Table 2-1 Computational conditions

	Simulation parameters (a)	Simulation parameters (b)	Physical properties
$\rho_L$	1.0	1000	1000 kg m <sup>-3</sup>
$\rho_G$	$1.2 \times 10^{-3}$	1.29	1.29 kg m <sup>-3</sup>
$\phi_L$	-	0.4	-
$\phi_G$	-	0.1	-
$\mu_L/\mu_G$	55.6	55.6	55.6
$\sigma_{LG}$	$2.09 \times 10^{-3}$	$5.0 \times 10^{-3}$	$7.2 \times 10^{-2}$ N m <sup>-1</sup>
$D$	12	3	-
$d_w$	100	20	$2.0 \times 10^{-4}$ m
$g$	$1.14 \times 10^{-9}$	$6.8 \times 10^{-9}$	9.8 m s <sup>-2</sup>



In these simulations, the Ohnesorge number ( $Oh = \mu_L / (\rho_L \sigma_{LG} (d_w/2)^{0.5})$ ) and the Bond number ( $Bo = (\rho_L - \rho_G) g_r (d_w/2)^2 / \sigma_{LG}$ ) are set to  $1.18 \times 10^{-2}$  and  $1.36 \times 10^{-3}$ , respectively.

To test the validity of these wetting models, the spread of a droplet on homogenous substrate given by the adhesive force model or the partial wetting boundary condition model are simulated, and the results are shown as follows.

Fig. 2-7 shows the calculated shape of the droplet at steady state on the different wettability substrate with  $G_{ad} = -0.003$ , 0 and 0.002 by using the adhesive force model. The contact line motion with time step is affected by adhesive force and gravity, the droplet finally reaches an equilibrium shape with contact angle  $\theta_c = 42.7^\circ$ ,  $90^\circ$  and  $121.8^\circ$ , respectively.

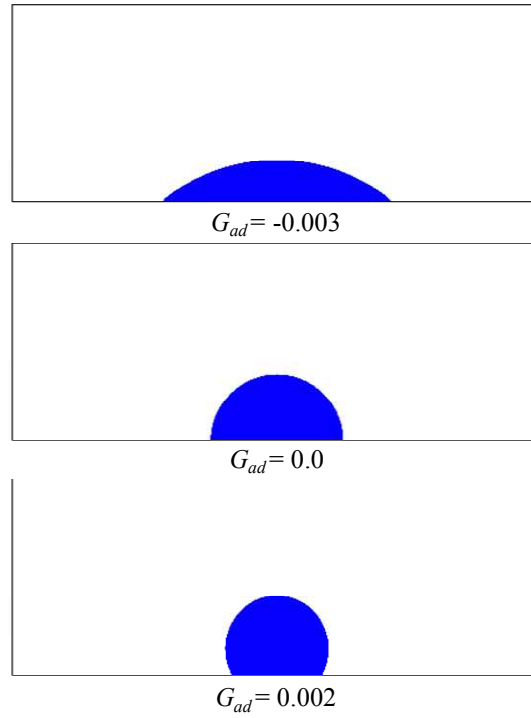


Fig. 2-7 Shape of the droplet at steady state on the uniform substrate with  $G_{ad} = -0.003$ , 0.0 and 0.002

Fig. 2-8 shows a correlation between the static contact angle  $\theta_c$  and interaction strength parameter  $G_{ad}$ . From this figure, the contact angle is given in the range of  $42.7^\circ$  to  $121.8^\circ$  with

the interaction strong parameter  $G_{ad}$  from  $-0.003$  to  $0.002$ . The  $\theta_c$  increases linearly with increasing  $G_{ad}$ . For  $G_{ad} < 0$  and  $G_{ad} > 0$ , the droplet represents the hydrophilic and hydrophobic region of the substrate, respectively. The contact angles are arbitrarily given for the substrate with different wettability. It indicates that the wetting model can be used in the LB model proposed by Lee and Lin [42] as reliable way to control substrate wettability.

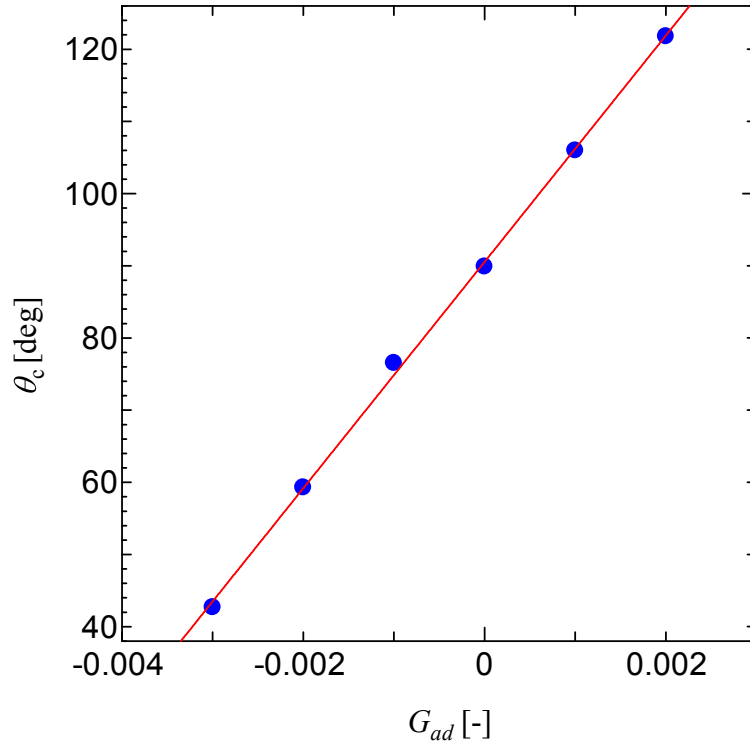


Fig. 2-8 Correlation between static contact angle  $\theta_c$  with interaction strength parameter  $G_{ad}$  in the adhesive force model.

The wettability of substrates is evaluated by imposing a partial wetting boundary condition into the LB model proposed by Inmuro *et al.* [43]. The results of droplet spreaded on homogenous substrate are shown as follows.

Fig.2-9 shows a correlation between the calculated contact angles and the given static contact angles. It can be seen that the calculated contact angles show a good correlation with the given static contact angles in the range  $30^\circ$  to  $120^\circ$ .

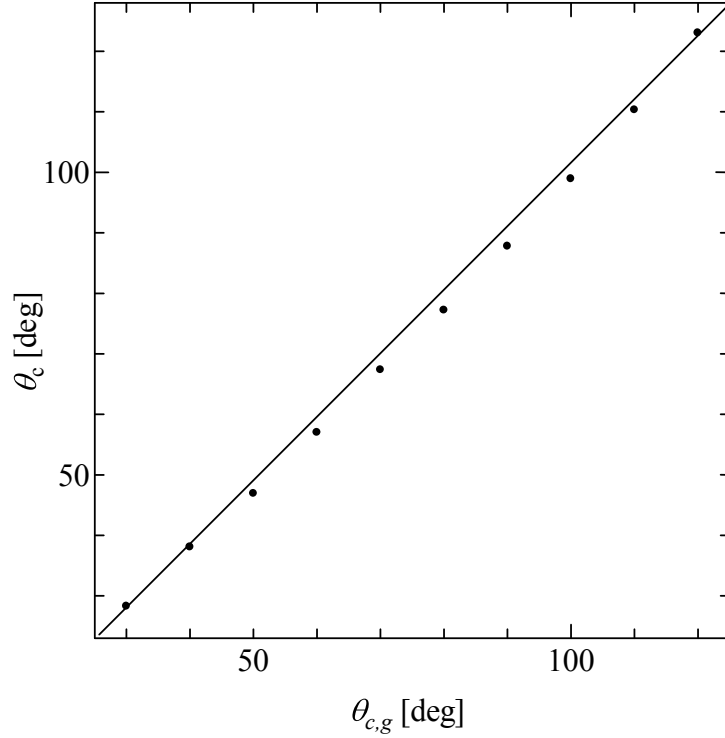


Fig. 2-9 Correlation between the calculated contact angles ( $\theta_c$ ) and the given contact angles ( $\theta_{c,g}$ ) in the partial wetting boundary condition model.

## 2.5 Evaporation Model

To evaluate the evaporation of liquid phase on the droplet surface, an evaporation term is added into the particle distribution function for order parameter as follows.

### 2.5.1 Evaporation model in Lee and Lin's LB model

For the particle distribution function in the two-phase LB model proposed by Lee and Lin [42], the Eq. (2-2) is corrected as Eq. (2-59) by adding the evaporation term

$$\frac{\partial f_i}{\partial t} + e_{\alpha i} \frac{\partial f_i}{\partial x_{\alpha}} = -\frac{1}{\lambda} (f_i - f_i^{eq}) + \frac{(e_{\alpha i} - u_{\alpha})(\partial_{\alpha} \rho x_s^2 - \rho \partial_{\alpha} (\varphi - k \partial_{\beta}^2 \rho))}{c_s^2} \Gamma_i(\mathbf{u}) - \varepsilon_{ev} (f_i^{int}(\mathbf{x}, t) - f_i^G(\mathbf{x}, t)) \quad (2-59)$$

where  $\varepsilon_{ev}$  is an evaporation rate coefficient,  $f_i^{int}(\mathbf{x}, t)$  is the particle distribution function of the order parameter in interface region and  $f_i^G(\mathbf{x}, t)$  is the equilibrium particle distribution function in the gas phase given as  $f_i^G(\mathbf{x}, t) = t_i \rho_L$ . Then, the collision terms of pre-streaming collision and

post-streaming collision steps can be expressed as follows.

Pre-streaming collision step:

$$\begin{aligned} \bar{f}_i(\mathbf{x}, t) = f_i(\mathbf{x}, t) - \frac{1}{2\tau} \left( f_i - f_i^{eq} \right) \Big|_{(\mathbf{x}, t)} + \frac{\delta t (e_{ai} - u_\alpha) [\partial_\alpha \rho c_s^2 - \rho \partial_\alpha (\varphi - k \partial_\gamma^2 \rho)]}{2 c_s^2} \Gamma_i(\mathbf{u}) \Big|_{(\mathbf{x}, t)} \\ - \frac{\Delta t}{2} \varepsilon_{ev} (f_i^{int}(\mathbf{x}, t) - f_i^G(\mathbf{x}, t)) \Big|_{(\mathbf{x}, t)} \end{aligned} \quad (2-60)$$

Post-streaming collision step:

$$\begin{aligned} f_i(\mathbf{x} + e_{ai} \Delta t, t + \Delta t) = \bar{f}_i(\mathbf{x} + e_{ai} \Delta t, t + \Delta t) - \frac{1}{2\tau + 1 + \tau \varepsilon_{ev} \Delta t} \left( \bar{f}_i - f_i^{eq} \right) \Big|_{(\mathbf{x} + e_{ai} \Delta t, t + \Delta t)} \\ + \frac{2\tau}{2\tau + 1 + \tau \varepsilon_{ev} \Delta t} \frac{\Delta t (e_{ai} - u_\alpha) [\partial_\alpha \rho c_s^2 - \rho \partial_\alpha (\varphi - k \partial_\gamma^2 \rho)]}{2 c_s^2} \Gamma_i(\mathbf{u}) \Big|_{(\mathbf{x} + e_{ai} \Delta t, t + \Delta t)} \\ - \frac{\tau \varepsilon_{ev} \Delta t}{2\tau + 1 + \tau \varepsilon_{ev} \Delta t} \left( \bar{f}_i^{int} - f_i^G \right) \Big|_{(\mathbf{x} + e_{ai} \Delta t, t + \Delta t)} \end{aligned} \quad (2-61)$$

### 2.5.2 Evaporation model in the Inamuro's LB model

For the particle distribution function in the two-phase LB model proposed by Inamuro *et al.* [43], the Eq. (2-24) of particle distribution function for order parameter is replaced by Eq. (2-62) by adding the evaporation term.

$$f_i(\mathbf{x}_\alpha + \mathbf{e}_{i\alpha} \Delta x, t + \Delta t) = f_i(\mathbf{x}_\alpha, t) - \frac{1}{\tau_f} [f_i(\mathbf{x}_\alpha, t) - f_i^{eq}(\mathbf{x}_\alpha, t)] - J_s(\mathbf{x}) (f_i^{int}(\mathbf{x}, t) - f_i^G(\mathbf{x}, t)) \quad (2-62)$$

where the equilibrium particle distribution function  $f_i^G(\mathbf{x}, t)$  is in the gas phase region given by Eq. (2-63)

$$f_{i,G}^{eq}(\mathbf{x}, t) = H_i \phi_G + F_i p_b \quad (2-63)$$

$J_s(x)$  in the Eq. (2-62) is the evaporation rate constant to give the local evaporation flux on the droplet surface at the position  $x$ . In the evaporation of a droplet on substrates,  $J_s$  is evaluated from the theoretical prediction [5, 20]

$$J_s(x) = \varepsilon_{ev} (d_w / 2 - x)^{-\chi} \quad (2-64)$$

where  $\varepsilon_{ev}$  is the evaporation rate coefficient,  $d_w$  is the wetting diameter,  $\chi = (\pi - 2\theta_c)/(2\pi - 2\theta_c)$ . For contact angles of  $\theta_c > \pi/2$ ,  $J_s(x)$  is a constant and is equal to the evaporation rate coefficient  $\varepsilon_{ev}$ .

### 2.5.3 Evaporation of a droplet in an ambient vapor

The physical problem and computation domain of a droplet in ambient vapor are shown in Fig. 2-10. The computational domain is a two dimensional Cartesian coordinate system and is divided into  $60 (L_x) \times 60 (L_y)$  lattices in  $x$  and  $y$  directions. A spherical liquid droplet of a radius  $R$  is placed in the center position of the computation domain. The computational conditions are shown in Table 2-1. Inamuro's model is utilized in this calculation.

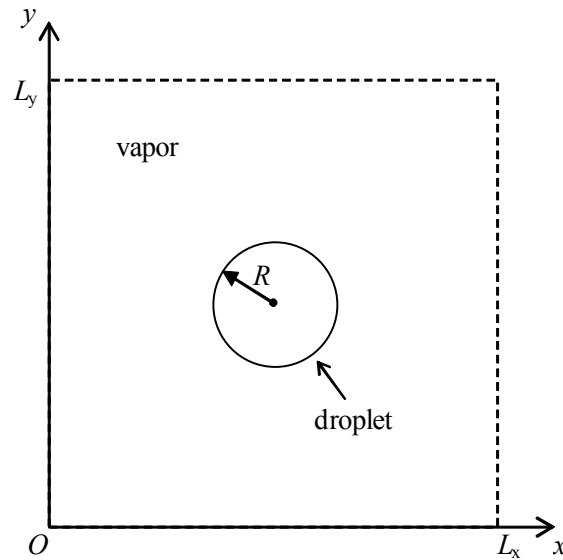


Fig. 2-10 Physical problem and computational domain of a droplet in ambient vapor

Fig. 2-11 shows the evaporation process of a droplet with an evaporation coefficient of  $\varepsilon_{ev} = 1.0 \times 10^{-6}$ . The size of the droplet decreases with increasing time steps and disappears after  $7.8 \times 10^5$  steps.

Fig. 2-12 shows the time variation of the square of the droplet radius,  $R^2$ , for various evaporation rate coefficients.  $R^2$  decreases linearly with time until it reaches about 25. The evaporation of a single droplet in ambient gas has been studied both experimentally and theoretically, and a linear decrease in  $R^2$  with increasing time is known as the classical  $d^2$  law

[93],

$$d^2 \propto d_0^2 - k_{ev}(t - t_0) \quad (2-65)$$

where  $k_{ev}$  is a proportional constant,  $d_0$  is the initial droplet diameter, and  $d$  is the droplet diameter during evaporation. The present numerical result follows the  $d^2$  law during the evaporation until  $R^2$  reaches about 25. However, deviation from the  $d^2$  law is observed when  $R^2$  is smaller than 25. The reason for this deviation may be numerical diffusion when the ratio of the area of interface region to the area occupied by the liquid phase becomes high.

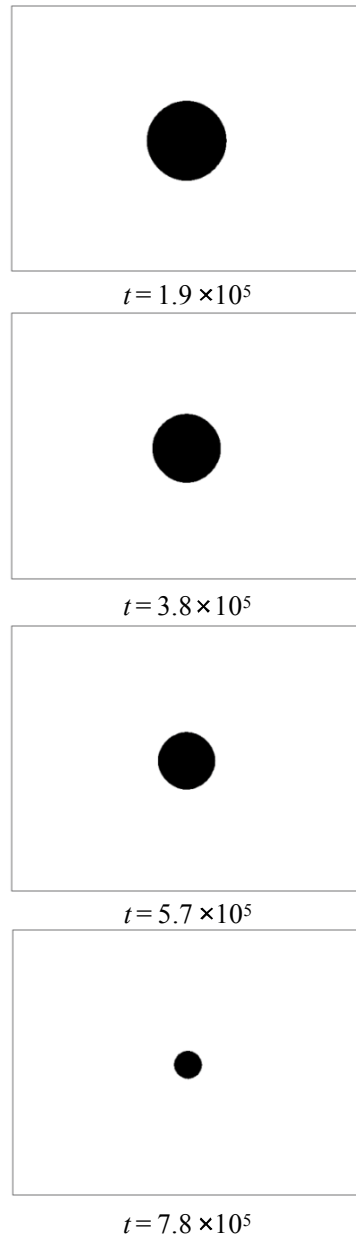


Fig. 2-11 Evaporation process of a droplet in ambient vapor for  $\varepsilon_{ev}=1.0 \times 10^{-6}$ .

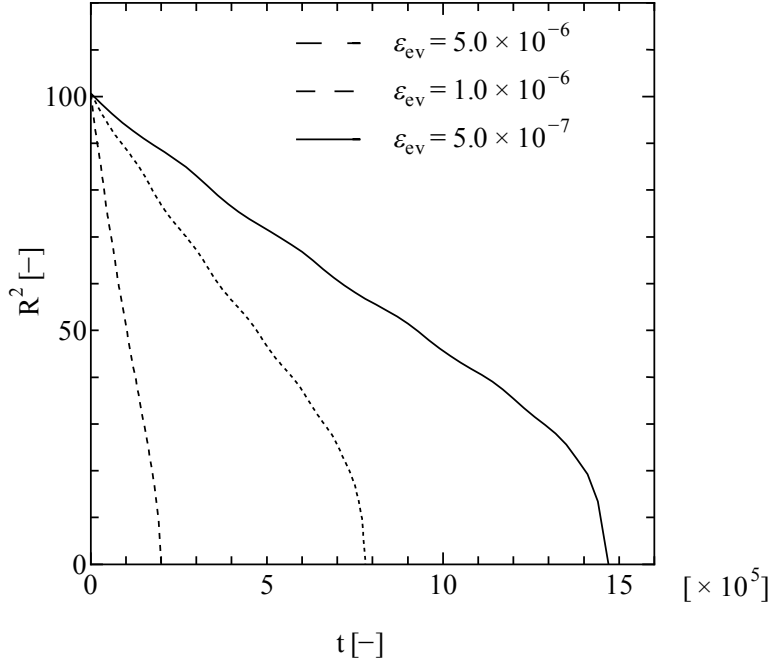


Fig. 2-12 Time variation of the square of the droplet radius for an evaporating droplet in ambient vapor. Evaporation rate coefficients are set to  $5.0 \times 10^{-6}$ ,  $1.0 \times 10^{-6}$  and  $5.0 \times 10^{-7}$

## 2.6 Solid particles transport model

In this section, a solid particles transport model is proposed to describe colloid particles motion dispersed in a liquid droplet. The transport of particles inside the droplet is evaluated by solving a Newton equation for each colloid particle. The equation of  $m$ -th colloid particle motion during the evaporation of the liquid droplet is expressed as follows:

$$m_p \frac{d\vec{u}_{p,m}}{dt} = \vec{F}_p + \vec{F}_l + \vec{F}_f - \vec{F}_g + \vec{F}_b - \vec{F}_{vis} \quad (2-66)$$

where  $\vec{u}_{p,m}$  is the velocity of the  $m$ -th particle at the moment,  $m_p$  is the mass of the colloid particles.  $\vec{F}_p$  is an interaction force between two colloid particles, which is given as  $\vec{F}_p = \sum_{m \neq n}^{N_p} \nabla U(r_{mn})$ . Here  $U(r_{mn})$  is the potential energy of the interaction of each  $m$ -th particle with any other  $n$ -th particle in the system ( $N_p$  is the total number of colloid particles within the droplet). The function form of  $U(r_{mn})$  is chosen as the part of the DLVO potential corresponding to the London-van der Waals potential energy [94] and is given as:

$$U(r_{mn}) = -\frac{A}{6} \left( \frac{2r_p^2}{(r_{mn} - 2r_p)^2 + 4r_p(r_{mn} - 2r_p)} + \frac{2r_p^2}{(r_{mn} - 2r_p)^2 + 4r_p(r_{mn} - 2r_p) + 4r_p^2} \right) - \frac{A}{6} \left( \ln \frac{(r_{mn} - 2r_p)^2 + 4r_p(r_{mn} - 2r_p)}{(r_{mn} - 2r_p)^2 + 4r_p(r_{mn} - 2r_p) + 4r_p^2} \right) \quad (2-67)$$

where  $A$  is the Hamaker constant of particles interacting in liquid,  $r_p$  is the particle radius, and  $r_{mn}$  is the distance between the  $m$ -th particle center and  $n$ -th particle center (Fig. 2-13a). The Hamaker constant  $A$  is given by

$$A = \left( \sqrt{A_{11}} - \sqrt{A_{22}} \right)^2 \quad (2-68)$$

where  $A_{11}$  and  $A_{22}$  are the Hamaker constant of the particles and medium, respectively.

The term  $\vec{F}_l$  in the Eq. (2-66) is the interaction force of the  $m$ -th particle in the liquid-vapor interface. In the present study, the interaction force  $\vec{F}_l$  is given as  $\vec{F}_l = 2\pi r_p \gamma (1 - c) \cdot \vec{n}$  in the liquid-vapor interface region (Fig. 2-13b). Here  $c = (\rho - \rho_G)/(\rho_L - \rho_G)$ ,  $\vec{n}$  is a vector normal to the liquid-gas interface, and  $\gamma$  is the free energy of the particle-solution interaction per unit area of the particle surface [95].

The term of  $\vec{F}_f$  in Eq. (2-66) is the interaction force between the  $m$ -th particles and fluid flows. The equation is given as:

$$\vec{F}_f = m_p \frac{3\rho_f c_d}{8\rho_p r_p} (\vec{u}_f - \vec{u}_{p,m}) |\vec{u}_f - \vec{u}_{p,m}| \quad (2-69)$$

where  $\rho_p$  and  $\rho_f$  is the  $m$ -th particles density and liquid density, respectively,  $\vec{u}_{p,m}$  is the  $m$ -th particles velocity,  $\vec{u}_f$  is fluid velocity,  $c_d$  is a drag coefficient and is given as  $c_d = 48/\text{Re}_p$ .

$\text{Re}_p$  is the particle Reynolds number expressed as  $\text{Re}_p = \frac{\rho_f r_p |\vec{u}_f - \vec{u}_{p,m}|}{\mu_f}$ , where  $\mu_f$  is the effective viscosity of fluid.

The term of  $\vec{F}_g$  and  $\vec{F}_b$  in Eq. (2-66) are the particle gravity and buoyancy force in the system, respectively. The function of  $\vec{F}_g$  and  $\vec{F}_b$  is given as  $\vec{F}_g = \frac{4}{3}\pi r_p^3 \rho_p g$  and  $\vec{F}_b = \frac{4}{3}\pi r_p^3 \rho_f g$ , where  $g$  is acceleration of gravity. The term of  $\vec{F}_{vis}$  in Eq. (2-66) is the Stokes



drag resistance force for a spherical particle in a viscous isotropic medium,

$$\vec{F}_{vis} = 6\pi r_p \mu_f \vec{u}_{p,m} \quad (2-70)$$

When the particle reaches to the substrate surface, the particle velocity is given as zero.

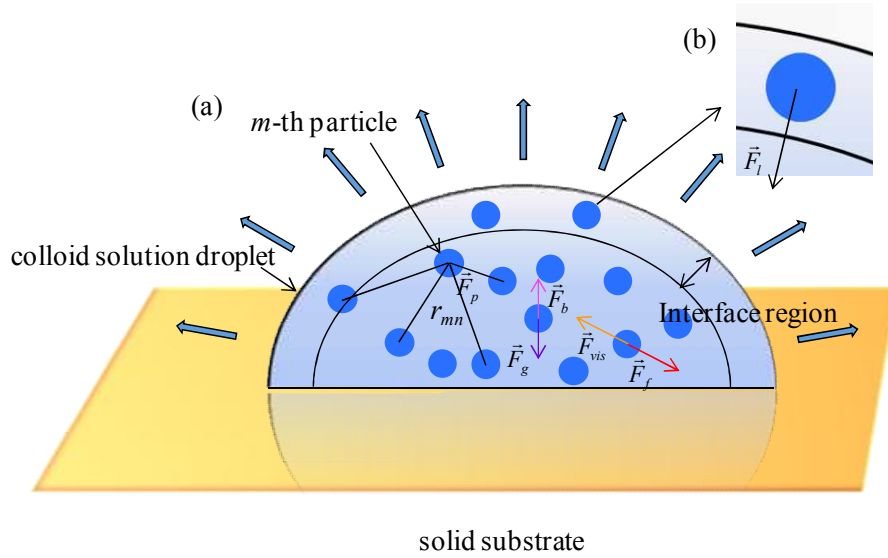


Fig. 2-13 Solid particle transport model in an evaporating droplet on substrate. Force acting on the colloid particle in liquid droplet: (a) the liquid-vapor interface region and the colloid particle; (b) the interaction force for the particle in the liquid-vapor interface region.

## 2.7 Conclusions

In this chapter, a mathematical model for the simulation of an evaporating droplet with solid colloidal particle on substrate is introduced. The mathematical model is composed of a two-phase lattice Boltzmann model, wetting model, evaporation model and solid particle transport model.

To simulate two-phase flows, the lattice Boltzmann simulation of Lee and Lin's model or Inamuro's model employs two particle distribution functions. One of the particle distribution function is used to calculate the order parameter which distinguishes the two-phase; another particle distribution function is used to calculate the momentum of the

two-phase flows.

To describe the wettability of substrates, a wetting model is introduced. In the present study, two wetting models are utilized: an adhesive force model and a partial wetting boundary condition model. The spread of a droplet on the substrate are simulated for the LB models of Lee and Lin's model and Inamuro's model by using an adhesive force model and a partial wetting boundary condition model, respectively. The wettability of substrates can be evaluated sufficiently by using these two wetting models.

An evaporation model is proposed to describe the evaporation of liquid phase on the droplet surface. The evaporation term is incorporated into LB model, which indicates the rate of mass loss in the interface region between liquid and vapor phase. The validity of the present evaporation model is confirmed by simulating the evaporation of a single droplet in ambient vapor. The result shows a linear decrease in the square of the droplet radius with time, which agrees well with the  $d^2$ -law for an evaporating droplet.

A solid particles transport model is proposed and is incorporated into the lattice Boltzmann simulation to describe the solid colloidal particles motion during droplet evaporation. The solid particle motion is evaluated by solving a Newton equation for each solid particle inside the droplet on substrate. This equation accounts for the solid particles transport due to the surrounding fluid flows, viscosity force, gravity and buoyancy force, the interaction force between the solid particle and the liquid-vapor interface and the interaction force due to the potential energy of each solid particle with any other solid particle.

## **Chapter 3 The Effect of the Computational Parameters on the Reduction of Spurious Velocities in LB Simulation of Two-phase Flows**

### **3.1 Introduction**

In two-phase lattice Boltzmann simulations, an intermolecular force term between liquid and gas phases is required to distinguish two phase and to track interfacial movement. However, it is well known that the intermolecular force cause nonphysical flows in the interfacial region to satisfy the balance of the interaction surface stresses, which are called spurious velocities or currents. In the past researches, much attention has been paid to the reduction or elimination of the spurious velocities by modifying discretization schemes or choosing suitable physical properties. Order parameter is one of the computational parameters used in a two-phase lattice Boltzmann simulation, which distinguish two phase. However, when an order parameter is employed, its range is arbitrarily chosen because the order parameter is not related to the physical properties throughout the characteristic scales of length, time, and mass. However, it is unclear how the range of the order parameter affects the spurious velocities.

In this chapter, a two-phase lattice Boltzmann simulation is performed to investigate the effect of computational parameters on the spurious velocities in a droplet in ambient vapor. In the simulation, the dimensionless surface tension parameter is given while preserving the actual physical properties by adjusting the characteristic scale. The effect of order parameter, dimensionless surface tension parameter, and density ratio of the two-phase fluid on the magnitude of spurious velocities is examined. In addition, the time for reaching steady state is also investigated by changing the range of the order parameter.

## 3.2 Numerical simulation

### 3.2.1 Computation domain

The physical problem and the computational domain are shown in Fig. 3-1. The computational domain is a two-dimensional Cartesian coordinate system divided into  $60 (L_x) \times 60 (L_y)$  lattices in the  $x$  and  $y$  directions. A spherical liquid droplet with radius  $R$  is placed in the center position of the computational domain.

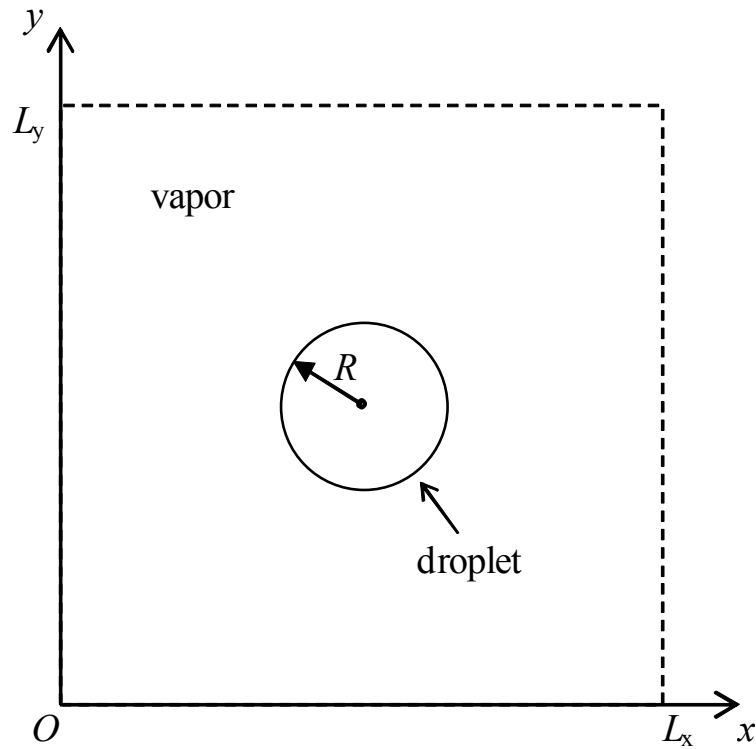


Fig. 3-1 Physical problem and computational domain.

### 3.2.2 Two-phase lattice Boltzmann model

A two-phase lattice Boltzmann model proposed by Inamuro *et al.* [43] is employed to simulate a single spherical liquid droplet in ambient vapor at nonequilibrium to equilibrium steady state. As introduced in Chapter 2, this two-phase lattice Boltzmann model employs two particle distribution functions; one is utilized to distinguish the two phase and the other is used to calculate the momentum of two phase flows. The details of the mathematical models

are presented in Chapter 2. A cyclic boundary condition is forced at the boundary of the computational domain.

### 3.2.3 Computation condition

A liquid droplet radius  $R^* = 1.0 \times 10^{-3}$  m is chosen. The densities of the two phases are set as  $\rho_L^* = 1000 \text{ kg m}^{-3}$  and  $\rho_G^* = 1.29 \text{ kg m}^{-3}$  (density ratio about 775.2), meanwhile their viscosities are  $\mu_L^* = 1.0 \times 10^{-3} \text{ Pa s}$  and  $\mu_G^* = 1.8 \times 10^{-5} \text{ Pa s}$ , respectively. The surface tension between liquid and vapor is  $\sigma_{LG}^* = 7.2 \times 10^{-2} \text{ N m}^{-1}$ . To relate the physical properties to the computational parameters, a length scale  $L_0$ , a time scale  $T_0$ , and a mass scale  $M_0$  are chosen, leading to the dimensionless computational parameters of the liquid density  $\rho_L$ , gas density  $\rho_G$ , liquid viscosity  $\mu_L$ , gas viscosity  $\mu_G$ , and surface tension  $\sigma_{LG}$ . The dimensionless radius  $R$  and interface thickness  $D$  of the droplet are set to 10 and 3, respectively. Order parameters for the liquid phase  $\phi_L$  and gas phase  $\phi_G$  are varied. To decrease the shrinking of the droplet as it reaches a steady state, the maximum and minimum values of the order parameters are given.

## 3.3 Results and discussion

### 3.3.1 Effect of surface tension

A single spherical liquid droplet in ambient vapor is simulated from nonequilibrium to equilibrium steady state condition. The droplet is considered to reach equilibrium steady state when the absolute time derivative of the droplet radius  $|dR/dt|$  is smaller than the tolerance  $\delta = 0.001|dR/dt|_{\max}$ . Fig. 3-2 shows the time variation of the droplet radius. The radius decreases and then reaches a constant value with increasing time steps, indicating that the droplet reaches a steady state at  $t = 1.1 \times 10^5$  steps.

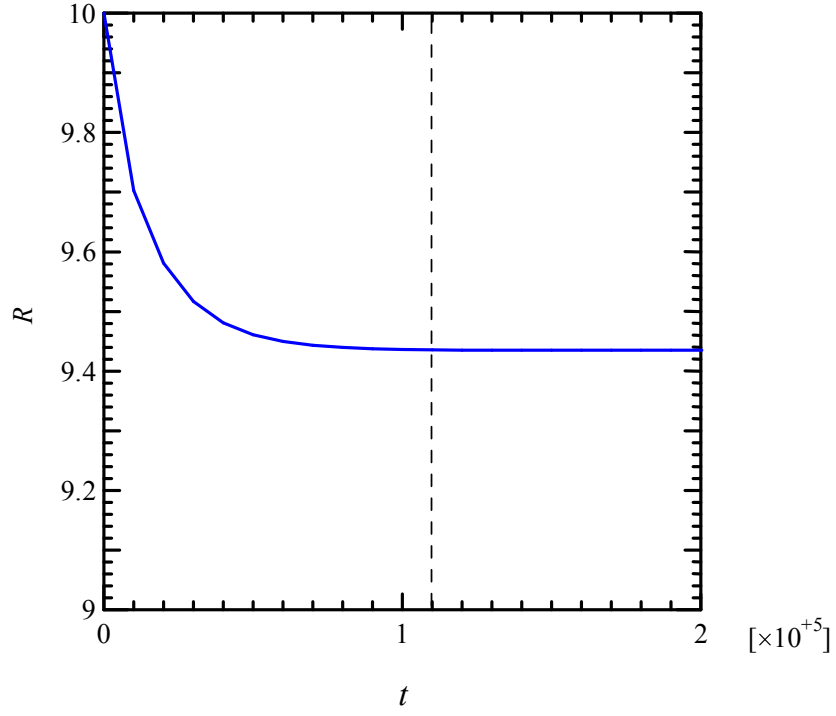


Fig. 3-2 Time variation of the radius for a single liquid droplet in ambient vapor.

( $\rho_L = 1000$ ,  $\rho_G = 1.29$ ,  $\sigma_{LG} = 5.0 \times 10^{-3}$ ,  $\mu_L = 2.635 \times 10^{-2}$ ,  $\phi_L = 4.0 \times 10^{-1}$ ,  $\phi_G = 1.0 \times 10^{-1}$ ).

Fig. 3-3 shows the density distribution and velocity fields at steady state for  $\sigma_{LG} = 5.0 \times 10^{-3}$  and  $5.0 \times 10^{-11}$ . In Fig. 3-3(a), the spurious velocities are observed near the interface and disappear gradually away from the interface. In contrast, the spurious velocities are negligibly small for small dimensionless surface tension parameter  $\sigma_{LG}$  of  $5.0 \times 10^{-11}$  as shown in Fig. 3-3(b).

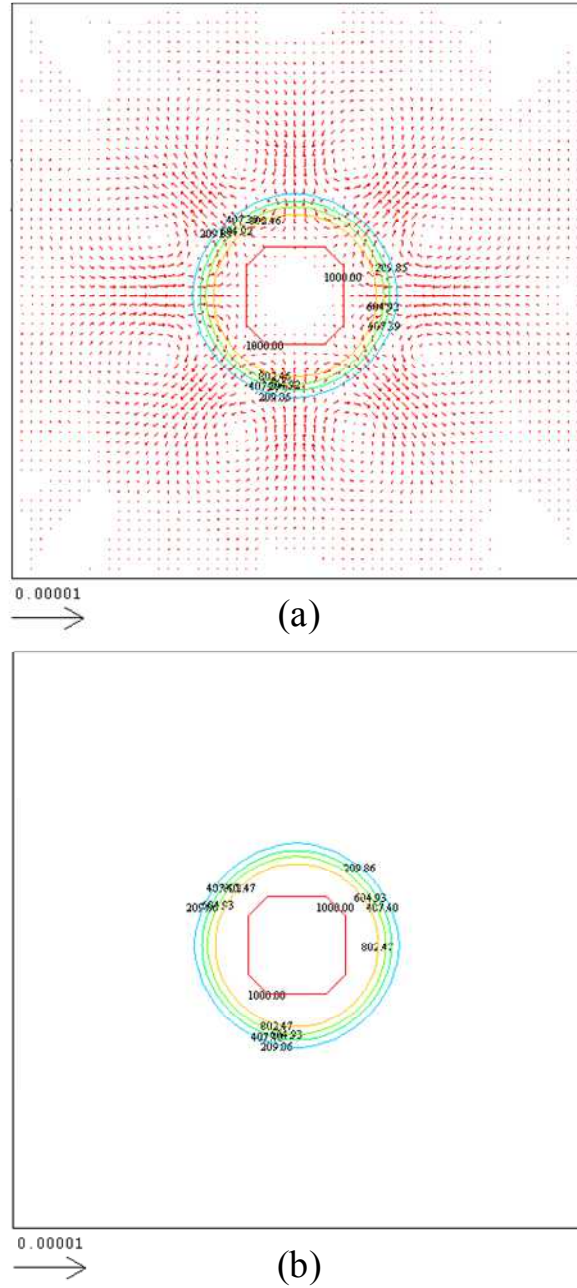


Fig. 3-3 Distribution of velocities in a liquid droplet at steady state.

(a)  $\rho_L = 1000, \rho_G = 1.29, \sigma_{LG} = 5.0 \times 10^{-3}, \mu_L = 2.635 \times 10^{-2}, \phi_L = 4.0 \times 10^{-1}, \phi_G = 1.0 \times 10^{-1}$ .

(b)  $\rho_L = 1000, \rho_G = 1.29, \sigma_{LG} = 5.0 \times 10^{-11}, \mu_L = 2.635 \times 10^{-6}, \phi_L = 4.0 \times 10^{-7}, \phi_G = 1.0 \times 10^{-7}$ .

Fig. 3-4 shows the variation of the maximum spurious velocities  $|u^s|_{max}$  as a function of the dimensionless surface tension parameter  $\sigma_{LG}$  at steady state. When the surface tension and viscosity are constant at  $\sigma_{LG}^* = 7.2 \times 10^{-2} \text{ N m}^{-1}$ ,  $\mu_L^* = 1.0 \times 10^{-3} \text{ Pa s}$ , and  $\mu_G^* = 1.8 \times 10^{-5} \text{ Pa s}$ , the dimensionless  $\sigma_{LG}$  varies from  $5.0 \times 10^{-3}$  to  $5.0 \times 10^{-11}$  by adjusting the

dimensionless liquid phase viscosity  $\mu_L$  from  $2.635 \times 10^{-2}$  to  $2.635 \times 10^{-6}$  with changing time scale  $T_0$  (solid circles). A linear decrease in  $|u^s|_{max}$  is obtained from  $1.16 \times 10^{-6}$  to  $1.21 \times 10^{-14}$  as the dimensionless surface tension parameter decreases, which corresponds to a decrease in  $|u^s|_{max}$  from  $4.402 \times 10^{-4}$  m/s to  $4.592 \times 10^{-8}$  m/s. In an evaporating water droplet on a substrate, the vertical average velocity inside the droplet is around  $10^{-8}$  m/s to  $10^{-6}$  m/s [25]. Therefore, the reduction of the spurious velocities is sufficient by decreasing the dimensionless surface tension parameter. In contrast, when the dimensionless liquid phase viscosity is constant,  $\mu_L = 2.635 \times 10^{-2}$ , and the surface tension  $\sigma_{LG}^*$  varies from  $7.2 \times 10^{-2}$  N m<sup>-1</sup> to  $7.2 \times 10^{-6}$  N m<sup>-1</sup> (open triangles),  $|u^s|_{max}$  decreases from  $1.17 \times 10^{-6}$  to  $1.17 \times 10^{-10}$  linearly, which corresponds to a decrease in  $|u^s|_{max}$  from  $4.42 \times 10^{-4}$  m/s to  $4.45 \times 10^{-8}$  m/s. The decrease in  $|u^s|_{max}$  is almost same as obtained for a constant surface tension  $\sigma_{LG}^*$  of  $7.2 \times 10^{-2}$  N m<sup>-1</sup>.

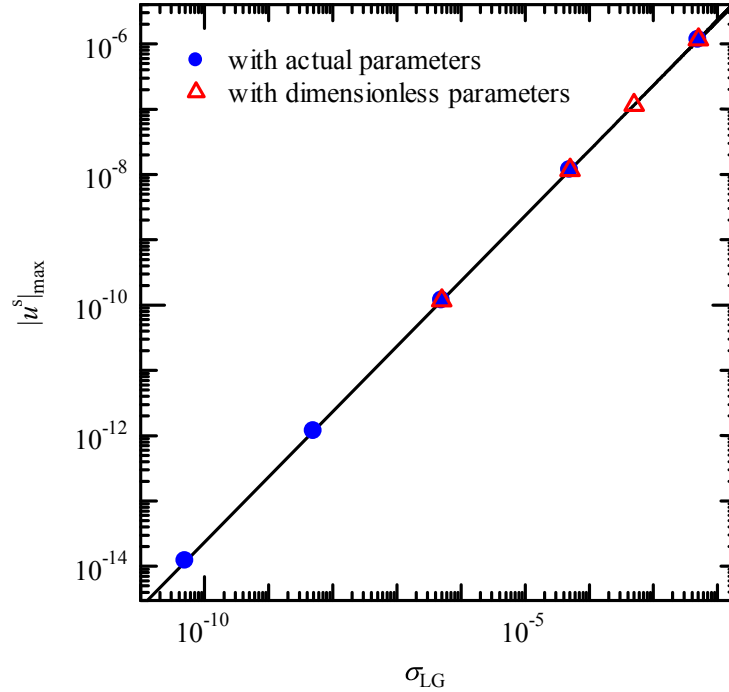


Fig. 3-4 Variation of  $|u^s|_{max}$  as a function of  $\sigma_{LG}$ .

Solid circles:  $\rho_L = 1000$ ,  $\rho_G = 1.29$ ,  $\sigma_{LG}^* = 7.2 \times 10^{-2}$  N m<sup>-1</sup>.

Open triangle:  $\rho_L = 1000$ ,  $\rho_G = 1.29$ ,  $\mu_L = 2.635 \times 10^{-2}$ ,  $\mu_G = 4.743 \times 10^{-4}$ .

Fig. 3-5 shows the variation of  $|u^s|_{max}$  as a function of the dimensionless liquid phase



viscosity  $\mu_L$  at steady state. The dimensionless liquid viscosity varies from  $2.635 \times 10^{-2}$  to  $2.635 \times 10^{-5}$  whereas the dimensionless surface tension remains constant at  $\sigma_{LG} = 5.0 \times 10^{-3}$ . The maximum spurious velocities are almost constant for the present liquid phase viscosity.

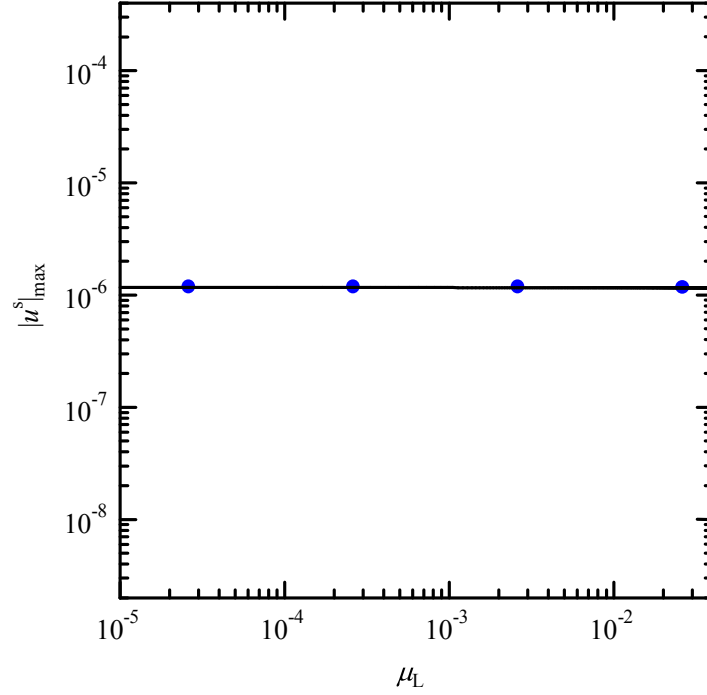


Fig. 3-5 Variation of  $|u^s|_{max}$  as a function of  $\mu_L$ . ( $\rho_L = 1000$ ,  $\rho_G = 1.29$ ,  $\sigma_{LG} = 5.0 \times 10^{-3}$ ).

From the results shown in Figs. 3-4 and 3-5, the dimensionless surface tension parameter greatly affects the spurious velocities, whereas the effect of the viscosity is negligibly small. Lee and Fischer [58] reported that spurious velocities are caused by the slight imbalance between the pressure gradient and interfacial stress due to the truncation error in discretization. As for the pressure, Fig. 3-6 shows the pressure profile at  $y = y_c$  ( $y_c = L_y/2$ ) for dimensionless surface tension  $\sigma_{LG}$  of  $5.0 \times 10^{-7}$  and  $5.0 \times 10^{-11}$ . The pressure difference between the droplet inside and the bulk vapor phase  $\Delta p^*$  is 70.4 Pa for both dimensionless surface tension parameters, which is almost consistent with the value of  $\Delta p^* = \sigma_{LG}^*/R^* = 72$  Pa from Laplace's law. In addition, although slight overshoots are observed, the pressure profile provides the correct evaluation of the pressure gradient, which may not contribute to the occurrence of spurious velocities.

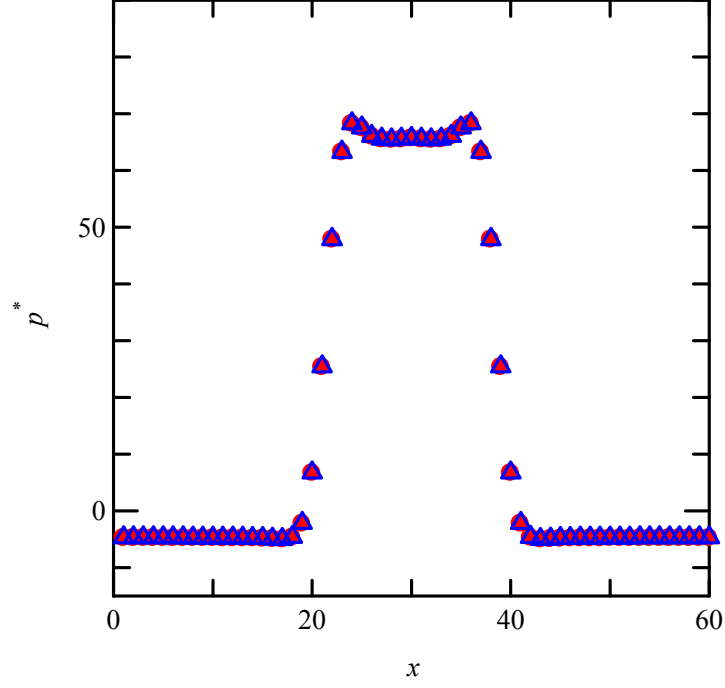


Fig. 3-6 Variation of pressure at  $y = y_c$  as a function of position  $x$ .

Solid circles:  $\rho_L = 1000$ ,  $\rho_G = 1.29$ ,  $\sigma_{LG} = 5.0 \times 10^{-7}$ ,  $\sigma_{LG}^* = 7.2 \times 10^{-2} \text{ N m}^{-1}$ .

Open triangle:  $\rho_L = 1000$ ,  $\rho_G = 1.29$ ,  $\sigma_{LG} = 5.0 \times 10^{-9}$ ,  $\sigma_{LG}^* = 7.2 \times 10^{-2} \text{ N m}^{-1}$ .

### 3.3.2 Effect of the order parameter

In order to examine the effect of the order parameters on the spurious velocities, the variation of  $|u^s|_{max}$  as a function of the order parameter difference between the liquid and vapor phase at steady state is shown in Fig. 3-7. The liquid-phase order parameters are set to  $4.0 \times 10^{-3}$ ,  $4.0 \times 10^{-4}$ , and  $4.0 \times 10^{-5}$ , whereas the vapor-phase order parameters are set to  $1.0 \times 10^{-3}$ ,  $1.0 \times 10^{-4}$ , and  $1.0 \times 10^{-5}$ , respectively. The order parameter shows little influence on the maximum spurious velocities.

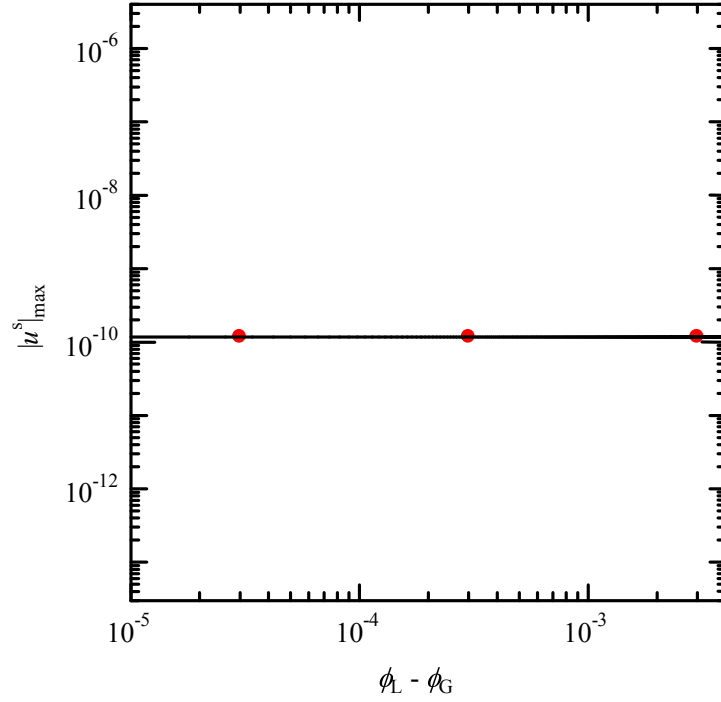


Fig. 3-7 Magnitude of  $|u^s|_{max}$  as a function of the liquid-droplet order parameters.

$$(\rho_L = 1000, \rho_G = 1.29, \sigma_{LG} = 5.0 \times 10^{-7}, \mu_L = 2.635 \times 10^{-4}).$$

Fig. 3-8 shows the time steps required to reach equilibrium steady state for the same conditions as shown in Fig. 3-7. The time steps for an equilibrium state decrease with the order parameter difference. This indicates that the computational time can be saved greatly by using a small order parameter to reach equilibrium even though physical properties such as density, viscosity, and surface tension remain constant. However, smaller order parameters lead to larger  $\beta$  and  $\kappa$  in Eqs. (10) and (11) for a fixed surface tension parameter and interface thickness. This implies that the fluids are less compressible, which results in shorter time steps required to reach steady state [58].

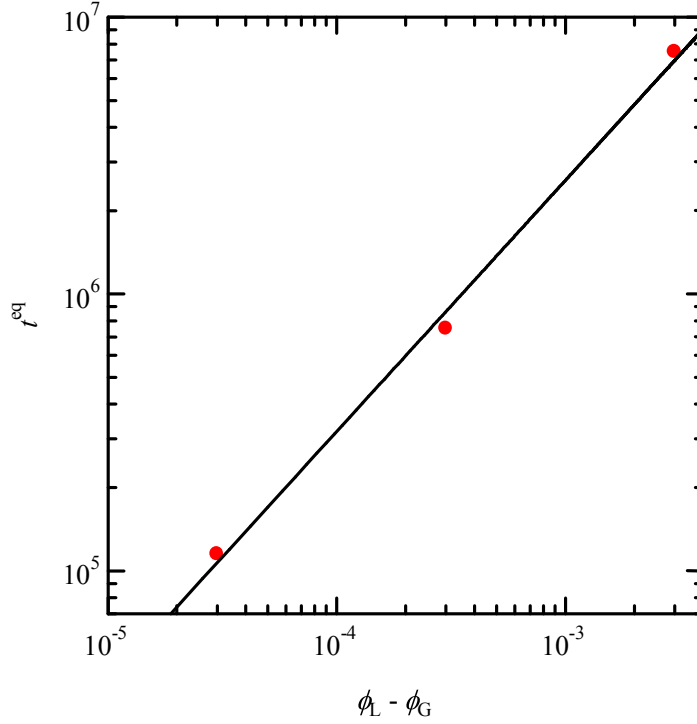


Fig. 3-8 Magnitude of  $t^{eq}$  as a function of the liquid-droplet order parameters.

$$(\rho_L = 1000, \rho_G = 1.29, \sigma_{LG} = 5.0 \times 10^{-7}, \mu_L = 2.635 \times 10^{-4})$$

### 3.3.3 Effect of density ratio

Fig. 3-9 shows the variations of  $|u^s|_{max}$  as a function of the density ratio  $\rho_L/\rho_G$  at steady state. The dimensionless surface tension parameter is set to  $5.0 \times 10^{-7}$  for the three density ratios of 10, 100, and 775.2. Other dimensionless computational parameters and characteristic scales are the same with the values for  $\sigma_{LG} = 5.0 \times 10^{-7}$  and  $\mu_L = 2.635 \times 10^{-4}$  as presented above.  $|u^s|_{max}$  shows a minor increase with density ratio. This may be caused by the increase in the imbalance between the pressure gradient and interfacial stress due to the truncation error of the discretization. However, the variation of spurious velocities is small for different density ratios, compared with the past results [64]. This may be because the pressure calculation is sufficiently accurate in the present simulation.

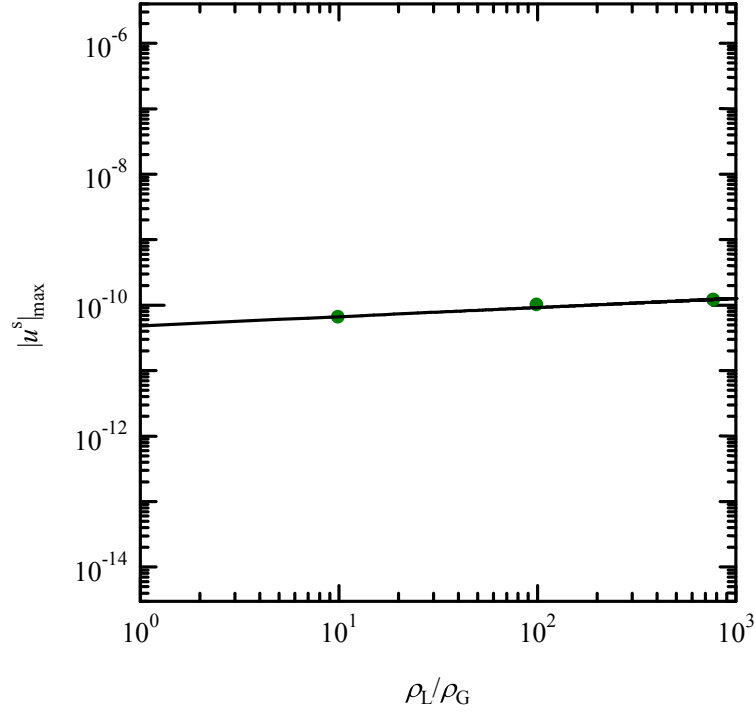


Fig. 3-9 Variation of  $|u^s|_{\max}$  as a function of  $\rho_L/\rho_G$ .

$$(\sigma_{LG} = 5.0 \times 10^{-7}, \mu_L = 2.635 \times 10^{-4})$$

### 3.3 Conclusions

A two-phase lattice Boltzmann simulation was performed to investigate the effect of computational parameters on the reduction of spurious velocities that appear in a droplet in ambient vapor. The major findings are summarized as follows.

Maximum spurious velocities can be decreased up to approximately  $10^{-14}$  by giving a small dimensionless surface tension. This spurious velocity corresponds to  $10^{-8}$  m/s, and is sufficiently small to neglect the internal fluid flow caused by the spurious velocities in an evaporating droplet on a substrate. The decrease in the order parameter has little influence on the reduction of spurious velocities. However, the smaller the order parameter is given, the shorter the time to reach steady state is obtained. This may be because the smaller order parameter difference leads to less compressibility of the fluids for a given surface tension and interface thickness. The maximum spurious velocity increases slightly with the density ratio. Only the dimensionless surface tension parameter greatly influences the reduction of the

spurious velocities in two-phase fluids and the liquid-vapor interface.

## **Chapter 4 A Lattice Boltzmann Simulation of Contact Line Motion and Internal Fluid Flows in an Evaporating Droplet on Homogenous Substrates**

### **4.1 Introduction**

When a sessile droplet evaporates on hydrophobic substrates, the contact line recedes as the evaporation progresses, which is called as de-pinning. In contrast, when a sessile droplet evaporates on hydrophilic substrates, two types of contact line motion are observed during the evaporation: the wetting diameter remains constant whereas the contact angle decreases (pinning), and the wetting diameter decreases and the contact angle remains constant (de-pinning). The contact line motion affects the thin film shape after the evaporation of a droplet with solid constituents or solutes. For example, when the contact line of an evaporating droplet is pinned during the evaporation, ring-like deposit of solutes is obtained due to the outward flows toward the contact line. However, the effect of the droplet shape change on the contact line motion and internal fluid flows during evaporation has not been investigated.

In this chapter, a lattice Boltzmann simulation of two-phase flow proposed by Inamuro *et al.* [43] is carried out to investigate the evaporation of a single droplet on homogeneous substrates. An evaporation model is proposed for simulating droplet evaporation. A partial wetting boundary condition is imposed to control the wettability of the substrate. The contact line motion of an evaporating droplet on homogenous substrates is discussed. In addition, fluid flows in the droplet during the evaporation of the droplet on hydrophilic substrates are discussed.

### **4.2 Numerical Simulation**

#### **4.2.1 Computational domain**

The physical problem and computational domain of an evaporating droplet on a homogeneous substrate are shown in Fig. 4-1. The computational domain is a two-dimensional Cartesian coordinate system and is divided into  $80 (L_x) \times 30 (L_y)$  lattices. A single droplet with an initial contact angle of  $\theta_{c,0} = 90^\circ$  is placed on a substrate with homogenous wettability (hydrophilic:  $\theta_{c,g} < 90^\circ$ , hydrophobic:  $\theta_{c,g} > 90^\circ$ ). The initial shape of the droplet is hemisphere. The wetting diameter and the height of the droplet are denoted by  $d_w$  and  $h$ .

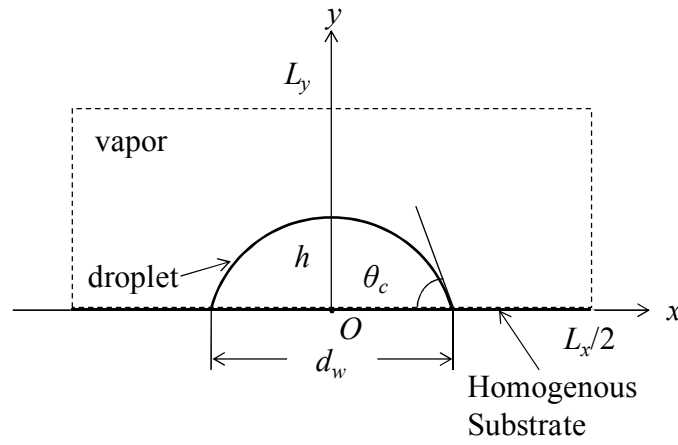


Fig. 4-1 Physical problem and computational domain of a droplet on homogenous substrates.

#### 4.2.2 Two-phase lattice Boltzmann model

A two-phase lattice Boltzmann model proposed by Inamuro *et al.* [43] is employed to simulate the evaporation of a droplet on homogenous substrates. As introduced in Chapter 2, this two-phase lattice Boltzmann model employs two particle distribution functions; one is utilized to distinguish the two phase and the other is used to calculate the momentum of two phase flows. An evaporation model proposed in Chapter 2 is applied to the evaluation of mass loss of liquid phase. A partial wetting boundary condition is incorporated into the lattice Boltzmann model to describe the wettability of the substrates. The details of the mathematical models are presented in Chapter 2.

On the boundaries at  $x = 0$ ,  $x = L_x$ , and  $y = L_y$ , non-slip boundary conditions are given,



and the normal derivatives of the order parameter, and the predicted and corrected velocities are set to zero. On the boundary at  $y = 0$ , the partial wetting boundary condition is imposed to control the wettability of the substrates. The predicted and corrected velocities are set to zero.

### 4.3.2 Computation conditions

The simulation parameters and physical properties are shown in Table 4-1. The maximum and minimum values of the order parameter are  $\phi_{min}=9.999\times10^{-6}$  and  $\phi_{max}=4.5\times10^{-5}$ , respectively. In order to relate the physical properties to the simulation parameters, the length scale, time scale, and mass scale are given as  $L_0=1.0\times10^{-4}$  m,  $T_0=2.635\times10^{-9}$  s, and  $M_0=1.0\times10^{-12}$  kg, respectively. An evaporation rate coefficient  $\varepsilon_{ev}$  is varied from  $5.0\times10^{-9}$  to  $1.0\times10^{-7}$ . For example, an evaporation rate coefficient of  $1.0\times10^{-8}$  results in an evaporation termination time (the period of time from the beginning of evaporation to the disappearance of the droplet) of 0.45s for droplet evaporation on a hydrophilic substrate; this time is shorter than experiments, about 700s [24]. This indicates that the time scale of spreading in the simulation is relatively large, accounting for 10.6% of the evaporation termination time because of the large evaporation rate coefficient. In the present simulation, therefore, the droplet shape reaches equilibrium at first, and evaporation begins subsequently.

## 4.3 Results and Discussion

### 4.3.1 Evaporation of a single droplet on a hydrophobic substrate

Fig. 4-2 shows the evaporation process of a droplet on a hydrophobic substrate with a static contact angle of  $120^\circ$ . The evaporation rate coefficient is set to  $1.0\times10^{-8}$ , and the evaporation begins at  $t = 1.0\times10^7$  steps. The contact line recedes until the droplet reaches an equilibrium shape, and the droplet retains its shape until evaporation begins. After evaporation begins, the droplet size decreases with increasing time, and the droplet finally disappears from the substrate after  $t = 7.6\times10^5$  steps.

Fig. 4-3 shows the time variation of wetting diameter  $d_w$  and contact angle  $\theta_c$  for the

Table 4-1 Computational conditions

	Simulation parameters	Physical properties
Liquid density ( $\rho_L$ )	1000	1000 kg m <sup>-3</sup>
Gas density ( $\rho_G$ )	1.29	1.29 kg m <sup>-3</sup>
Order parameter for liquid phase ( $\phi_L$ )	$4.0 \times 10^{-5}$	~
Order parameter for gas phase( $\phi_G$ )	$1.0 \times 10^{-5}$	~
Liquid viscosity ( $\mu_L$ )	$2.635 \times 10^{-4}$	$1.0 \times 10^{-3}$ Pa s
Gas viscosity ( $\mu_G$ )	$4.743 \times 10^{-6}$	$1.8 \times 10^{-5}$ Pa s
Surface tension ( $\sigma_{LG}$ )	$5.0 \times 10^{-7}$	$7.2 \times 10^{-2}$ N m <sup>-1</sup>
Interface width ( $D$ )	3	~
Initial wetting diameter ( $d_{w,0}$ )	20	$2.0 \times 10^{-3}$ m
Gravity acceleration ( $g$ )	$6.80436 \times 10^{-13}$	$9.8$ m s <sup>-2</sup>

droplet on the hydrophobic substrate with a static contact angle of 120°. The evaporation begins at  $t = 1.0 \times 10^7$  steps for evaporation rate coefficients of  $5.0 \times 10^{-9}$ ,  $1.0 \times 10^{-8}$  and  $1.0 \times 10^{-7}$ . Before the evaporation begins,  $d_w$  decreases with time and then remains constant until  $t = 1.0 \times 10^7$  steps; the contact angle is almost equal to the given static contact angle of 120°. After evaporation begins, the wetting diameter decreases almost linearly up to 7 and then decreases rapidly until the droplet disappears near the end of evaporation. This rapid decrease is caused by the order parameter on hydrophobic substrates being smaller than the liquid-phase order parameter, which leads to the mass loss inside the droplet near the substrate. The changes in the wetting diameter and the contact angle show no remarkable difference for the present evaporation rate coefficients. These results agree well with those of an experiment on the water droplet evaporation on hydrophobic substrates [24]. The evaporation termination time varies with the evaporation rate coefficient. This is a consequence of a large evaporation rate coefficient resulting in a large rate of mass loss.

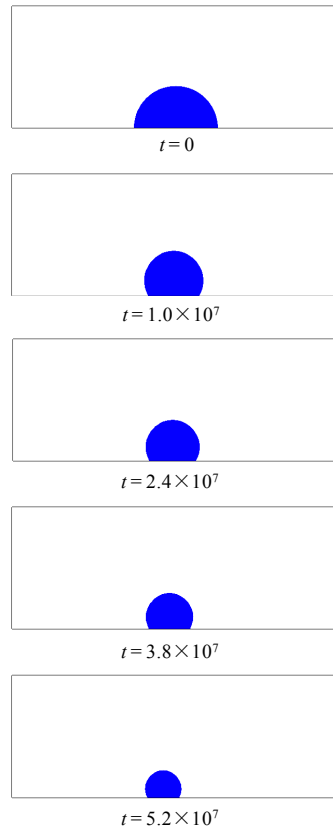


Fig. 4-2 Evaporation process of a droplet on a hydrophobic substrate for  $\theta_{c,g} = 120^\circ$ .

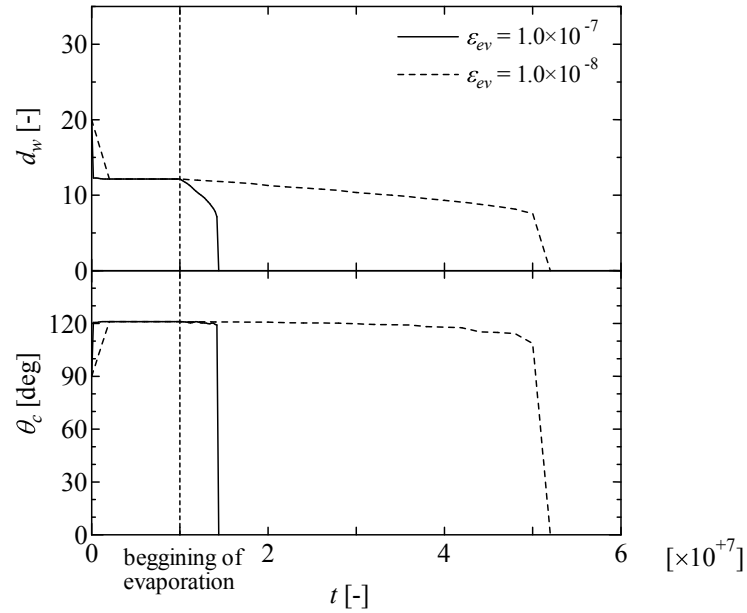


Fig. 4-3 Time variation of  $d_w$  and  $\theta_c$  of an evaporating droplet on a hydrophobic substrate ( $\theta_{c,g} = 120^\circ$ ).  $\epsilon_{ev} = 5.0 \times 10^{-9}$ ,  $1.0 \times 10^{-8}$  and  $1.0 \times 10^{-7}$ , respectively

### 4.3.2 Evaporation of a single droplet on a hydrophilic substrate

Fig. 4-4 shows the evaporation process of a droplet on a hydrophilic substrate with a static contact angle of  $60^\circ$ . Fig. 4-5 shows the time variation of wetting diameter  $d_w$  and contact angle  $\theta_c$  for the droplet. In Figs. 4-4 and 4-5,  $\varepsilon_{ev}$  is set to  $1.0 \times 10^{-8}$ , and evaporation begins at  $t = 1.0 \times 10^7$  steps after the droplet spread reaches equilibrium. The wetting diameter decreases linearly, while the contact angle remains constant and is almost consistent with the given static contact angle. The wetting diameter and contact angle decrease rapidly near the end of evaporation. These results indicate that the contact line recedes throughout the evaporation. However, Shanahan and Bourges [16] (1994) reported that there are three stages during the evaporation of a droplet on hydrophilic substrates: a constant wetting diameter stage, constant contact angle stage, and mixed stage. The reason for the difference between

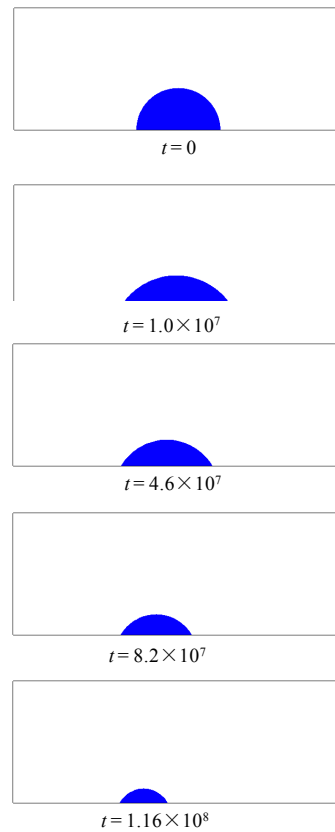


Fig. 4-4 Evaporation process of a droplet on a hydrophilic substrate for  $\theta_{c,g} = 60^\circ$  and  $\varepsilon_{ev} = 1.0 \times 10^{-8}$ .

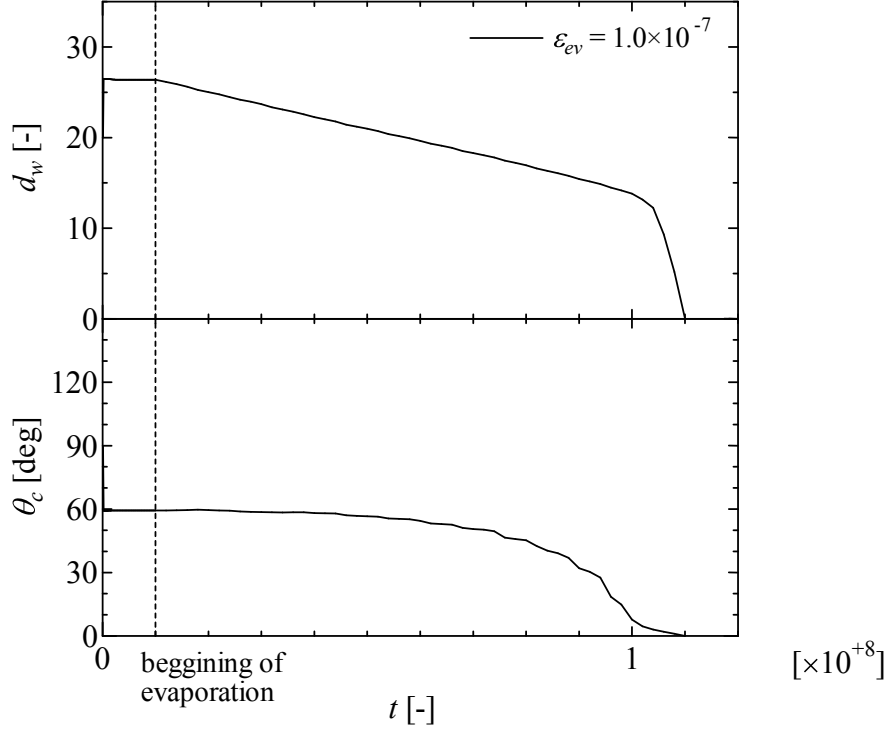


Fig. 4-5 Time variation of  $d_w$  and  $\theta_c$  for an evaporating droplet on a hydrophilic substrate for  $\theta_{c,g} = 60^\circ$  and  $\epsilon_{ev} = 1.0 \times 10^{-8}$ .

the calculation and the experiments is that the partial wetting boundary condition assumes a constant wetting potential throughout the evaporation. However, Shanahan and Sefiane [96] reported that free energy changes during the evaporation. Hence, to take into account the change in the wetting potential, the contact angle in the wetting boundary condition is dynamically changed during evaporation.

When the contact line of an evaporating droplet is pinned on a hydrophilic substrate with remaining a hemispherical shape, the overall evaporation rate  $dV/dt$  is evaluated as follows:

$$\frac{dV}{dt} = \frac{dV}{d\theta} \frac{d\theta}{dt} = \frac{2R^2(1 - \theta \cot \theta)}{\sin^2 \theta} \frac{d\theta}{dt} \quad (4-1)$$

where  $R$  is the wetting radius. The change in the contact angle from time  $t$  to  $t + \Delta t$  is given by

$$\Delta\theta_t = \frac{\Delta V_t \sin^2 \theta_t}{2R_t^2(1 - \theta_t \cot \theta_t)} \Delta t \quad (4-2)$$

where  $\Delta V_t$  is the change in the droplet volume,  $\Delta t$  is the time step,  $\theta_t$  is the contact angle at time  $t$ , and  $R_t$  is the wetting radius. Then, the contact angle at  $t+\Delta t$  is given as  $\theta_{t+\Delta t} = \theta_t - \Delta\theta_t$ .

Fig. 4-6 shows the evaporation process of a droplet on a hydrophilic substrate when the contact angle in the partial wetting boundary condition is dynamically changed. The time variation of the wetting diameter and the contact angle are shown in Fig. 4-7. The contact angle used in the modified boundary condition varies from  $60^\circ$  to  $30^\circ$  and then remains constant at  $30^\circ$  as shown in the figure (dashed line). The evaporation begins at  $t = 1.0 \times 10^7$  steps, and the evaporation rate coefficient is set to  $1.0 \times 10^{-8}$ . In the calculated result obtained by using the modified boundary condition, there are three stages of contact line motion during the evaporation. In stage I, the wetting diameter remains constant while the contact

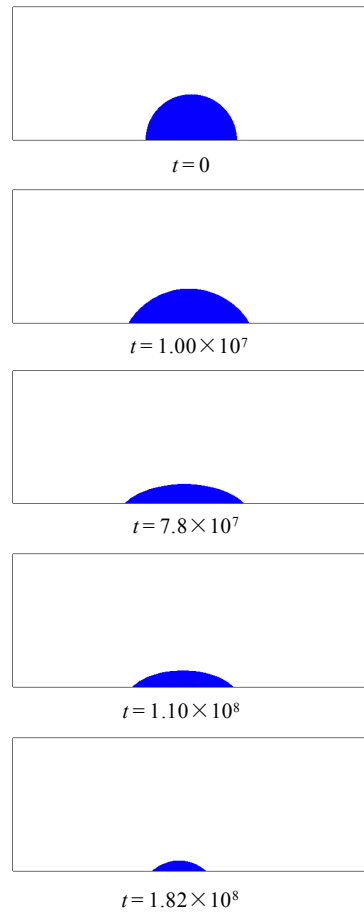


Fig. 4-6 Evaporation process of a droplet on a hydrophilic substrate for  $\varepsilon_{ev} = 1.0 \times 10^{-8}$ . The partial wetting boundary condition is given for dynamical contact angle changing from  $60^\circ$  to  $30^\circ$ .

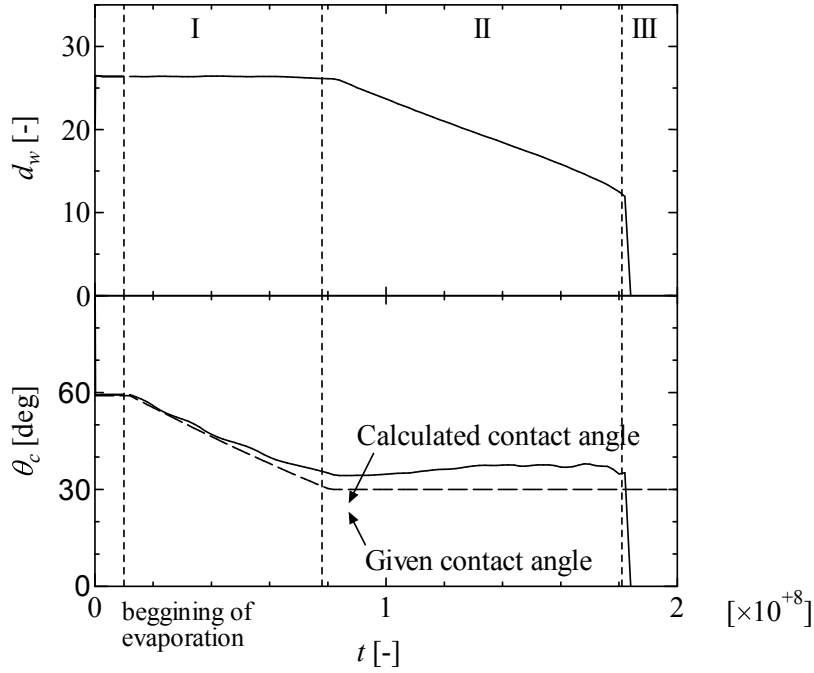


Fig. 4-7 Time variation of  $d_w$  and  $\theta_c$  for an evaporating droplet on a hydrophilic substrate for  $\varepsilon_{ev} = 1.0 \times 10^{-8}$ . The partial wetting boundary condition is given for dynamical contact angle changing from  $60^\circ$  to  $30^\circ$ .

angle decreases; this is the pinning stage. In stage II, the wetting diameter decreases and the contact angle increases slightly; this accounts for the contact line motion being in the de-pinning stage. The wetting diameter and contact angle decrease rapidly near the end of evaporation in stage III. These three stages of the contact line motion during the droplet evaporation process agree well with those observed in the experiments of Shanahan and Bourguès [16].

Fig. 4-8 shows the effect of the evaporation rate on the time variations of the wetting diameter and the contact angle for the droplet on the hydrophilic substrate. Although the evaporation rate increases with  $\varepsilon_{ev}$ , the contact line motion shows almost the same behavior under the present conditions. The evaporation termination time becomes shorter with increasing  $\varepsilon_{ev}$  because the rate of mass loss increases.

Fig. 4-9 shows the velocity distribution in an evaporating droplet for  $\varepsilon_{ev}$  of  $1.0 \times 10^{-8}$  at the beginning of evaporation, in the middle of the pinning stage, at the end of the pinning stage and in the middle of the de-pinning stage. The solid line shows the interface between

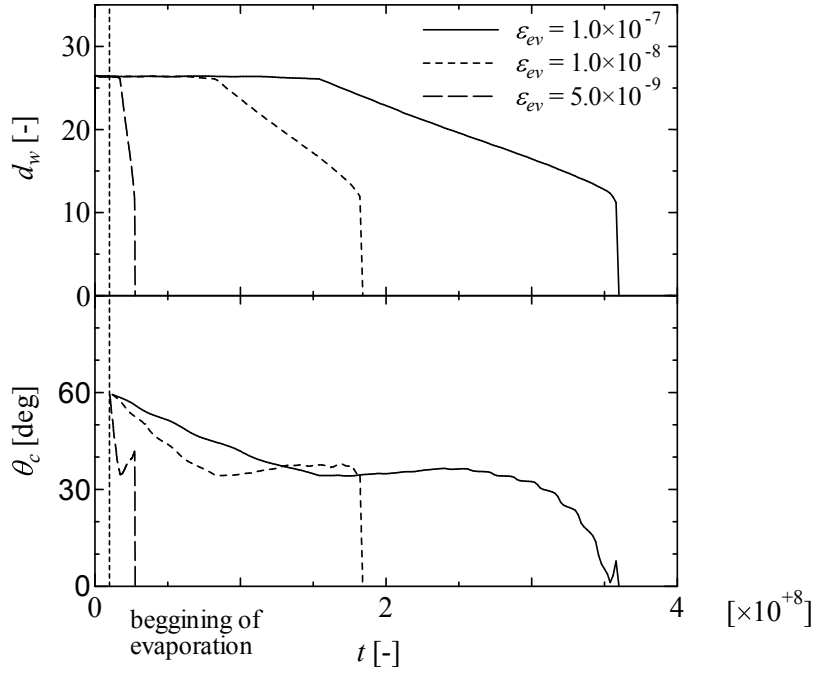


Fig. 4-8 Time variation of  $d_w$  and  $\theta_c$  for an evaporating droplet on a hydrophilic substrate for  $\varepsilon_{ev} = 5.0 \times 10^{-9}$ ,  $1.0 \times 10^{-8}$  and  $1.0 \times 10^{-7}$ . The partial wetting boundary condition has a dynamical contact angle ranging from  $60^\circ$  to  $30^\circ$ .

the liquid and ambient vapor phase. The velocity snapshots of the evaporating droplet at different times show that the internal fluid flows towards the contact line of the droplet during droplet evaporation.

Deegan *et al.* [20] found that the pinning of the contact line of an evaporating droplet causes the radial fluid flows toward the contact line to compensate for the evaporated liquid. In addition, they measured the vertically averaged fluid velocity inside an evaporating droplet and showed an increase in the fluid velocities toward the contact line. Fig. 4-10 shows the vertically averaged velocity  $v(x,t)$  for  $\varepsilon_{ev} = 1.0 \times 10^{-8}$  at the beginning, in the middle, and at the end of the contact line pinning stage.  $v(x,t)$  is calculated at position  $x$  and time  $t$  by the following equation:



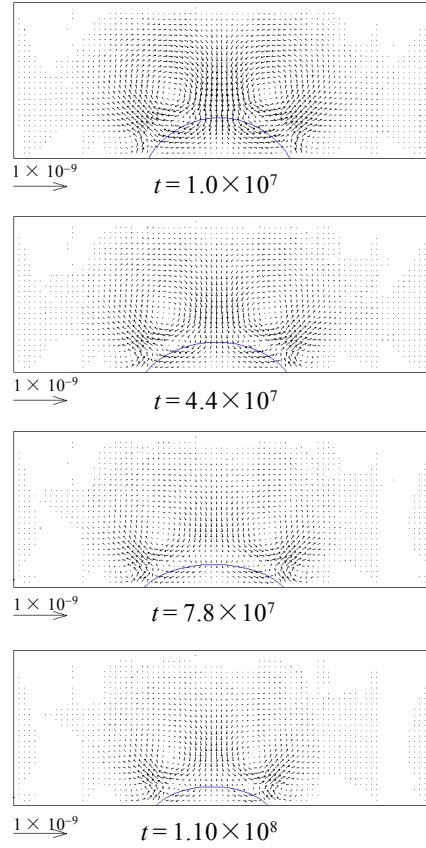


Fig. 4-9 Velocity distribution in an evaporating droplet on a hydrophilic substrate at the beginning, in the middle, and at end of the contact line pinning stage and in the middle of the contact line de-pinning stage for  $\varepsilon_{ev} = 1.0 \times 10^{-8}$ . The partial wetting boundary condition is given for dynamical contact angle changing from  $60^\circ$  to  $30^\circ$ .

$$v(x,t) = \frac{\sum_{y=0}^{h(x,t)} u_x(y,t)}{h(x,t)} \quad (4-3)$$

where  $h(x,t)$  is the vertical distance from the substrate surface to the interface of the droplet and can be obtained by using the number of lattice points at position  $x$  and time  $t$ .  $v(x,t)$  increases linearly toward the contact line and reaches the maximum value near the interface region. The fluid velocity is zero at the contact line of the droplet because the contact line is pinned.  $v(x,t)$  is not equal to zero at the beginning of the pinning stage, and then the magnitude of  $v(x,t)$  decreases as the evaporation progresses. This indicates that spurious

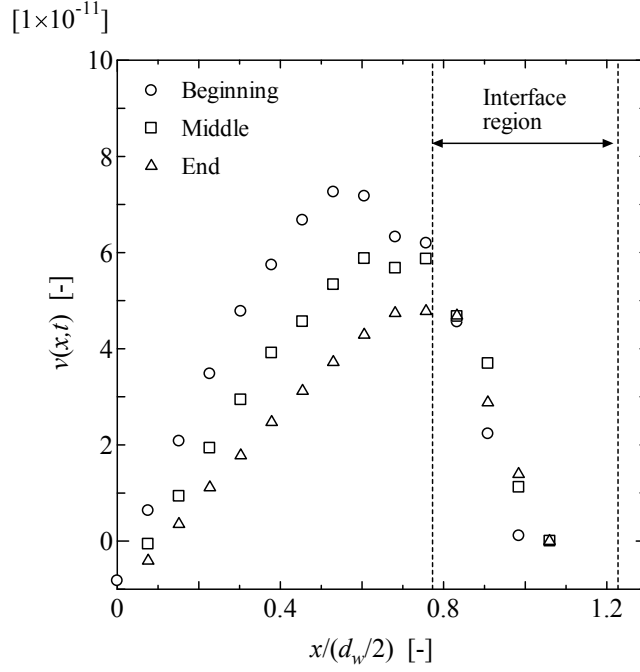


Fig. 4-10 Variation of the vertically averaged velocity in the  $x$ -direction in the droplet at the beginning in the middle, and at the end of the contact line pinning stage. The evaporation rate coefficient is set to  $1.0 \times 10^{-8}$ . The partial wetting boundary condition is given for dynamical contact angle changing from  $60^\circ$  to  $30^\circ$ .

velocities are formed in the interface region. The maximum value of  $v(x,t)$  is ranged from  $1.52$  to  $2.66 \times 10^{-6}$  m/s. In the experiment of Deegan *et al.* [20], the vertically averaged velocity in a evaporating water droplet of the diameter of 1mm is approximately ranged from  $1$  to  $6 \times 10^{-6}$  m/s. Therefore, the spurious velocity observed in the simulation is sufficiently small, however, further decrease is required by choosing smaller dimensionless surface tension parameter.

Fig. 4-11 shows the distribution of the vertically averaged fluid velocity  $v(x,t)$  in the droplet during the contact line pinning stage for  $\varepsilon_{ev}$  of  $5.0 \times 10^{-9}$ ,  $1.0 \times 10^{-8}$ , and  $1.0 \times 10^{-7}$ .  $v(x,t)$  increases linearly from the center towards the contact line for three  $\varepsilon_{ev}$  values. Although the vertically averaged velocity in  $\varepsilon_{ev} = 1.0 \times 10^{-7}$  shows a little larger value than that in the other evaporation rate coefficients, the evaporation rate has less influence on the internal fluid flows of the evaporating droplet in the present simulation. In the present simulation, the evaporation term is given only to the particle distribution function for order parameters to

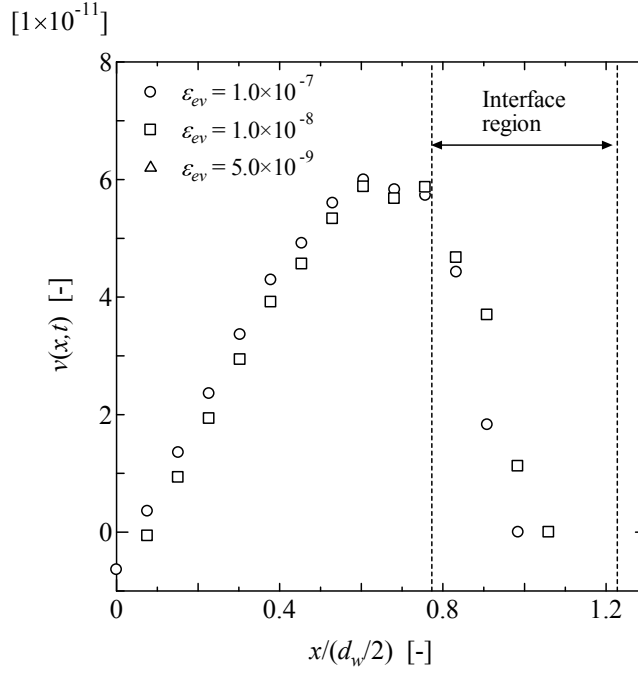


Fig. 4-11 Variation of the vertically averaged velocity in the  $x$ -direction in the droplet midway through the contact line pinning stage ( $\varepsilon_{ev} = 5.0 \times 10^{-9}$ ,  $1.0 \times 10^{-8}$ , and  $1.0 \times 10^{-7}$ ). The partial wetting boundary condition is given for dynamical contact angle ranging from  $60^\circ$  to  $30^\circ$ .

evaluate the mass loss of liquid phase. However, the movement of interface due to the evaporation may cause the momentum change in the interface, which is required to evaluate the internal fluid flows of an evaporating droplet. Therefore, some modification is required in the particle distribution function for momentum in the lattice Boltzmann equations.

Kim *et al.* [25] derived a correlation equation between the vertically averaged velocity and overall evaporation flux over the droplet surface. In this correlation, the vertically average velocity increases with increasing the evaporation flux. Fig. 4-12 shows the time variation of overall evaporation flux  $J_t$ . The overall evaporation flux  $J_t$  is calculated from the weight loss ( $m_{t-1} - m_t$ ) per unit time per unit surface area  $A_{t-1}$  of the droplet as follows [25]:

$$J(t) = \frac{m_{t-1} - m_t}{A_{t-1}} \quad (4-4)$$

This result shows the decrease in the evaporation flux with time. In the simulation, local

evaporation flux on the droplet surface is given by the following equation.

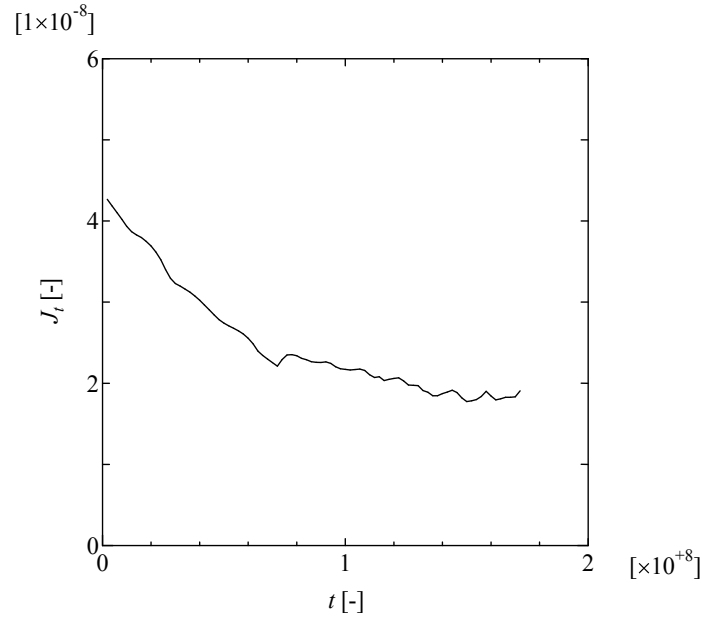


Fig.4-12 Time variation of  $J_l$  for dynamic contact angle changing from  $60^\circ$  to  $30^\circ$ .

$$J_s(x) = \varepsilon_{ev} (d_w/2 - x)^{-\chi} \quad (4-5)$$

where  $\varepsilon_{ev}$  is the evaporation rate coefficient,  $d_w$  is the wetting diameter,  $\chi = (\pi - 2\theta_c)/(2\pi - 2\theta_c)$ . This equation indicates a decrease in the local evaporation flux as the contact angle decreases during the pinning stage of the evaporation, as shown in Fig. 4-13. However, in the experiment of Kim *et al.* [25] and the theoretical prediction by Deegan *et al.* [5], both  $J(x)$  and  $v(x,t)$  increase with time as the evaporation progresses. The discrepancy between the present simulation and past researches may be caused by saturation vapor concentration  $c_v$  on the interface. As the evaporation progress, the contact angle changes small in the pinning stage so that the height of the droplet will decrease. This will be favorable for the heat transfer inside the droplet, and results in the increase in the droplet surface temperature. Then, the saturation vapor concentration increases, leading to the increase in the evaporation flux. Therefore, further modification of the simulation is required by incorporating heat transfer in an evaporating droplet.

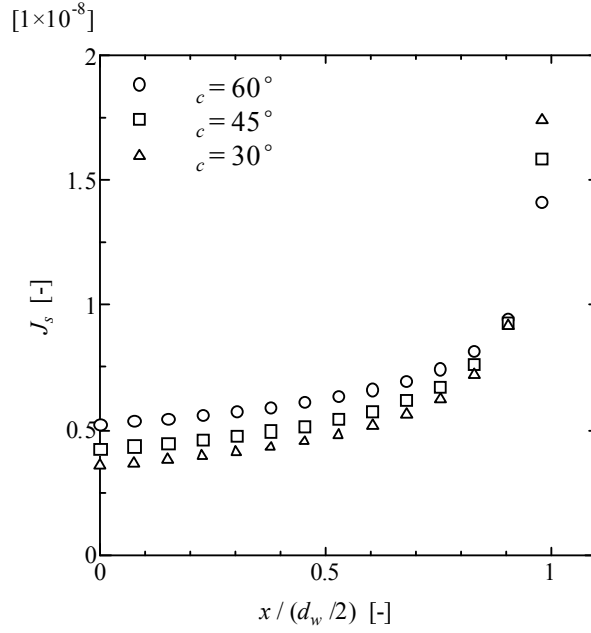


Fig. 4-13 Variation of  $J_s(x)$  at the position  $x$  of droplet surface for contact angle  $60^\circ$ ,  $45^\circ$  and  $30^\circ$ .

## 4.4 Conclusions

A two-dimensional lattice Boltzmann simulation of the evaporation of a single droplet on homogeneous substrates is performed. An evaporation model and a partial wetting boundary condition are used in the simulation to investigate the contact line motion and fluid flows in an evaporating droplet on wetting substrates. The major conclusions can be summarized as follows.

During the evaporation of a droplet on hydrophilic substrates, the wetting diameter decreases while the contact angle remains almost constant throughout the evaporation when the original partial wetting boundary condition is imposed. This is because the original partial wetting boundary condition assumes the equilibrium shape of the droplet. In order to take into account the dynamical changes in the contact angle in the pinning stage of evaporation, the partial wetting boundary condition is modified by using the relationship between the change in the droplet volume and the contact angle when the contact line is pinned. Then, the result obtained with the modified partial wetting boundary condition shows the three stages

of evaporation, which agree with experimental observations. The effect of the evaporation rate on the contact line motion of an evaporating droplet is negligibly small under the present conditions.

The vertically averaged fluid velocity in the  $x$ -direction increases towards the contact line of the droplet and takes the maximum value near the interface region of the droplet. However, the fluid velocity is not equal to zero at the beginning of the contact line pinning stage. This result may be associated with the spurious velocity formed in the interface region. In addition, the evaporation rate has less influence on the vertically averaged fluid velocity. From this result, the present evaporation model is required to be modified by giving the evaporation terms into particle distribution function for momentum in lattice Boltzmann equations. Furthermore, heat transfer inside an evaporating droplet should be solved for the precise evaluation of evaporation rate.

## **Chapter 5 A Lattice Boltzmann Simulation for Contact Line Motion of Evaporating Droplet on Patterned Substrates**

### **5.1 Introduction**

Inkjet printing technology can coat functional materials only on specific area with small quantities of microdroplet. However, this technology has drawbacks in the formation of micropatterned thin film due to accuracy of droplet positioning and the size of droplets formed. The accuracy of droplet positioning is over 10  $\mu\text{m}$ , and the minimum size of droplet is around 10~20  $\mu\text{m}$ . These indicate that it is quite difficult to form patterned thin films with the size less than 10  $\mu\text{m}$ . To overcome these drawbacks, the utilization of patterned hydrophilic surface has been proposed [7]. In this case, inkjet droplets can deposit with microstructured less than 10  $\mu\text{m}$  on the patterned substrate, and then the thin film will be formed only on the hydrophilic area after drying the droplets. In this application, the contact line motion during the evaporation of droplets affects greatly on the shape of micropatterned thin film.

In this chapter, a two-phase lattice Boltzmann simulation is performed to investigate the contact line motion of an evaporating droplet on a patterned substrate of line shape hydrophilic region. The effects of the width of hydrophilic region and the evaporation rate on the contact line motion are discussed.

### **5.2 Numerical simulation**

#### **5.2.1 Computational domain**

The physical problem and computational domain of a droplet on a patterned substrate are shown in Fig. 5-1. The computational domain is a two-dimensional Cartesian coordinate system and is divided into 400 ( $L_x$ ) $\times$ 150 ( $L_y$ ) lattices. Patterned substrate has a hydrophilic

region with the width of  $L_{w,phi}$  in the center of the hydrophobic substrate. A droplet is initially placed on the center of the patterned substrate. The initial shape of the droplet is a spherical cap with the wetting diameter  $d_w$ , the height at the center  $h$  and contact angle  $\theta_c$  on the substrate.

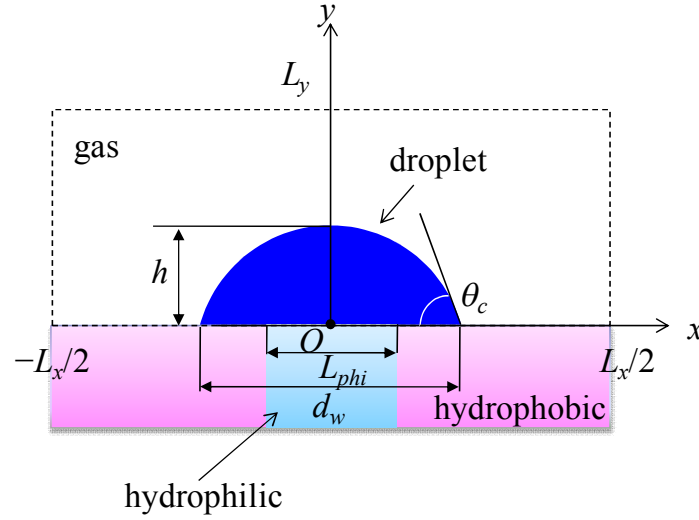


Fig. 5-1 Physical problem and computational domain of droplet on heterogeneous substrates. The blue region represents the hydrophilic region with width  $L_{w,phi}$ ; pink region lying on the two side of blue region represents the hydrophobic region of the substrate.

### 5.2.2 Two Phase lattice Boltzmann model

A two-phase lattice Boltzmann model proposed by Lee and Lin [42] is employed to simulate the evaporation of a droplet on a patterned substrate. As introduced in Chapter 2, this two-phase LB model employs two particle distribution functions; one is utilized to distinguish the two phase and the other is used to calculate the momentum of two phase flows. An evaporation model proposed in Chapter 2 is applied to simulate the mass loss of liquid phase. An adhesive force is incorporated into the LB model to describe the wettability of the patterned substrates. Cyclic boundary conditions are given at  $x = -L_x/2$  and  $L_x/2$ , and mass conserving boundary condition [89] is given at  $y = 0$ . The details of the mathematical models are presented in Chapter 2.



### 5.2.3 Computation conditions

Simulation parameters and physical properties are shown in Table 5-1. In order to relate the physical properties to the simulation parameters, Ohnesorge number, Oh, and Bond number, Bo, are set to  $1.18 \times 10^{-2}$  and  $1.36 \times 10^{-3}$ , respectively. The width of hydrophilic region of the patterned substrate  $L_{w,phi}$  is varied from 30 to 70. The static contact angles of hydrophilic and hydrophobic regions are  $42.7^\circ$  and  $121.8^\circ$ , respectively. The evaporation rate coefficient is set to  $1.0 \times 10^{-4}$  and  $2.0 \times 10^{-4}$ .

Table 5-1 Computational conditions

	Simulation parameters	Physical properties
Liquid density ( $\rho_L$ )	1.0	$1000 \text{ kg m}^{-3}$
Gas density ( $\rho_G$ )	$1.2 \times 10^{-3}$	$1.2 \text{ kg m}^{-3}$
Liquid/Gas viscosity ( $\mu_L/\mu_G$ )	55.6	55.6
Surface tension ( $\sigma_{LG}$ )	$2.09 \times 10^{-3}$	$7.2 \times 10^{-2} \text{ N m}^{-1}$
Interface width ( $D$ )	12	-
Initial wetting diameter ( $d_{w,0}$ )	100	$2.0 \times 10^{-4} \text{ m}$
Gravity acceleration ( $g$ )	$1.14 \times 10^{-9}$	$9.8 \text{ m s}^{-2}$

## 5.3 Results and Discussion

Fig. 5-2 shows the density distribution and fluid velocity in an evaporating droplet. Circulation flows inside the droplet are observed near the boundary between hydrophilic and hydrophobic region. The circulation flows are caused by the large jump of the adhesive force between the hydrophilic and hydrophobic regions, as shown in Fig. 5-3, because the opposite direction of the adhesive force acts on one node between the hydrophilic and hydrophobic regions. The opposite value of the adhesive force on the patterned substrate will affect the circulation flows between the hydrophilic and hydrophobic regions. This unphysical circulation flows lead to the density decrease inside the droplet near the substrate.

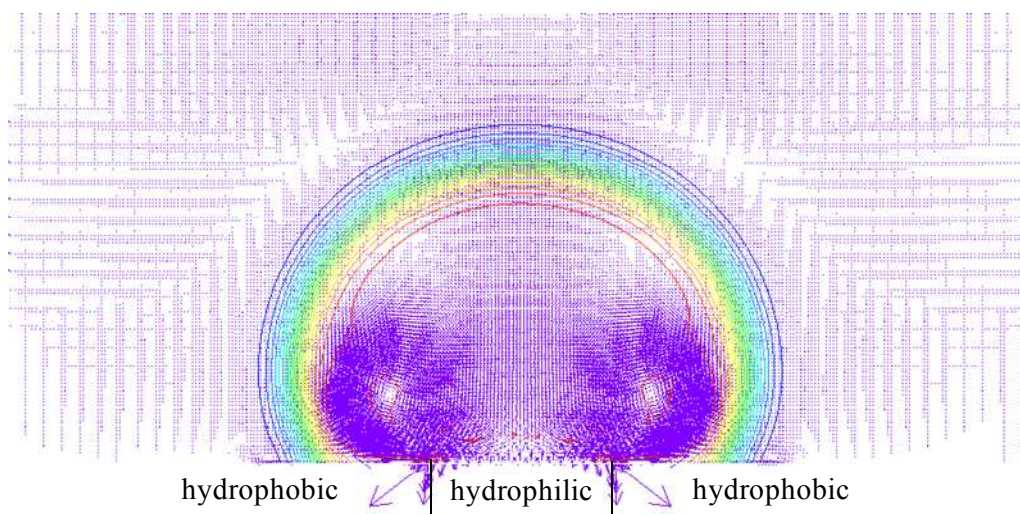


Fig. 5-2 Density and internal fluid flows of droplet with evaporation on patterned substrate. ( $t = 1.0 \times 10^4$  steps)

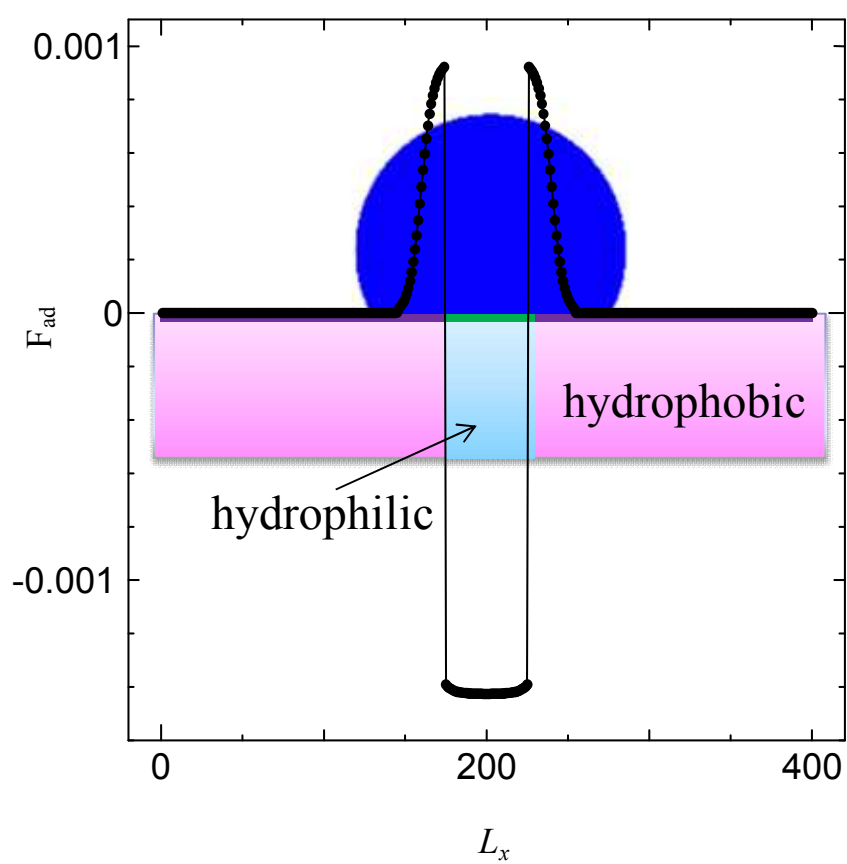


Fig. 5-3 Distribution of adhesive force on patterned substrate.

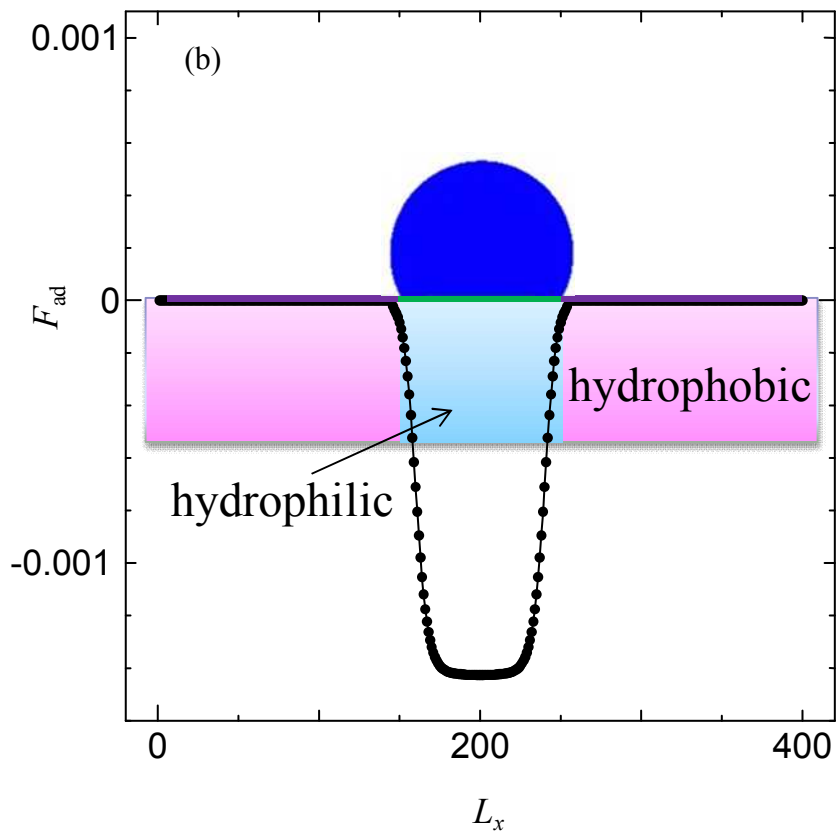
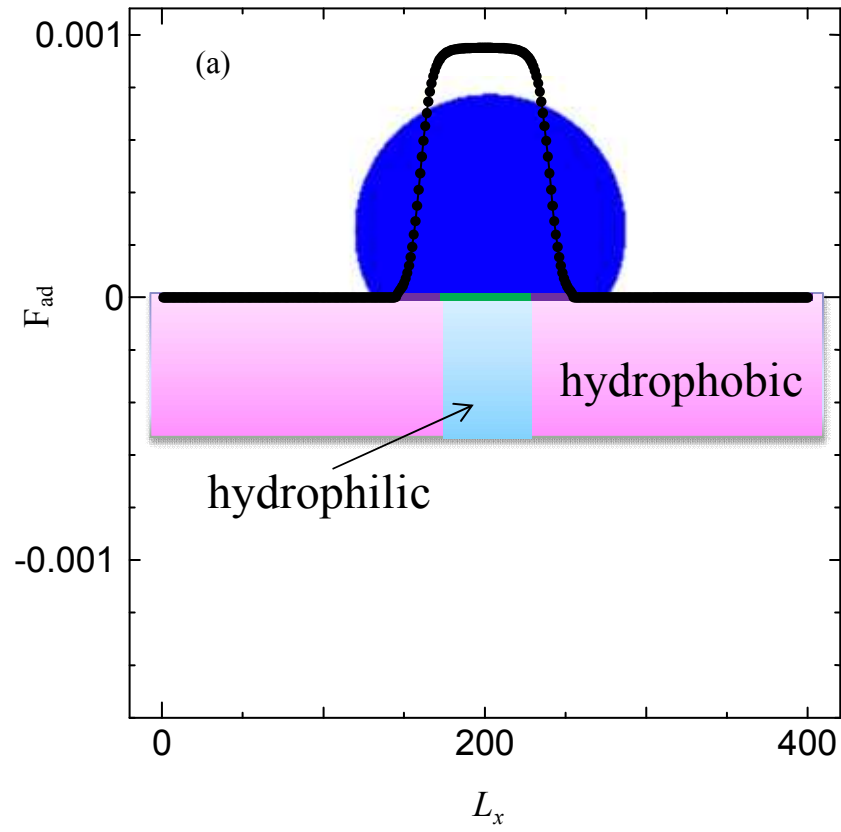


Fig. 5-4 Distribution of modified adhesive force on patterned substrate, (a) contact line is on hydrophobic region (b) contact line reaches on hydrophobic region.

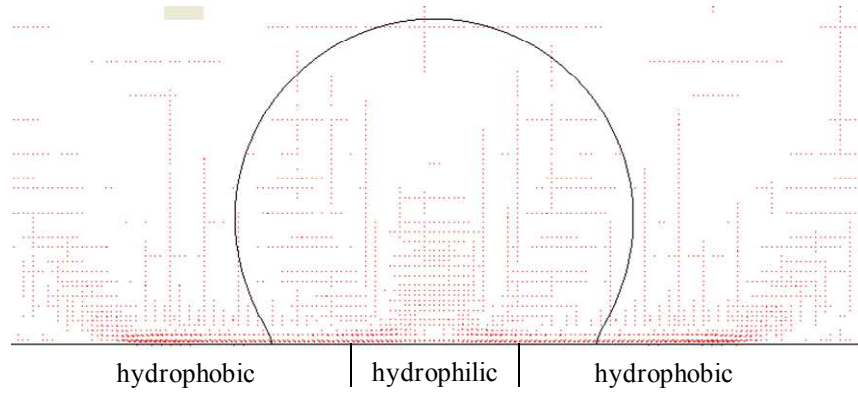


Fig. 5-5 Density and internal fluid flows of droplet with evaporation on patterned substrate.

To solve this problem, the adhesive force on the patterned substrate is modified as follows. Fig. 5-4 shows the distribution of the modified adhesive force on the patterned substrate. When a contact line of the droplet is on the hydrophobic region (Fig. 5-4(a)), the adjusting parameter for adhesive force  $G_{ad}$  is set to the value of the hydrophobic region. In contrast, when a contact line is on the hydrophilic region (Fig. 5-4(b)), the adjusting parameter for adhesive force is set to the value of the hydrophilic region. Fig. 5-5 shows the density distribution and fluid velocity by giving the modified adhesive force. The large circulation flow is not observed in this figure, leading to the no density decrease inside the droplet. Therefore, from now on, the modified adhesive force is applied to the modeling of the wettability of the patterned substrate.

Fig. 5-6 shows the time variation of the droplet shape during evaporation on the patterned substrate with the evaporation rate coefficient  $\varepsilon_{ev}$  of  $1.0 \times 10^{-4}$ . The patterned substrate has a hydrophilic region with the width  $L_{w,phi}$  of 50 in hydrophobic substrate. During the evaporation process, the size of droplet decreases with increasing time steps. At the beginning of the evaporation, the contact line recedes towards the centre of droplet. When the contact line reaches to the hydrophilic region, the receding is stopped temporarily. The height of the droplet decreases and the contact line is pinned at the boundary between the hydrophilic and hydrophobic region. Finally, the contact line recedes again and the droplet disappears at the termination of evaporation.

Fig. 5-7 shows the time variations of the wetting diameter and contact angle during the

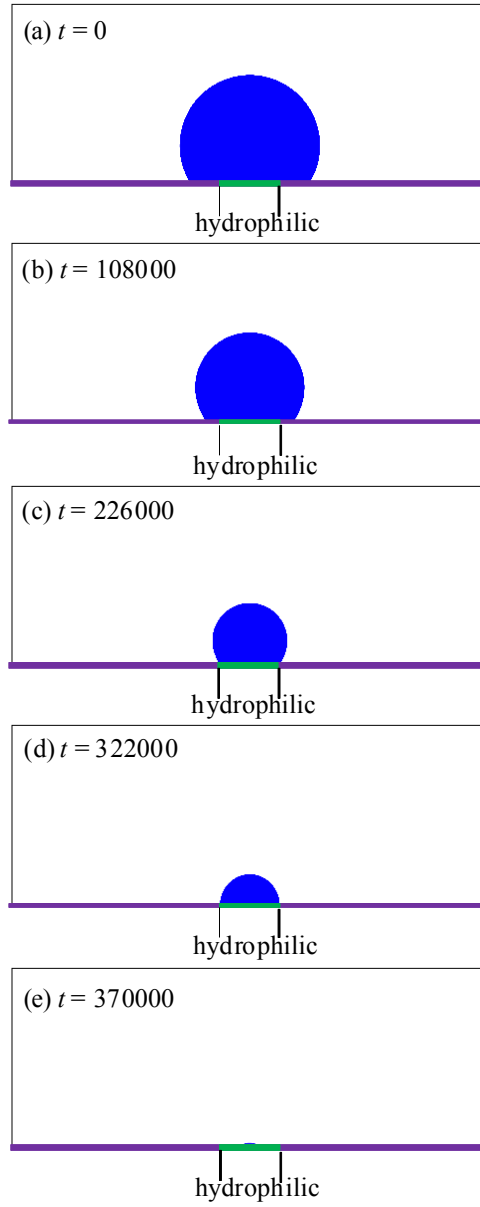


Fig. 5-6 Time variations of the evaporating droplet on the patterned substrate. Evaporation rate coefficient  $\varepsilon_{ev} = 1.0 \times 10^{-4}$ .

evaporating process of the droplet on the patterned substrate. In this figure, three stages of contact line motion are observed. In the first stage (stage I), the wetting diameter decreases, whereas the contact angle remains constant. This indicates that the contact line motion of the droplet is in de-pinning. After, the contact line recedes close to the hydrophilic region, the contact line motion of the droplet is in the second stage. This is because the magnitude of  $d_w$  is about 51.6, this value is almost same with the width of the hydrophilic region  $L_{w, \phi}$  of 50, which is observed in this figure. In the stage II, the wetting diameter keeps constant while the

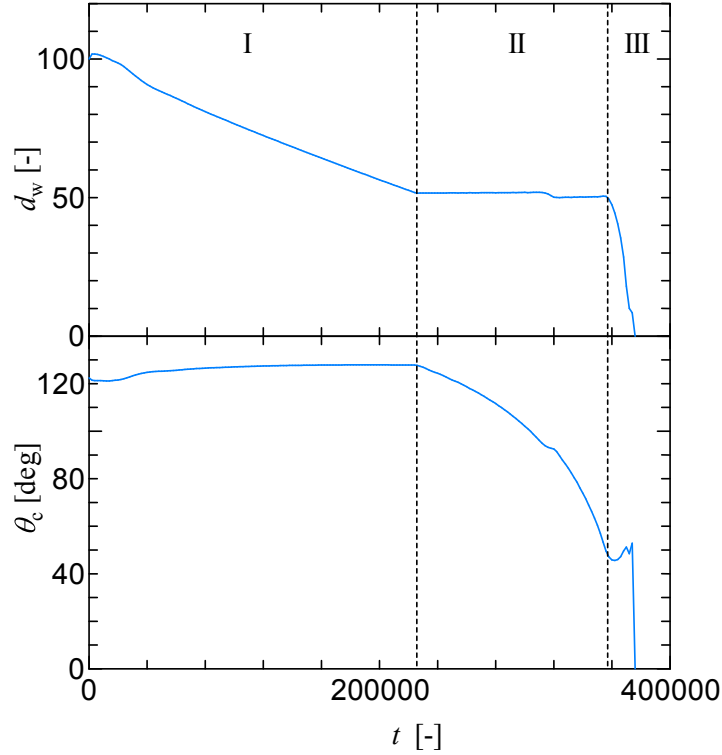


Fig. 5-7 Time variations of the wetting diameter and contact angle during the evaporating process of the droplet on the patterned substrate. Evaporation rate coefficient  $\varepsilon_{ev} = 1.0 \times 10^{-4}$ .

contact angle decreases, which can account for the contact line motion is in the pinning stage. Then, the wetting diameter decreases again when the contact angle reaches to around static contact angle (is equal to about  $46^\circ$  in this result), indicating the contact line motion is into the third stage. In the stage III, the contact angle shows a little increase and then decrease rapidly while the wetting diameter decrease near the termination of evaporation. This little increase and subsequent rapid decrease in the contact angle may be caused by an increase in the interface width due to computation error.

Fig. 5-8 shows the time variation of wetting diameter and contact angle of an evaporating droplet with the evaporation rate coefficient  $\varepsilon_{ev}$  of  $1.0 \times 10^{-4}$  and  $2.0 \times 10^{-4}$  on the patterned substrate. Three stages of contact line motion can be observed for both evaporation rate coefficients. The change from stage I to stage II is because the contact line position reaches to the hydrophilic region. In the stage II, when the contact angle decreases to the static contact angle of the droplet on hydrophilic substrate, the contact line motion will change to stage III.

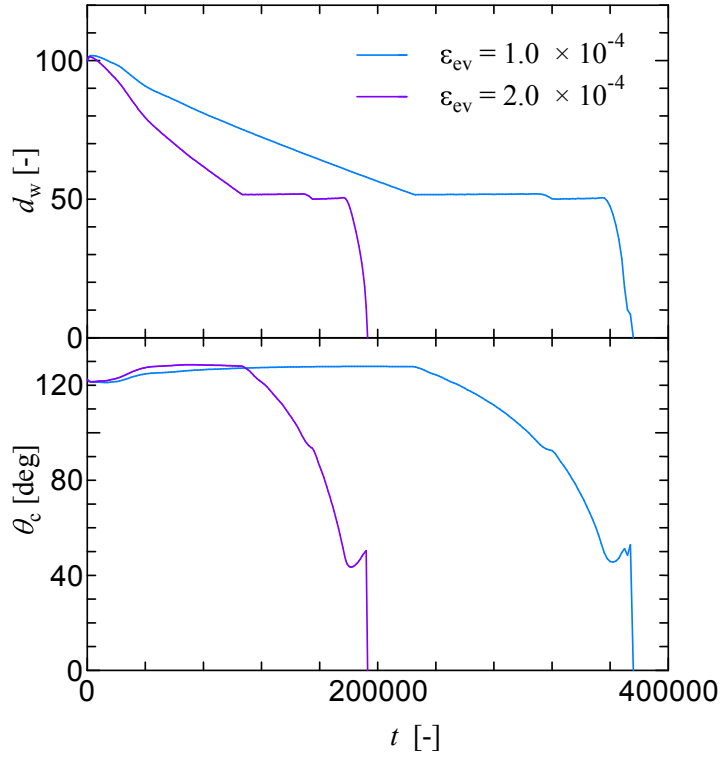


Fig. 5-8 Time variations of the wetting diameter and contact angle during the evaporating process of droplet on patterned substrate. Evaporation rate coefficient are set to  $\varepsilon_{ev} = 1.0 \times 10^{-4}$  and  $\varepsilon_{ev} = 2.0 \times 10^{-4}$ .

The termination time of droplet evaporation for  $\varepsilon_{ev}$  of  $2.0 \times 10^{-4}$  is shorter than that for  $\varepsilon_{ev}$  of  $1.0 \times 10^{-4}$ . This is because the rate of mass loss increases when the evaporation rate coefficient increases.

Fig. 5-9 shows the variation of wetting diameter and contact angle of an evaporating droplet with the evaporation rate coefficient  $\varepsilon_{ev}$  of  $1.0 \times 10^{-4}$  on the patterned substrate. The width of the hydrophilic region of the patterned substrate  $L_{w,phi}$  is varied to 30, 50 and 70. Three stages of contact line motion are observed for  $L_{w,phi}$  of 30, 50 and 70. The changes from stage I to stage II starts from the time when the wetting diameter decreases to the width of hydrophilic region. The reason is because the contact line reaches to the hydrophilic region and then the contact line motion is in the pinning stage. In stage II, the pinning time increases with the width of hydrophilic region. In addition, the termination time of droplet evaporation is different for  $L_{w,phi}$  of 30, 50 and 70 with same  $\varepsilon_{ev}$  of  $1.0 \times 10^{-4}$ . The termination time of droplet evaporation on a patterned substrate decreases with increasing the  $L_{w,phi}$  from 30 to

70. This may be caused by the surface area of the evaporating droplet in pinning stage is larger than that in de-pinning stage, if the volume of droplet has same value.

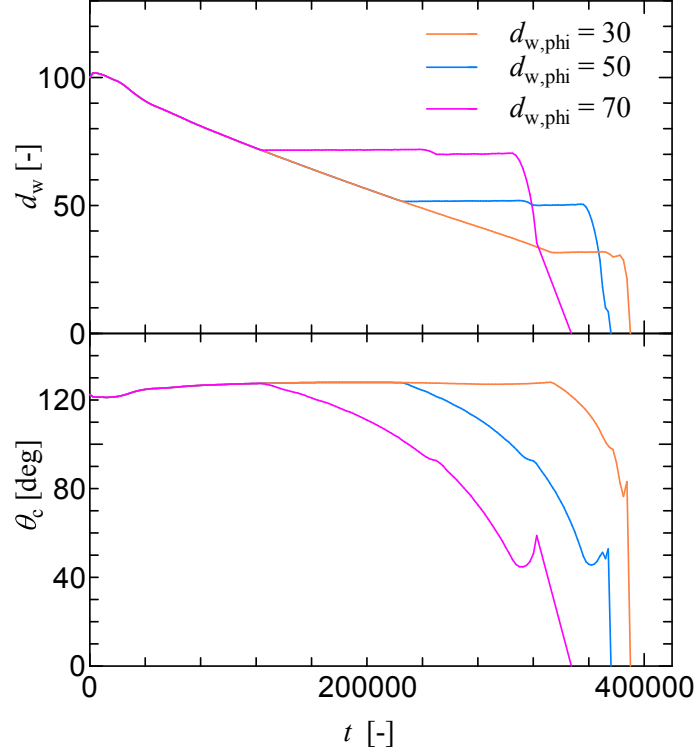


Fig. 5-9 Time variation of wetting diameter and contact angle of the evaporating droplet with evaporation rate coefficient  $\varepsilon_{ev}$  of  $1.0 \times 10^{-4}$  on patterned substrate. The patterned substrate with width of hydrophilic region  $L_{w,phi} = 30, 50$  and  $70$ .

## 5.4 Conclusions

A two-phase lattice Boltzmann simulation is performed to investigate the evaporation of a single droplet on patterned substrates with different wettability. An evaporation model is applied to the simulation by modeling the mass loss in the interface region between droplet liquid and gas phase. To avoid unphysical circulation flows and density decrease inside the droplet near the substrate, a modified adhesive force is incorporated into the present LB model which can give wettability of the patterned substrate. Three stages of contact line motion of droplet can be observed for various evaporation rate coefficient and the width of hydrophilic region. In the initial stage of evaporation, the contact line motion shows



de-pinning because the contact line is placed on the hydrophobic region. When the contact line recedes and reaches to the hydrophilic region, the contact line is pinned. As the evaporation progresses, the contact line is de-pinned again when the contact angle decreases to the static contact angle of the hydrophilic region. The termination time of droplet evaporation increases when the evaporation rate coefficient decreases. In addition, the termination time of droplet evaporation decrease with increasing the width of hydrophilic region, because of the difference in the surface area of the droplet.

## Chapter 6 A Lattice Boltzmann Simulation for Solid Particle Transport after a Droplet Evaporation on Homogenous Substrate

### 6.1 Introduction

Because inkjet printing can form micron-size droplet, it has been applied to electrical manufacturing such as organic thin film transistors [3]. However, solid particles inside evaporating droplets will be transported toward the perimeter of the droplets, and then the ring-like deposit will be formed. To investigate the nonuniform thin film formation, solid particles transport inside evaporating droplets has been focused in experimental and theoretical studies. It is well known that the ring-like deposit is caused by the internal fluid flows with solid particles transport to the contact line of evaporating droplet when contact line pinned [5]. However, it is unclear what conditions will affect on the solid particles transport inside droplet and the shape of thin film after droplet evaporation.

In this chapter, a solid particles transport model proposed in Chapter 2 is incorporated into the two-phase lattice Boltzmann model [43] to simulate solid particles transport and deposit after droplet evaporation.

### 6.2 Numerical simulation

The physical problem and computational domain of a droplet with solid particles on homogenous substrates are shown in Fig. 6-1. The computational domain is a two-dimensional Cartesian coordinate system and is divided into 80 ( $L_x$ ) $\times$ 30 ( $L_y$ ) lattices. A single droplet with solid particles is placed on a substrate with homogenous wettability (hydrophilic:  $\theta_c < 90^\circ$  hydrophobic:  $\theta_c > 90^\circ$ ). A single droplet with an initial contact angle of  $\theta_{c,0}$  of  $90^\circ$  is initially placed on a substrate with a given static contact angle  $\theta_{c,g}$  of  $60^\circ$ . The wetting diameter and the height from the droplet center are denoted by  $d_w$  and  $h$ .

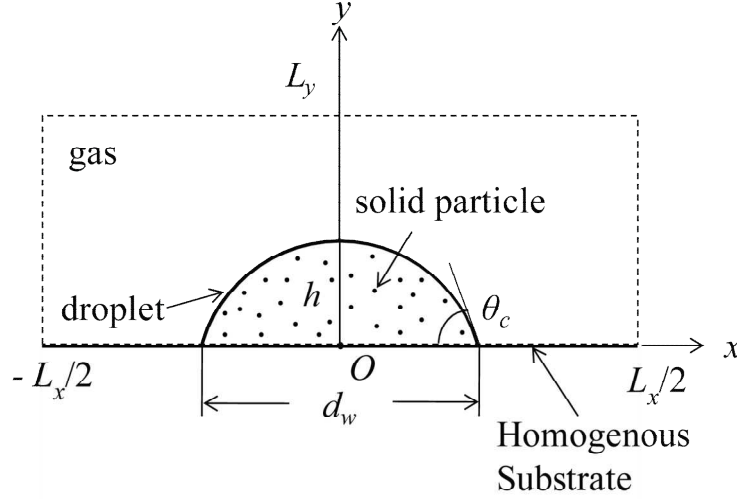


Fig. 6-1 Physical problem and computational domain of droplet with solid particles on homogenous substrates.

A two-phase lattice Boltzmann model proposed by Inamuro *et al.* [43] is employed to simulate the evaporation of a droplet on homogenous substrates. As introduced in Chapter 2, this two-phase lattice Boltzmann model employs two particle distribution functions; one is utilized to distinguish the two phase and the other is used to calculate the momentum of two phase flows. An evaporation model proposed in Chapter 2 is applied to simulate the mass loss of liquid phase. A partial wetting boundary condition is incorporated into the lattice Boltzmann model to describe the wettability of the substrates. A solid particles transport model proposed in Chapter 2 is used to calculate the particle motion inside the evaporating droplet. The details of the mathematical models are presented in Chapter 2.

On the boundaries at  $x = 0$ ,  $x = L_x$ , and  $y = L_y$ , non-slip boundary condition is given, and the normal derivatives of the order parameter, and the predicted and corrected velocities are set to zero. On the boundary at  $y = 0$ , the partial wetting boundary condition is imposed, the predicted and corrected velocities are set to zero.

The maximum and minimum values of the order parameter are  $\phi_{min} = 9.999 \times 10^{-6}$  and  $\phi_{max} = 4.5 \times 10^{-5}$ . In order to relate the physical properties to the simulation parameters, the length scale, time scale, and mass scale are given as  $L_0 = 1.0 \times 10^{-4}$  m,  $T_0 = 2.635 \times 10^{-9}$  s, and  $M_0 = 1.0 \times 10^{-12}$  kg, respectively. Evaporation rate coefficient  $\varepsilon_{ev}$  is set to  $1.0 \times 10^{-7}$ . The number

Table 6-1 Computation conditions of liquid droplet

	Simulation parameters	Physical properties
Liquid density ( $\rho_L$ )	1000	1000 kg m <sup>-3</sup>
Gas density ( $\rho_G$ )	1.29	1.29 kg m <sup>-3</sup>
Liquid order parameter ( $\phi_L$ )	$4.0 \times 10^{-5}$	-
Gas order parameter ( $\phi_G$ )	$1.0 \times 10^{-5}$	-
Liquid viscosity ( $\mu_L$ )	$2.635 \times 10^{-4}$	$1.0 \times 10^{-3}$ Pa s
Gas viscosity ( $\mu_G$ )	$4.743 \times 10^{-6}$	$1.8 \times 10^{-5}$ Pa s
Surface tension ( $\sigma_{LG}$ )	$5.0 \times 10^{-7}$	$7.2 \times 10^{-2}$ N m <sup>-1</sup>
Interface width ( $D$ )	3	-
Initial wetting diameter ( $d_{w,0}$ )	20	$2.0 \times 10^{-3}$ m
Gravity acceleration ( $g$ )	$6.80436 \times 10^{-13}$	$9.8$ m s <sup>-2</sup>

Table 6-2 Physical properties of solid particles

	Simulation parameters	Physical properties
Density ( $\rho_p$ )	1050	1050 kg m <sup>-3</sup>
Radius ( $r_p$ )	0.005	$5.0 \times 10^{-7}$ m
Hamaker constant of particles ( $A_{11}$ )	$4.56864 \times 10^{-17}$	$6.58 \times 10^{-20}$ J
Hamaker constant of medium ( $A_{22}$ )	$2.56899 \times 10^{-17}$	$3.70 \times 10^{-20}$ J
Free energy of particle-solution interaction ( $\gamma$ )	$2.77729 \times 10^{-8}$	$4 \times 10^{-3}$ Nm <sup>-1</sup>

of solid particles is set to 100. The computation conditions are shown in Table 6-1. The simulation parameters of solid particle transport are shown in Table 6-2. The Hamaker

constants and free energy of particle-solution interaction are referred as polystyrene particle in water medium [94, 95].

## 6.3 Results and Discussion

### 6.3.1 Solid particles transport inside an evaporating droplet

Fig. 6-2 shows the time variation of liquid-vapor interface and solid particles position. Colloid particles are randomly dispersed inside the liquid droplet as shown in Fig. 6-2(a). Before beginning of the evaporation at  $t = 9.8 \times 10^6$  steps, the droplet interface motion are only controlled by the wettability of substrate to reach equilibrium. Fig. 6-2(b) shows the interface of liquid-gas and the particle position at time of  $t = 9.8 \times 10^6$  steps. The droplet spreads on the substrate leading to the solid particles movement to downward from their initial position. The particles transport is affected by interface motion of liquid-vapor. After  $t = 9.8 \times 10^6$  steps, the evaporation starts, the particles are transported by the wettability of substrate. Fig. 6-2(c) shows the position of liquid-vapor interface and solid particles at  $t = 1.86 \times 10^7$  steps. The solid particles are further transported to downward.

In order to know how the solid particles are transported in an evaporating droplets, the trajectories of solid particles from the beginning to the termination of the evaporation ( $t = 9.8 \times 10^6$  to  $2.72 \times 10^7$ ) are shown in Fig. 6-3. In this figure, the solid particles are transported toward the vicinity of the substrate with increasing time. In the last stage of evaporation, the solid particles are remarkably transported to the centre of the droplet. This may be because the contact line motion is in the mixture of pinning and de-pinning stage. In this case, the contact line moves toward the center of droplet rapidly which will cause the solid particles transport to the center controlled by the force of interaction  $\vec{F}_l$  (in Chapter 2). In the past research [5, 20], the solid particles are transported toward the contact line when the contact line of an evaporating droplet is pinned on substrates. However, in the present simulation, the solid particles move to center. In the present simulation, the evaporation termination time is approximately about 0.05s, which is quite smaller than the experiments. In this case, the

contribution of the interaction force caused by interface is larger than that of the internal fluid flows toward the contact line.

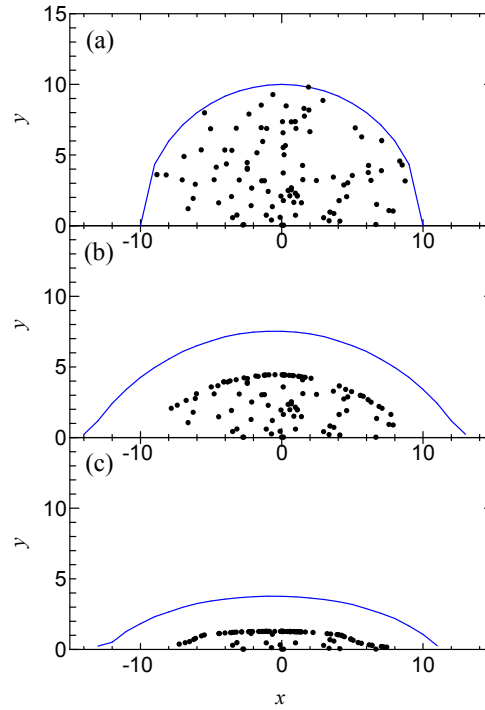


Fig. 6-2 Time variation of liquid-vapor interface (blue line) and solid particles position (solid circle). (a) The droplet is in initial state, at  $t = 0$  steps; (b) the droplet without evaporation reached steady state at  $t = 9.8 \times 10^6$  steps; (c) the droplet is in the middle evaporation at  $t = 1.86 \times 10^7$  steps.

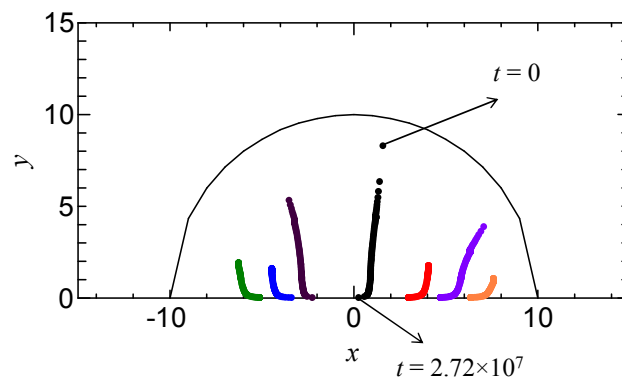


Fig. 6-3 Trajectories of solid particles from beginning to the termination of evaporation ( $t = 0$  to  $2.72 \times 10^7$ )

### 6.3.2 Solid particles deposit after droplet evaporation

The shape of solid particles deposit is evaluated by number distribution deposit on the substrate after droplet evaporation. Fig. 6-4 shows the distribution of number of solid particles deposit on the substrate at  $t = 2.74 \times 10^7$  steps (after droplet evaporation). The number of particles is larger in center of the droplet which indicates that the shape of particle deposit is dot-like structure after droplet evaporation. The result of solid particles deposit can be explained by solid particles transport to the center of the evaporating droplet as mentioned above. However, this result is inconsistent with the result in past researches which shows a ring-like deposit of solid particles. This may be because the contribution of the interaction force caused by interface between liquid and vapor phase is larger than that of the fluid flows under high evaporation rate condition.

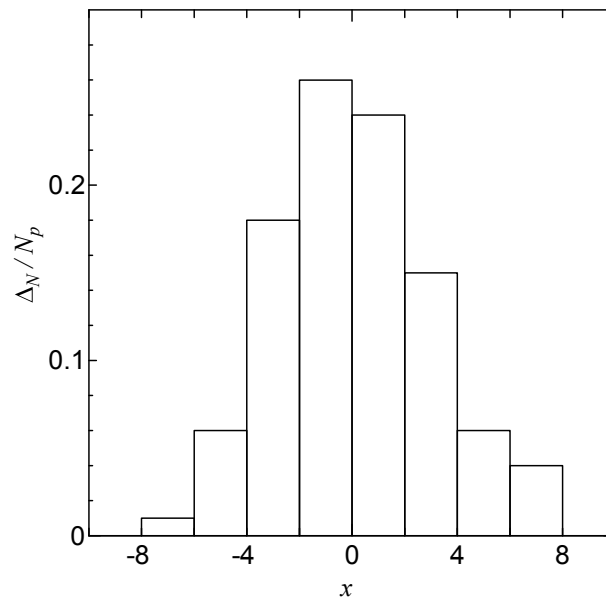


Fig. 6-4 The distribution of the number of solid particles at  $x$  position on substrate for time  $t = 2.74 \times 10^7$  steps.

## 6.4 Conclusions

A two-phase lattice Boltzmann simulation of solid particles deposit in a drying droplet

on substrates is performed. The evaporation behavior of a droplet on a substrate is simulated by using a two-phase lattice Boltzmann model incorporated with an evaporation model, a partial wetting boundary condition and a solid particles transport model proposed in Chapter 2 to describe the solid particle motion inside an evaporating droplet. Major findings are summarized as follows.

In the present simulation, the solid particles are transported downward and then toward centre of evaporating droplet on hydrophilic substrate. The shape of solid particles deposit shows the large numbers of particles in the center than that near the edge of the deposit. This result indicates that the shape of particles deposit is dot-like, which is inconsistent with past experiments. From this result, the interaction force caused by interface is required to modify, because the shape of particles deposit is seemed to be greatly affected. Furthermore, reduction of the evaporation rate is required to prevent the solid particles transport to the centre of an evaporating droplet on hydrophilic substrate.



## Chapter 7 Conclusions

The main contribution of the present dissertation is the development and application of numerical simulation to investigate the evaporation behavior and solid particles deposit of a sessile droplet on substrates.

The first chapter presents the background of industrial applications of inkjet printing to thin film formation, and the objective of this study. Outline of the present dissertation is also introduced in this chapter. In addition, the evaporation behavior as well as internal fluid flows and thin film formation after drying of a sessile droplet on substrates in experiment, theoretical and numerical simulation is summarized in the literature review.

The second chapter shows a mathematical model which is composed of a two-phase lattice Boltzmann model, a wetting model, an evaporation model and a solid particles transport model. To simulate two-phase flows, two-phase lattice Boltzmann simulation of Lee and Lin's model [42] and Inamuro's model [43] are introduced. Two kinds of wetting models are presented to describe the wettability of substrate. These wetting models given by a partial wetting boundary condition and an adhesive force model are incorporated into two-phase lattice Boltzmann models proposed by Inamuro *et al.* and Lee and Lin. The spread of a droplet on the substrate are simulated by using these two wetting models to confirm the validity of the wettability of substrates. To describe the evaporation of liquid phase on the droplet surface, an evaporation model is proposed. The evaporation term is incorporated into two-phase lattice Boltzmann model, which indicates the rate of mass loss in the interface region of liquid-vapor phase. The validity of the present evaporation model is confirmed by simulating the evaporation of a single droplet in ambient vapor. The result shows a good agreement with the  $d^2$ -law for an evaporating droplet. In addition, a solid particles transport model is proposed and is incorporated into the lattice Boltzmann simulation to describe the solid colloidal particles motion in an evaporating droplet. The solid particles motion is evaluated by solving a Newton equation for each solid particle inside the droplet on substrate.

The third chapter shows the effect of computational parameters on the reduction of

spurious velocities that appear in the simulation of a droplet in ambient vapor. The maximum spurious velocities can be reduced up to approximately  $10^{-14}$  by giving a small dimensionless surface tension. This spurious velocity corresponds to  $10^{-8}$  m/s, and is sufficiently small to neglect the internal fluid flow caused by the spurious velocities in an evaporating droplet on a substrate. In addition, the effects of order parameter and density ratio are also simulated. However, only the dimensionless surface tension parameter greatly influences the reduction of the spurious velocities in two-phase fluids and the liquid-vapor interface.

The fourth chapter investigates the contact line motion and internal fluid flows of a single droplet evaporation on wetting substrates. A two-dimensional lattice Boltzmann model proposed by Inamuro *et al.* [43] is performed to simulate two-phase fluid flows. An evaporation model and a partial wetting boundary condition are incorporated into the lattice Boltzmann model. During the evaporation of a droplet on hydrophilic substrates, the wetting diameter decreases while the contact angle remains almost constant throughout the evaporation when the original partial wetting boundary condition is imposed. This is because the original partial wetting boundary condition assumes the equilibrium shape of the droplet. In order to take into account the dynamical changes in the contact angle in the pinning stage of evaporation, the partial wetting boundary condition is modified by using the relationship between the change in the droplet volume and the contact angle when the contact line is pinned. Then, the pinning, de-pinning and mixture of pinning and de-pinning stages of contact line motion are obtained with the modified partial wetting boundary condition, which agree with experimental observations. The vertically averaged fluid velocity in the  $x$ -direction increases towards the contact line of the droplet and takes the maximum value near the interface region of the droplet. In addition, the evaporation rate has less influence on the contact line motion and vertically averaged fluid velocity under the present conditions. From these result, the present evaporation model is required to modified by giving the evaporation terms into particle distribution function for momentum in lattice Boltzmann equations. Furthermore, heat transfer inside an evaporating droplet should be solved for the precious evaluation of the evaporation rate.

The fifth chapter investigates the effects of the width of hydrophilic region in a patterned substrate and the evaporation rate on the contact line motion by applying Lee and Lin's

two-phase lattice Boltzmann model [42] incorporated with an evaporation model and a wetting model given by adhesive force. A modified adhesive force is introduced to describe wettability of patterned substrates, which can avoid unphysical circulation flows and density decrease inside the droplet near the substrate. In the results, the de-pinning, pinning and de-pinning of contact line motion of an evaporating droplet on patterned substrates can be observed for various evaporation rate coefficient. The termination time increases with decreasing the evaporation rate coefficient. The pinning time becomes longer if the width of hydrophilic region increase. However, the termination time decreases with increasing width of hydrophilic region. This may be caused by the difference in the surface area of the droplet.

In sixth chapter, a numerical simulation is performed to investigate a solid particles transport and deposit of an evaporating droplet on homogenous substrates. In the simulation results, the solid particles transport can be observed during droplet evaporation. However, the solid particles are transported toward the centre of the droplet and forms dot-like deposit after droplet evaporation on hydrophilic substrate. These results are inconsistent with experimental results. This may be because the contribution of the interaction force caused by interface between liquid and vapor phase is larger than that of the fluid flows under high evaporation rate condition. Therefore, further reduction of the evaporation rate is required to prevent the solid particles transport to the centre of an evaporating droplet on hydrophilic substrate.

In future work, the mathematical model such as evaporation model, solid particles transport model will be modified. In the present study, the 2D simulation is performed, however, 3D simulation is required to investigate the evaporation behavior and solid particles deposit on patterned substrate with line-shape or dot shape. Furthermore, the heat transfer in an evaporating droplet will be incorporated into evaporation model, this is because the heat transfer will affect the evaporation flux on the droplet surface.

## References

- [1] E. R. Lee, Microdrop generation. CRC PRESS. Boca Raton London New York Washington, D.C., 2003
- [2] R. Danzebrink and M. A. Aegerter, Deposition of micropatterned coating using an ink-jet technique, *Thin Solid Films*, **351**, 115-118, 1999
- [3] H. Sirringhaus, T. Kawase, R. H. Friend, T. Shimoda, M. Inbsekaran, W. Wu and EP. Woo, High-Resolution inkjet printing of all-polymer transistor circuits, *Science*, **290**, 2123-2126, 2000.
- [4] E. A. Roth, T. Xu, M. Das, C. Gregory, J. J. Hickman and T. Boland, Inkjet printing for high-throughput cell patterning, *Biomaterials*, **25**, 3707-3715, 2004.
- [5] R. D. Deegan, O. Bakajin, T. F. Dupont, G. Huber, S. R. Nagel, T. A. Witten, Capillary flow as the cause of ring stains from dried liquid drops, *Nature*, **389**, 827-829, 1997.
- [6] M. Morita, T. Koga, H. Otsuka and A. Takahara, Macroscopic-wetting anisotropy on the line-patterned surface of fluoroalkylsilane monolayers, *Langmuir*, **21**, 911-918, 2005.
- [7] M. Morita, S. Yasutake, H. Ishizuka, J. Fukai and A. Takahara, Site-selective coating of polymer thin film prepared by the ink-jet method on the patterned fluoroalkylsilane monolayer substrate, *Chem. Lett.*, **34**, 916-917, 2005.
- [8] M. Morita, S. Yasutake, H. Ishizuka, J. Fukai and A. Takahara, Site-selective formation of polymer ultrathin films using the ink-jet method onto patterned fluoroalkylsilane monolayer substrate, *表面科学*, **27** (2), 108-115, 2006.
- [9] M. Furusawa, T. Hashimoto, M. Ishida, T. Shimoda, H. Hasei, T. Hirai, H. Kiguchi, H. Aruga, M. Oda, N. Saito, H. Iwashige, N. Abe, S. Fukuta and K. Betsui, 19.5 L: Late-News paper: inkjet-printed bus and address electrodes for plasma display, *SID Symposium Digest of Technical papers*, **33**, 753-755, 2002.

- [10] T. Kawase, T. Shimoda, C. Newsome, H. Sirringhaus R. H. Friend, Inkjet printing of polymer thin film transistors, *Thin Solid Films*, **438-439**, 279-287, 2003.
- [11] H. H. Lee, K. S. Chou and K. C. Huang, Inkjet printing of nanosized silver colloids, *Nanotechnology*, **16**, 2436-2441, 2005.
- [12] W. R. Cox, T. Chen and D. J. Hayes, Micro-optics fabrication by ink-jet printing, *Optics & Photonics News*, 32-35, June 2001.
- [13] V. Dugas, J. Broutin and E. Souteyrand, Droplet evaporation study applied to DNA chip manufacturing, *Langmuir*, **21**, 9130-9136, 2005.
- [14] S. Y. Liu, H. Y. Tam and M. S. Demokan, Low-cost microlens array for long-period grating fabrication, *Electronics Letters*, **35** (1), 79-81, 1999.
- [15] D. J. Hayes, W. R. Cox and D. B. Wallace, Printing system for MEMS packaging. Proceedings of the *SPIE Conference on Micromachining and Microfabrication*, October, 2001.
- [16] M. E. R. Shanahan and C. Bourgès, Effects of evaporation on contact angles on polymer surfaces, *Int. J. Adhes. Adhes.*, **14**, 201-205, 1994.
- [17] C. Bourgès-Monnier and M. E. R. Shanahan, Influence of evaporation on contact angle, *Langmuir*, **11**, 2820-2829, 1995.
- [18] H. Hu and R. G. Larson, Evaporation of a sessile droplet on a substrate, *J. Phys. Chem. B.*, **106**, 1334-1344, 2002.
- [19] H. Hu and R. G. Larson, Analysis of the microfluid flow in an evaporating sessile droplet, *Langmuir*, **21**, 3963-3971, 2005.
- [20] R. D. Deegan, O. Bakajin, T. F. Dupont, G. Huber, S. R. Nagel, T. A. Witten, Contact line deposits in an evaporating drop, *Phys Rev E*, **62**, 756-764, 2000.
- [21] B. J. de Gans, P. C. Duineveld and U. S. Schubert, Inkjet printing of polymers: State of the art and future developments, *Adv. Mater*, **16** (3), 203-213, 2004.
- [22] Y. Morozumi, H. Ishizuka and J. Fukai, Solute deposit during evaporation of a sessile

- binary liquid micro-droplet on a substrate, *J. Chem. Eng. Japan*, **37**, 778-784, 2004.
- [23] J. Park and J. Moon, Control of colloidal particle deposit patterns within picoliter droplets ejected by ink-jet printing, *Langmuir*, **22**, 3506-3513, 2006.
- [24] J. Fukai, H. Ishizuka, Y. Ssakai, M. Kaneda, M. Morita and A. Takahara, effects of droplet size and solute concentration on drying process of polymer solution droplets deposited on homogeneous surfaces, *Int. J. Heat Mass Transfer*, **40**, 3561-3567, 2006.
- [25] J.-H. Kim, S. I. Ahn, J. H. kim and W.-C. Zin, evaporation of water droplets on polymer surfaces, *Langmuir*, **23**, 6163-6169, 2007.
- [26] D. Soltman and V. Subramanian, Inkjet-printed line morphologies and temperature control of the coffee ring effect, *Langmuir*, **24**, 2224-2231, 2008.
- [27] M. Kaneda, K. Hyakuta, Y. Takao, H. Ishizuka and J. Fukai, Internal flow in polymer solution droplets deposited on a lyophobic surface during a receding process, *Langmuir*, **24**, 9102-9109, 2008.
- [28] Y. Yoshitake, S. Yasumatsu, M. Kaneda, K. Nakaso and J. Fukai, Structure of circulation flows in polymer solution droplets receding on flat surfaces, *Langmuir*, **26**, 3923-3928, 2010.
- [29] P. J. Yunker, T. Still, M. A. Lohr and A. G. Yodh, Suppression of the coffee-ring effect by shape-dependent capillary interactions, *Nature*, **476**, 308-311, 2011.
- [30] J. Z.Wang, Z. H. Zhang, H. W. Li, W. T. S. Huck and H. Srringhaus, Dewetting of conducting polymer inkjet droplets on patterned surfaces, *Nature Materials*, **3**, 171-176, 2004.
- [31] Y. Jung, T. Kajiya, T. Yamaue and M. Doi, Film Formation kinetics in the drying process of polymer solution enclosed by bank, *Japanese Journal of Applied physics*, **48**, 031502, 2009.
- [32] D. H. Rothman and J. M. Keller. Immiscible cellular-automaton fluids. *J. Stat. Phys.*, **52**, 1119, 1988.

- [33] G. McNamara and G. Zanetti, Use of the Boltzmann equation to simulate lattice-gas automata, *Phys Rev Lett*, **61**, 2332, 1988.
- [34] Gunstensen AK., DH. Rothman, S. Zaleski and G. Zanetti. Lattice Boltzmann model of immiscible fluids. *Phys. Rev. A.*, **43**, 4320, 1991.
- [35] C. Appert and S. Zaleski. Lattice gas with a liquid-gas transition, *Phys. Rev. Lett.*, **64**, 1-4, 1990.
- [36] S. Chen, G. Doolen, K. Eggert, D. Grunau and E. Y. Loh, Local lattice-gas model for immiscible fluids, *Phys Rev A*, **43**, 7053, 1991.
- [37] S. Chen and G. D. Doolen, Lattice Boltzmann method for fluid flows, *Annu. Rev. Fluid Mech.*, **30**, 329-364, 1998.
- [38] X. Shan and H. Chen, Lattice Boltzmann model for simulating flows with multiple phase and components, *Phys. Rev. E.*, **47**(3), 1815-1819, 1993.
- [39] X. Shan and H. Chen, Simulation of nonideal gases and liquid-gas phase transitions by the lattice Boltzmann equation, *Phys. Rev. E.*, **49**, 2941-2948, 1994.
- [40] M. R. Swift, W. R. Osborn and J. M. Yeomans, Lattice Boltzmann simulation of nonideal fluids, *Phys. Rev. Lett.*, **75**, 830-833, 1995.
- [41] M. R. Swift, E. Orlandini, W. R. Osborn and J. M. Yeomans, Lattice Boltzmann simulation of liquid-gas and binary fluid systems, *Phys. Rev. E.*, **54**, 5041-5052, 1996.
- [42] T. Lee and C. Lin, A stable discretization of the lattice Boltzmann equation for simulation of incompressible two-phase flows at high density ratio, *J. Comp. Phys.*, **206**, 16-47, 2005.
- [43] T. Inamuro, T. Ogata, S. Tajima, N. Konishi, A lattice Boltzmann method for incompressible two-phase flows with large density differences, *J. Comp. Phys.*, **198**, 628-644, 2004.
- [44] Y. Tanaka, Y. Washio, M. Yoshino, T. Hirata, Numerical simulation of dynamic behavior of droplet on solid surface by the two-phase lattice Boltzmann method, *Comput.*

*Fluids*, **40**, 68-78, 2011.

- [45] Y. Y. Yan and Y. Q. Zu, A lattice Boltzmann method for incompressible two-phase flows on partial wetting surface with large density ratio, *J. Comput. Phys.*, **227**, 763-775, 2007.
- [46] A. J. Briant, P. Papatzacos and J. M. Yeomans, Lattice Boltzmann simulations of contact line motion in a liquid-gas systems, *Phil. Trans. R. Soc. Lond. A.*, **360**, 485-495, 2002.
- [47] A. J. Briant, A. J. Wagner and J. M. Yeomans, Lattice Boltzmann simulations of contact line motion. I. Liquid-gas systems, *Phys. Rev. E.*, **69**, 031602, 2004.
- [48] A. J. Briant and J. M. Yeomans, Lattice Boltzmann simulations of contact line motion. II. Binary fluids, *Phys. Rev. E.*, **69**, 031603, 2004.
- [49] H. W. Zheng, C. Shu and Y. T. Chew, A lattice Boltzmann model for multiphase flows with large density ratio, *J. Comput. Phys.*, **218**, 353-371, 2006.
- [50] R. Begum and M. A. Basit, Lattice Boltzmann method and its applications to fluid flow problems, *Euro. J. Sci. Res.*, **22**, 216-231, 2008.
- [51] R. Ouared and B. Chopard, Lattice Boltzmann simulations of blood flow: Non-Newtonian rheology and clotting processes, *J. Stati Phys*, **121**(112), 209-221, 2005
- [52] S. Hou, X. Shan, Q. Zou, G. D. Doolen, W. E. Soll, Evaluation of two lattice Boltzmann models for multiphase flows, *J. Comp. Phys.* **138**, 695-713, 1997.
- [53] A. S. Joshi, Y. Sun, Multiphase lattice Boltzmann method for particle suspensions, *Phys. Rev. E.* **79**, 06703, 2009.
- [54] X. He, X. Shan and G. D. Doolen, Discrete Boltzmann equation model for nonideal gases, *Phys. Rev. E.*, **57**(R): 13-16, 1998.
- [55] X. He, and L-S. Luo, Theory of the Boltzmann method: From the Boltzmann equation to the lattice Boltzmann equation, *Phys. Rev. E.*, **56**, 6811-6817, 1997.
- [56] X. He, S. Chen and R. Zhang, A lattice Boltzmann scheme for incompressible multiphase flow and its application in simulation of Rayleigh-Taylor instability, *J. Comp.*



*Phys.*, **152**, 642-663, 1999.

- [57] A. J. Wagner, The origin of spurious velocities in lattice Boltzmann, *Int. J. Mod. Phys. B.* **17**, 193-196, 2003.
- [58] T. Lee and P. F. Fischer, Eliminating parasitic currents in the lattice Boltzmann equation method for nonideal gases, *Phys. Rev. E.*, **74**, 046709, 2006.
- [59] D. Chiappini, G. Bella, S. Succi, F. Toschi and S. Ubertini, Improved lattice Boltzmann without parasitic currents for Rayleigh-Taylor Instability, *Commun. Comput. Phys.*, **7**, 423-444, 2010.
- [60] Q. Lou, Z. Guo and C. Zheng, Some fundamental properties of lattice Boltzmann equation for two phase flows, *Comp. Mod. Eng. Sci.*, **76**, 175-188, 2011.
- [61] C. M. Pooley, K. Furtado, Eliminating spurious velocities in the free-energy lattice Boltzmann method, *Phys. Rev. E.*, **77**, 046702, 2008.
- [62] S. Leclair, M. Reggio and J.-Y. Trépanier, Isotropic color gradient for simulating very high-density ratios with a two-phase flow lattice Boltzmann model, *Comput. Fluids*, **48**, 98-112, 2011.
- [63] Z. Yu and L.-S. Fan, Multirelaxation-time interaction-potential-based lattice Boltzmann model for two-phase flow, *Phys. Rev. E.*, **82**, 046708, 2010.
- [64] P. Yuan, Thermal lattice Boltzmann two-phase flow model for fluid dynamics, *Ph. D dissertation, university of Pittsburgh*, 2005.
- [65] M. C. Sukop and D. Or, Lattice Boltzmann method for modeling liquid-vapor interface configurations in porous media, *Water Resour. Res.*, **40**, w01509, 2004.
- [66] N. S. Martys and H. Chen, Simulation of multicomponent fluids in complex three-dimensional geometries by the lattice Boltzmann method, *Phys. Rev. E.*, **53**, 743-750, 1996.
- [67] D. Iwahara, H. Shinto, M. Miyahara and K. Higashitani, Liquid drops on homogeneous and chemically heterogeneous surfaces: A two-dimensional lattice Boltzmann study,

*Langmuir*, **19**, 9086-9093, 2003.

- [68] T. Inamuro, N. Konishi and F. Ogino, A Galilean invariant model of the lattice Boltzmann method for multiphase fluid flows using free-energy approach, *Comput. Phys. Commun.*, **29**, 32-45, 2000.
- [69] T. Inamuro, R. Tomita and F. Ogino, Lattice Boltzmann simulations of drop deformation and breakup in shear flows, *Int. J. Mod. Phys. B.*, **17**, 21-26, 2003.
- [70] A. R. Davies, J. L. Summers and M. C. T. Wilson, On a dynamic wetting model for the finite-density multiphase lattice Boltzmann method, *Int. J. Comput. Fluid Dyn.*, **20**, 415-425, 2006.
- [71] A. Dupuis and J. M. Yeomans, Lattice Boltzmann modeling of droplets on chemically heterogeneous surface, *Future Generation Computer Systems*, **20**, 993-1001, 2004.
- [72] A. Dupuis and J. M. Yeomans, Mesoscopic modelling of droplets on topologically patterned substrates, *Computational Science*, **3039**, 556-563, 2004.
- [73] A. Dupuis and J. M. Yeomans, Modeling droplets on superhydrophobic surfaces: Equilibrium states and Transitions, *Langmuir*, **21**, 2624-2629, 2005.
- [74] A. Dupuis and J. M. Yeomans, Droplet dynamics on patterned substrates, *Pramana Journal of Physics*, **64**, 1019-1027, 2005.
- [75] H. Kusumaatmaja, A. Dupuis and J. M. Yeomans, Lattice Boltzmann simulations of drop dynamics, *Mathematics and Computers in Simulation*, **72**, 160-164, 2006.
- [76] Q. Chang and J. I. D. Alexander, Analysis of single droplet dynamics on striped surface domains using a lattice Boltzmann method, *Microfluid Nanofluid*, **2**, 309-326, 2006.
- [77] J. M. Yeomans and H. Kusumaatmaja, Modelling drop dynamics on patterned surfaces. *Bulletin of the Polish Academy of Sciences*, **55**, 203-209, 2007.
- [78] Y. Y. Yan, Physical and numerical modeling of biomimetic approaches of natural hydrophobic surfaces, *Chinese Science Bulletin*, **54**, 541-548, 2009.
- [79] Y. H. Kim, W. Choi and J. S. Lee, Water droplet properties on periodically structured

- superhydrophobic surfaces: a lattice Boltzmann approach to multiphase flows with high water/air density, *Microfluid Nanofluid*, **10**, 173-185, 2011.
- [80] A. Yamamoto and M. Suzuki, Simulation of the evaporation phenomenon of Metal by the lattice Boltzmann method, *J. Chem. Eng. Jpn.*, **35**, 944-950, 2002.
- [81] R. Zhang and H. Chen, Lattice Boltzmann method for simulations of liquid-vapor thermal flows, *Phys. Rev. E*, **67**, 066711, 2003.
- [82] A. S. Joshi and Y. Sun, Wetting dynamics and particle deposition for an evaporating colloidal drop: A lattice Boltzmann study, *Phys. Rev. E*, **82**, 041401, 2010.
- [83] A. S. Joshi and Y. Sun, Numerical simulation of colloidal drop deposition dynamics on patterned substrates for printable electronics fabrication, *J. Display Technol.*, **6**, 579-585, 2010.
- [84] A. Márkus and G. Házi, Simulation of evaporation by an extension of the pseudopotential lattice Boltzmann method: A quantitative analysis, *Phys. Rev. E*, **83**: 046705, 2011.
- [85] M. R. Kamali, J. J. J. Gillissen, S. Sundaresan and H. E. A. Van den Akker, Contact line motion without slip in lattice Boltzmann simulations, *Chem. Eng. Sci.*, **66**, 3452-3458, 2011.
- [86] A. Xu, G. Gonnella and A. Lamura, Phase separation of incompressible binary fluids with lattice Boltzmann method, *Physica. A.*, **331**, 10-22, 2004.
- [87] L.-S. Luo, The lattice-gas and lattice Boltzmann methods: Past, Present, and Future, *Proceedings of the International Conference on Applied Computational Fluid Dynamics*, Beijing, China, 329-364, 2000.
- [88] J. S. Rowlinson, B. Widom, Molecular theory of capillarity. Clarendon, Oxford, the United States of America, 1989.
- [89] J. Bao, P. Yuan and L. Schaefer, A mass conserving boundary condition for the lattice Boltzmann equation method, *J. Comp. Phys.*, **227**, 8472-8487, 2008.
- [90] O. Filippova, D. Hänel, Grid refinement for lattice-BGK models, *J. Comput. Phys.*, **147**, 219-228, 1998.

- [91] R. Mei, L-S. Luo and W. Shyy, An accurate curved boundary treatment in the lattice Boltzmann method, *J. Comput. Phys.*, **155**, 307-329, 1999.
- [92] R. Mei, W. Shyy, D. Yu and L-S. Luo, Lattice Boltzmann method for 3-D flows with curved boundary, *J. Comput. Phys.*, **161**, 680-699, 2000.
- [93] A. Frohn, and N. Roth, Dynamics of droplets, Springer, Berlin, Germany, 200-206, 2000.
- [94] Q. Liao, L. Chen, X. Qu and X. Jin, Brownian dynamics simulation of film formation of mixed polymer late in the water evaporation stage, *J. Colloid Interface Sci.*, **227**, 84-94, 2000.
- [95] N. Saito, Y. Kagari and M. Okubo, Revisiting the morphology development of solvent-swollen composite polymer particles at thermodynamic equilibrium, *Langmuir*, **23**, 5914-5919, 2007.
- [96] M. E. R. Shanahan and K. Sefiane, Kinetics of triple line motion during evaporation, Contact Angle, Wettability and Adhesion, Koninklijke Brill, Leiden, the Netherlands, 19-31, 2009.

## **Publications**

### ❖ Refereed journal

R.-J. Li and Y. Morozumi, “The effect of the computational parameters on the reduction of spurious velocities in lattice Boltzmann simulation of two-phase flows” Computers & Fluids, submitted

R.-J. Li and Y. Morozumi, “A Lattice Boltzmann Simulation for Contact Line Motion and Internal Fluid Flows in an Evaporating Droplet on Homogenous Substrates”, Journal of Chemical Engineering of Japan, Vol. 45, No. 3, pp. 155-165, 2012

Y. Morozumi, R.-J. Li, “Lattice Boltzmann Simulation of Droplet Drying Behavior on Substrates with Different Wettability”, Kochi university of Technology Research Bulletin, Vol.7, pp. 71-79, 2010

### ❖ International conference

R.-J. Li and Y. Morozumi, Numerical Simulation of Evaporation Process of a Droplet on Substrates with Different Wettability, Proceedings of the 22nd International Symposium on Transport Phenomena, Delft, Netherland, 2011

R.-J. Li and Y. Morozumi, “A Lattice Boltzmann Simulation of an Evaporating droplet on Wetting Substrate”, 2nd International Conference on Chemistry and Chemical Engineering, Chengdu, China, 2011

R.-J. Li and Y. Morozumi, “A Lattice Boltzmann Simulation of Drying Liquid Film on Patterned Substrates with Different Wettability”, The 17th International Drying Symposium, Magdeburg, Germany, 2010

### ❖ National conference

R.-J. Li and Y. Morozumi “A Lattice Boltzmann Simulation of Contact Line Motion of Evaporating Droplets on Patterned Surface”, The 42th annual meeting of the society of

Chemical Engineers Japan, Kyoto, 2010

Y. Morozumi, R.-J. Li, “Lattice Boltzmann Simulation of Droplet Evaporation on Substrates with Different Wettability, 47th National Heat Transfer Symposium of Japan, Sapporo, 2010

## Acknowledgments

During this work, I want to give my thanks to these people who helped me. At first, I will thanks to my advisor Dr. Morozumi, who provided me with his suggestions and advice to support my research works. He often taught me what is researched thinking and how to do research which is same with how to connect with other person. He often told me that I should not talk 'I don't know' when I do my research.

I'd like to thank the Prof. Chono, Prof. Tsusui, Prof. Tsuji and Prof. Momota, they gave me so many precious suggestions and much support for my research. I would also like to thank my master advisor Dr. Sun Minhua, he give me so many support and encouragement when I have problem about my life and research in Japan.

My thanks are extended to the member of who helped me for living in Japan, my Chinese and Japanese friends and IRC members. I feel lucky to have a lot of good friends in Japan. The member follows as: Zhang Jianguo, Sun Liang, Tan Renpeng, Li Zeming, Wang Yina, Li Chunguang, Hou Liyuan, Ishimoto and Kitaoka, *et al.*. My time spent with these friends and went fast.

I reserve my sincere thanks for my family member and boyfriend, they give me love and support in my life.